Title

Flows of settling marine aggregates and complex fluid rheology

Author

Yoo, Eunji

Publication Date

2023

UNIVERSITY OF CALIFORNIA, MERCED

Flows of settling marine aggregates and complex fluid rheology

A dissertation submitted in partial satisfaction of the
requirements for the degree Doctor of Philosophy

in

Applied Mathematics

by

Eunji Yoo

Committee in charge:

François Blanchette, Co-Chair
Shilpa Khatri, Co-Chair

Changho Kim
Camille Carvalho (Institut National des Sciences Appliquées de Lyon)
Ishan Srivastava (Lawrence Berkeley National Laboratory)

2023

The dissertation of Eunji Yoo is approved, and it is acceptable in quality and form for publication on microfilm and electronically:

(Changho Kim)

(Camille Carvalho (Institut National des Sciences Appliquées de Lyon))

(Ishan Srivastava (Lawrence Berkeley National Laboratory))

(Shilpa Khatri, Co-Chair)

(François Blanchette, Co-Chair)

University of California, Merced

2023

TABLE OF CONTENTS

LIST OF FIGURES

LIST OF TABLES

DEDICATION

To my family, Dr. Dallerit
To my friends, Diversity 101 & Susan
To my heavenly Father
I can do all things through Him who strengthens me.
- Philippians 4:13

ACKNOWLEDGEMENTS

I thank my research advisors, Dr. François Blanchette and Dr. Shilpa Khatri, for their constant support and patience.

ABSTRACT OF THE DISSERTATION

Flows of settling marine aggregates and complex fluid rheology

by Eunji Yoo
Doctor of Philosophy in Applied Mathematics

University of California Merced, 2023

Committee Co-Chairs: François Blanchette and Shilpa Khatri

Settling marine aggregates are essential in transporting dissolved carbon dioxide from the surface ocean to the deep sea. While sinking, they may accumulate in thin layers where density stratification is present, becoming nutrient hotspots for bacteria and animal activity. We simulate settling marine aggregates both in an ambient homogeneous and a density-stratified fluid to study their dynamics. We model a marine aggregate as a fractal collection of cubes. In a homogeneous fluid, the flow is computed in the Stokes regime using a boundary integral method. We focus on analyzing the forces acting on the aggregate in the presence of various background flows. We have identified an effective hydrodynamic radius that captures the settling dynamics accurately. We couple the velocity with the advection-diffusion equation to track the heat density or salt concentration in time. We use this method to quantify how the presence of stratification affects the settling speed and time of the aggregates.

We also present the study of complex fluids with higher-order rheology. We introduce rate-dependent flows having non-Newtonian behaviors. We pay attention to a flow of granular material, which is the second most commonly used material in industry after water. We model a second-order stress tensor in strain rate for granular material within an Adaptive Mesh Refinement (AMR) framework, AMReX-incflo, to solve for incompressible flows. We also formulate a regularization of the yield stress terms to account for viscosity divergence at low strain rates. To incorporate a higher-order strain rate tensor with the incompressible solver numerically, we added a two-stage Runge-Kutta scheme in the AMReX-incflo code and the default solver, the explicit Euler method.

Chapter 1

Introduction

Marine aggregates are randomly formed particles composed of organic and inorganic matter, such as phytoplankton, detritus, sediment, and fecal pellets (Jackson, 1989). Since these components stick together arbitrarily, a marine aggregate is often shown as a fractal structure. These marine aggregates take in carbon dioxide (CO_2) during photosynthesis near the surface ocean and carry the dissolved carbon to the deep ocean. This process removes CO_2 from the atmospheric carbon cycle (Honjo et al., 2014) and plays a role in regulating atmospheric CO_2 and climate changes, which is one of the most significant environmental problems we face today.

It has been observed that larger sinking aggregates tend to accumulate in thin layers where the ambient fluid is density stratified (Alldredge et al., 2002). The highly concentrated thin layers become biological hotspots for bacterial activity and animal feeding. It is ecologically important to understand the marine aggregates' dynamics as they delay in settling.

We consider the flows around aggregates in the low Reynolds number regime, which is applicable for approximately the smallest 30% of marine aggregates (Alldredge & Gotschalk, 1988). Flow in this regime is governed by the Stokes equations, which allows solutions to be found via boundary integral methods (Pozrikidis, 1992). Such methods have been implemented in several contexts, typically via a combination of analytical integration near the singularities that arise and quadrature methods away from the singularities. See (Pozrikidis, 1992) for a review. Boundary integral methods are particularly well suited to computations of flow around complex solids (Zinchenko & Davis, 2006) as velocity and forces may be expressed in terms of an integral over the boundary of the object. They have also recently been combined with other methods, for example, to capture interactions between fluids and elastic solids (Bao et al., 2017) and stochastic fluctuations in suspensions (Bao et al., 2018). Here, we form aggregates using cubic particles, which results in a simple boundary over which the resulting integrals can be computed analytically, as described in Chapter 2. This has the advantage of avoiding numerical singularities on the boundary, which otherwise require regularization (Cortez, 2001) or specialized numerical methods such as high-order product Nyström methods (Atkinson, 1997; Delves & Mohamed, 1985), adaptive sub-domain integration (Chan, Beris, & Advani, 1992), or nearest-neighbor discretization of the regularized Stokeslet boundary integral equation (Smith, 2018). We introduce a novel implementation of boundary integral methods which is both simple and well-behaved numerically. Details of this new methodology, along with its validation, are presented in Section 2.4. We compare two approaches, using a single-layer and double-layer integral representation of the velocity (Pozrikidis, 1992; Power & Miranda, 1987; Ingber & Mammoli, 1999), and determine which is the most suitable for fluid flow simulations around marine aggregates with this new method.

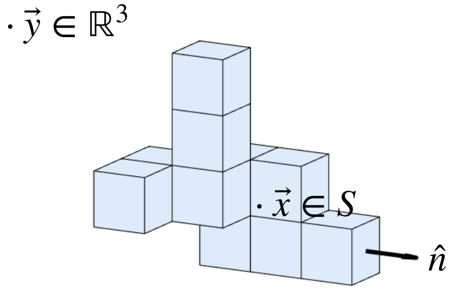

Figure 1.1: Example aggregate model with ten cubes. We denote S as the aggregate boundary surface and $\hat{n}$ as its normal. The vectors $\vec{x}$ and $\vec{y}$ are points on and outside of S.

Our research is centered on computing the velocity field around settling marine aggregates and the forces acting on them. We do so using boundary integral equation (BIE) formulations. We construct marine aggregates using cubes to capture their fractal shape, as shown in Figure 1.1.

1.1 Fluid momentum equations

To describe the incompressible fluid motion that takes place around marine aggregates, we consider the Navier-Stokes equations,

$$\nabla \cdot \vec{u} = 0 \tag{1.1}$$

$$\rho \left(\frac{\partial \vec{u}}{\partial t} + \vec{u} \cdot \nabla \vec{u} \right) = \nabla \cdot \bar{\bar{\sigma}} + \rho \vec{g}, \tag{1.2}$$

where ρ is fluid density (constant) and $\vec{u}$, $\vec{g}$ are fluid velocity and gravity vectors, respectively. The first equation (1.1) shows the conservation of mass, and equation (1.2) describes the momentum conservation. We also introduce the stress tensor, $\bar{\bar{\sigma}}$ as sum of the fluid pressure P and deviatoric stress tensor $\boldsymbol{\tau}$,

$$\bar{\bar{\sigma}} = -P\bar{\bar{I}} + \boldsymbol{\tau} = -P\bar{\bar{I}} + 2\tilde{\mu}\boldsymbol{D}, \tag{1.3}$$

where $\tilde{\mu}$ is constant fluid viscosity and $\boldsymbol{D}$ is the symmetric strain rate tensor, that is,

$$\boldsymbol{D} = \frac{1}{2} \left(\nabla \vec{u} + (\nabla \vec{u})^T \right). \tag{1.4}$$

Since seawater is a Newtonian fluid, following Newton's law of viscosity, the strain rate (1.4) becomes $\nabla \vec{u}$. This implies that we can rewrite the momentum equation (1.2) as

$$\rho \left(\frac{\partial \vec{u}}{\partial t} + \vec{u} \cdot \nabla \vec{u} \right) = -\nabla P + \tilde{\mu} \nabla^2 \vec{u} + \rho \vec{g} \tag{1.5}$$

For typical seawater, it is reasonable to say $\rho \approx 1025\text{kg}/\text{m}^3$ and $\tilde{\mu} = 1.2 \times 10^{-3}\text{kg}/\text{ms}$. Also, the gravity vector is $\vec{g} = -g\hat{k} \approx -9.8\text{m}/s^2 \times (0, 0, 1)$ where $\hat{k}$ points in the vertical direction (upward).

The momentum equation (1.2) can be linearized for flows where inertial effects are small. To estimate the size of the main forces at play, we consider a radius of marine aggregate, $R_a \approx 5 \times 10^{-5}(\text{m})$ and the reference Stokes settling speed of an aggregate,

$$U_s = \frac{gR_a^2}{\tilde{\mu}}(\rho_a - \rho) \approx 3.8 \times 10^{-4}(\text{m}/\text{s}), \tag{1.6}$$

where $\rho_a \approx 1400\text{kg}/\text{m}^3$ is the aggregate mass density. When we non-dimensionalize the momentum equation using the length scale, R_a, and velocity, U_s, we obtain the following equation:

$$\left(\frac{\rho U_s R_a}{\tilde{\mu}} \right) \left(\frac{\partial \vec{u}'}{\partial t'} + \vec{u}' \cdot \nabla' \vec{u}' \right) = \nabla'^2 \vec{u}' - \nabla' P' + \vec{g}', \tag{1.7}$$

where we find and compute the Reynolds number (Re),

$$\mathrm{Re} = \frac{\rho U_s R_a}{\tilde{\mu}} \approx 10^{-2} \ll 1. \tag{1.8}$$

Note that we use the prime symbol to represent a dimensionless value. Since we have a fairly small Reynolds number, we may neglect the inertial effects, limiting the left-hand side of equation (1.7) to zero,

$$\nabla'^2 \vec{u}' - \nabla' P' + \vec{g}' = 0. \tag{1.9}$$

In the settling marine aggregate project part of this thesis, we, therefore, consider the following Stokes equations, written with dimensions, to describe the fluid flow around the settling aggregates,

$$\begin{gathered} \nabla \cdot \vec{u} = 0 \\ \tilde{\mu} \nabla^2 \vec{u} - \nabla P \ + \rho \vec{g} = 0. \end{gathered} \tag{1.10}$$

The solutions of the system of equations are the fluid velocity, $\vec{u}$, and pressure, P. In general, pressure does not induce motion. We see the pressure at rest, denoted as P_s, contains the pressure of gravity, $P_s(\vec{y}) = \rho \vec{g} \cdot \vec{y}$, where $\vec{y} \in \mathbb{R}^3$ is a point in the fluid. Using this static pressure term, we introduce the dynamic pressure P_d, defined as

$$P_d(\vec{y}) = P(\vec{y}) - P_s(\vec{y}) = P(\vec{y}) - \rho \vec{g} \cdot \vec{y}. \tag{1.11}$$

By substituting the expression (1.11), we obtain

$$\begin{gathered} \nabla \cdot \vec{u} = 0 \\ \tilde{\mu} \nabla^2 \vec{u} - \nabla P_d = 0. \end{gathered} \tag{1.12}$$

While an aggregate model settles, we focus on the velocity field and hydrodynamic forces around the marine aggregate model.

1.2 Boundary integral equation (BIE) formulations

For our simulations, we consider a large fluid domain compared to the size of an aggregate, having zero fluid velocity at infinity. We also treat our aggregate surface as a solid. Although marine aggregates are porous, the solid boundary condition is reasonable to apply due to their low permeability. This condition prevents flow through the aggregate, acting like a solid particle. For this reason, any flow inside of the aggregate is neglected in the remainder of this thesis.

For a general surface S, the velocity $\vec{u}$ at a point $\vec{y} \in \mathbb{R}^3$ exterior to the surface may generally be expressed using the representation formula (Pozrikidis, 1992) when solving for the flow using the Stokes equations,

$$\vec{u}(\vec{y}) = -\frac{1}{8\pi\tilde{\mu}} \int_S \vec{f}(\vec{x}) \cdot \bar{\bar{G}}(\vec{x},\vec{y}) \, \mathrm{d}S(\vec{x}) + \frac{1}{8\pi} \int_S \vec{u}(\vec{x}) \cdot \bar{\bar{K}}(\vec{x},\vec{y}) \cdot \hat{n}(\vec{x}) \, \mathrm{d}S(\vec{x}), \tag{1.13}$$

where the integral is taken over points $\vec{x}$ on the surface S. The kernel $\bar{\bar{G}}(\vec{x},\vec{y})$ is the Green's function of the Stokes equations at any point $\vec{y}$, that is the *Stokeslet*, in the domain for a point-source located at $\vec{x}$,

$$\bar{\bar{G}}(\vec{x},\vec{y}) = \frac{\bar{\bar{I}}}{||\vec{x}-\vec{y}||} + \frac{(\vec{x}-\vec{y})(\vec{x}-\vec{y})}{||\vec{x}-\vec{y}||^3}. \tag{1.14}$$

The kernel $\bar{\bar{K}}(\vec{x},\vec{y})$ is the stress tensor associated with this fundamental solution, named the *Stresslet*,

$$\bar{\bar{K}}(\vec{x},\vec{y}) = -6\frac{(\vec{x}-\vec{y})(\vec{x}-\vec{y})(\vec{x}-\vec{y})}{||\vec{x}-\vec{y}||^5}, \tag{1.15}$$

where $\|\cdot\|$ is the vector 2-norm. The first integral distribution on the right-hand side of equation (1.13) is called the *single-layer potential*, and the second one is called the *double-layer potential*. To compute the velocity at a point on the surface S, i.e., $\vec{x}_s \in S$, we use

$$\vec{u}(\vec{x}_s) = -\frac{1}{4\pi\tilde{\mu}} \int_S \vec{f}(\vec{x}) \cdot \bar{\bar{G}}(\vec{x},\vec{x}_s) \, \mathrm{d}S(\vec{x}) + \frac{1}{4\pi} \int_S \vec{u}(\vec{x}) \cdot \bar{\bar{K}}(\vec{x},\vec{x}_s) \cdot \hat{n}(\vec{x}) \, \mathrm{d}S(\vec{x}). \tag{1.16}$$

In general, $\vec{f}(\vec{x})$ is the unknown stress vector, or traction, on the surface, and $\vec{u}(\vec{x})$ is the, typically unknown, velocity on the surface S. When S is the boundary of a solid object, in our case, an aggregate, the general representation formula may be simplified in two different ways, depending on the fluid domain characteristics and the object's surface. We will introduce those two formulae in Chapter 2.

1.3 Complex fluids

In the last part of this thesis, we will turn our attention to non-Newtonian fluids. This topic is added to my thesis as an extension of a summer internship at the Lawrence Berkeley National Lab in 2022 under the guidance of Dr. Ishan Srivastava.

A broad class of complex fluids encompasses various materials of natural, industrial, and medical importance, such as granular materials, suspensions of micro-scale materials, and biological molecules. Complex fluids show many interesting behaviors quite different than Newtonian fluids. The major difference is that the viscosity (denoted $\tilde{\mu}$ in the Newtonian fluid case) is not constant anymore; rather, it is attributed to the shear rate $\dot{\gamma} = |\boldsymbol{D}|$ (Kundu, Cohen, & Dowling, 2016). Due to this varying viscosity, the constitutive behavior of non-Newtonian fluids is highly complex. To understand their behaviors, we shall focus on the viscous stress tensor, $\boldsymbol{\tau}$, introduced in equation (1.3). In particular, we explore four features of viscosity in complex fluids: 1) (shear) rate-dependent flow, 2) yield stress, 3) a second-order strain rate rheology, and 4) granular material flow. Note that *rheology* is the study of material deformation and flows as responses to applied stress, including those that exhibit co-existing two states.

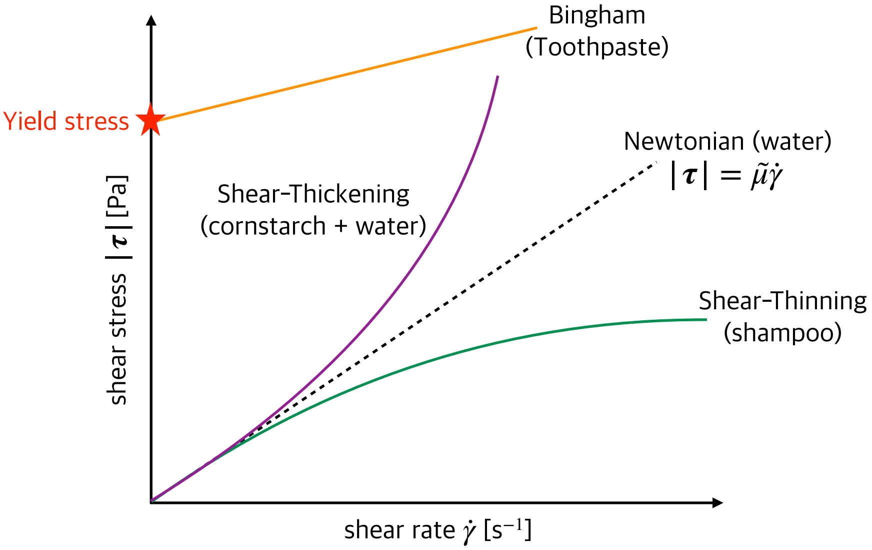

Figure 1.2: Classification of fluid types based on descriptions in (Irgens, 2014). Solid lines show different types of non-Newtonian behavior with examples in the parenthesis. The red star describes yield stress. The dashed line represents Newton's law of viscosity.

Figure 1.2 demonstrates how the shear stress, $|\boldsymbol{\tau}|$, varies on the shear rate $\dot{\gamma}$, with an example. Two types of rate-dependent flow, shear-thinning, and thickening, are plotted with the green and purple lines, respectively. The viscosity of a shear-thinning fluid, such as shampoo or mayonnaise, decreases as the shear rate increases (Singh &

Heldman, 2013). On the other hand, shear-thickening fluid viscosity gets higher under shear strain (Barnes, Hutton, & Walters, 1989). Meanwhile, the orange straight line represents the Bingham plastic fluid. One defining characteristic of many complex fluids is the presence of yield stress, which is shown as the red star on the vertical axis. Yield stress is an instantaneous stress value to make a material flow. For an insufficiently stressed state, the material behaves like an elastic solid, allowing deformation plastically; once the yield stress is exceeded, it flows like a fluid (Irgens, 2014). Examples of yield stress fluids include toothpaste, cement, mud, and blood. We will discuss more of the relationship between viscosity and shear rate in Chapters 4.2 and 4.3.

While the viscous stress tensor of the rate-dependent fluids has a linear relationship with the strain rate, $\boldsymbol{D}$, other flow effects can be captured by a higher-order strain rate. In this thesis, we explore up to the second-order case and call them secondary flows. In the recent paper by (Tanner, 2018), Tanner discussed several examples of non-colloidal suspensions and highlighted the importance of examining these secondary flows. For instance, a curvature in free-surface flows (Couturier et al., 2011), anomalous stress profile in cylindrical Couette flows (Krishnaraj & Nott, 2016), or negative rod climbing effect (Weissenberg effect) (Boyer, Pouliquen, & Guazzelli, 2011) are found for a non-linear strain rate effect. We thus want to implement computational tools to study the second-order strain rate effect.

Lastly, we present further work for granular materials. They are highly ubiquitous and the second most common material on earth after water (Richard et al., 2005). For example, we can find grains in the food industry, pharmaceutical powder to make medicine tablets, and geological materials, such as sand or soil. One fascinating property is that they can behave like a liquid, solid, and gas, coexisting simultaneously. For instance, sand in a desert can stay still like a solid without any external forces; it can also flow or slide like a fluid when there is wind. There are still many open questions we should study to understand the behaviors of granular materials due to the complicated dynamics.

Our ultimate goal for this project is to have a constitutive rheology code that can capture complex continuum dynamics. We use the exascale computing package AMReX-Codes, which is a block-Structured Adaptive Mesh Refinement (AMR) Software Framework and Applications. We implement the granular rheology in an individual module of AMReX called *incflo*. This code allows us to model the incompressible

Navier-Stokes equations with various types of rheology in complex geometries without subcycling in time. We will describe the details of the numerical methods in Chapter 4.4.

This dissertation is ordered as follows: in Chapter 2, we introduces the simulations of settling marine aggregates in a homogeneous fluid. As an extended study, we explore a density-stratified fluid to understand more realistic marine aggregate behaviors in Chapter 3. Lastly, Chapter 4 addresses complex fluid rheology and granular materials using the AMReX-Codes.

Chapter 2

Settling marine aggregates in a homogeneous fluid

The content of this chapter has been published in Yoo, E., Khatri, S., & Blanchette, F. (2020). Hydrodynamic forces on randomly formed marine aggregates [Publisher: American Physical Society]. *Physical Review Fluids*, *5*(4), 044305. https://doi.org/10.1103/PhysRevFluids.5.044305

In this chapter, we compute the flow around randomly-formed aggregates and characterize the resulting hydrodynamic forces in a constant-density fluid. Since the 1980s, there have been numerous models of aggregation, including marine aggregation, based on the random motion of small particulates (Rosenstock & Marquardt, 1980; Witten & Sander, 1981; Witten & Cates, 1986; Kolb, 1987). To form aggregates, we use two established models: individually-added aggregation and cluster-cluster aggregation, which are described in detail in (Yoo, Khatri, & Blanchette, 2020). We study the hydrodynamics of flow around a broad sample of the resulting aggregates. In situ, measurements of oceanic aggregates have shown an approximately linear relationship between the drag and the aggregate diameter (Alldredge & Gotschalk, 1988). Experimental studies of settling aggregates first focused on inorganic clusters (Wiltzius, 1987) and later considered precisely constructed aggregates (Takayasu & Galembeck, 1998) and statistical descriptions of broader ensembles (C. P. Johnson, Li, & Logan, 1996). It was generally found that a linear relationship exists between the drag and the square root of the projected area, which allows for the identification of a corresponding settling hydrodynamic radius (C. P. Johnson, Li, & Logan, 1996; Tang, Greenwood, & Raper, 2002). However, these experimental studies did not allow for a systematic variation of certain parameters and found a range of results depending on the measure used and the exact composition of the aggregates. Computational studies, in theory, do not have this limitation. Early numerical results were based on rather coarse approximations of aggregates, using point particle approximations (Chen, Deutch, & Meakin, 1984). The accelerated Stokesian dynamics (ASD) approach, which model aggregates as a collection of spheres and accounts for lubrication forces between them, was later developed (Brady & Bossis, 1988) and used to estimate a hydrodynamic radius for progressively larger aggregates (Rogak & Flagan, 1990; Bossis, Meunier, & Brady, 1991). In addition to the drag on settling aggregates, the torque on rotating aggregates was computed using ASD (Binder, Hartig, & Peukert, 2009). More recently, results were obtained using Lattice-Boltzmann simulations that also considered inertial effects (Zhang & Zhang, 2015). The distribution of internal stresses in rigid aggregates moving in a constant flow, which may result in an aggregate break-up, was also recently studied using the method of reflections (Gastaldi & Vanni, 2011) and again using ASD (Vanni, 2015). We develop here computational simulations that, in the regime considered, are more flexible and efficient, allowing us to study a greater number of aggregates, resulting in more statistically reliable results.

While ocean water is density stratified due to temperature or salinity, we begin with the simplifying assumptions of uniform fluid density to understand settling aggregate dynamics. As marine aggregates have fractal structures, it is important to find an appropriate length scale to be able to predict their settling speed more accurately. We thus consider a homogeneous fluid in this chapter to choose an effective hydrodynamic radius.

2.1 Aggregation Model

To model marine aggregates, we make use of existing models of aggregation where the constituting particles undergo a random walk (Rosenstock & Marquardt, 1980; Witten & Sander, 1981; Witten & Cates, 1986; Kolb, 1987). In these models, particles are typically subject to uniform Brownian motion and attach to one another when sufficiently close. The resulting aggregates often have a fractal structure characterized by a fractal dimension, d. The fractal dimension describes the nature of these complicated objects

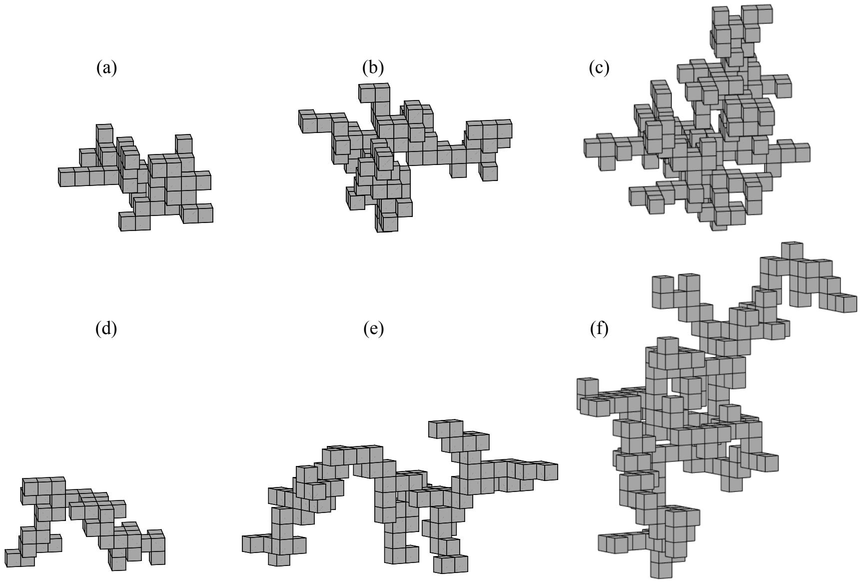

Figure 2.1: We show typical aggregates as formed by two different methods. Top row: individually-added-aggregates (IAA) containing (a) 50, (b) 100, and (c) 200 cubes. Bottom row: cluster-to-cluster aggregates (CCA) containing (d) 50, (e) 100, and (f) 200 cubes.

and may be defined from the relation $N \sim (R_s/l)^d$, where N is the number of particles of length scale l that are part of the aggregate within a sphere of radius R_s (Witten & Cates, 1986). In general, fractal dimensions of aggregate models have been found to range from 1.3 to 3 depending on the exact formation mechanism (Witten & Sander, 1981; Kolb, 1987; Gmachowski, 2002). Direct observations of marine aggregates have found fractal dimensions ranging approximately from 1.3 to 2.5 (Alldredge & Gotschalk, 1988; Jackson & Burd, 1998).

We consider aggregates made of collated cubic particles, as shown in Figure 2.1. Once formed, we assume that aggregates do not deform, sinter, or break apart (Eggersdorfer et al., 2011). This is a flexible model that has the advantage of having a simple external boundary, which will be exploited when we solve for the flow around the aggregate. We generate diffusion-limited aggregates using two different techniques: (1) individually-added aggregation (IAA) and (2) cluster-to-cluster aggregation (CCA) (Witten & Cates, 1986; Kolb, 1987). In both methods, each cube has a non-dimensional length, 2, is aligned with the Cartesian axes, and is centered at a point on a three-dimensional Cartesian lattice restricted to a triply periodic box of period $2P$. The cube centers thus only take values of the form $\{(2m, 2n, 2p) \,|m, n, p \in \mathbb{Z}, -P < m, n, p \leq P\}$.

Typically, the IAA method gives a more compact form of aggregates, with dimension ≈ 2.56, than the CCA case, which has dimension ≈ 1.79 (Witten & Sander, 1981; Kaye, 2008). More details regarding the analysis of the aggregation formation can be found (Yoo, Khatri, & Blanchette, 2020).

To characterize the size of each aggregate, we define the dimensionless gyration radius, R'_g, also known as the root-mean-square radius, as

$$R'_g = \sqrt{\frac{1}{NC}\sum_{i=1}^{NC} \|\vec{x}_i - \vec{x}_{cm}\|^2}, \tag{2.1}$$

and the maximum radius of the aggregate, R'_m, as the maximum distance between the center of each of its constituting cubes, $\vec{x}_i$, and the center of mass, $\vec{x}_{cm}$, to which we add one to account for the size of an individual cube,

$$R'_m = 1 + \max_{i=1,\cdots,NC} \|\vec{x}_i - \vec{x}_{cm}\|, \tag{2.2}$$

where NC is the number of cubes in the aggregate. We obtain the center of mass of the aggregate, $\vec{x}_{cm}$, by taking the mean values of each element of $\vec{x}_i$ for $i = 1, \cdots, NC$. Note that most experimental studies use the projected area method to describe the size of an aggregate. However, since this project is done computationally, which has more freedom than physical experiments, we choose to use those formulations (2.1) and (2.2) without reduction of dimension. We will later show the results of different forces acting on the aggregates and examine which size measurement captures better physical properties.

2.2 Derivation of single- and double-layer potentials

We introduced equation (1.16) as a solution to the Stokes equations in Chapter 1. As we have a solid boundary surface of a marine aggregate model, we are able to use a simplified version of the fundamental solution. We are interested in solving for the flow at points $\vec{y}$ in the fluid domain, which extends to infinity, and external to the surface, S, of an aggregate, as shown in Figure 1.1. We take advantage of the linearity of the Stokes equations and express the velocity as a boundary integral over the surface of the aggregate (Pozrikidis, 1992; Stakgold, 2000). The resulting Fredholm integral formulas have the advantage of involving computations in two dimensions only, despite the three-dimensionality of the system. For solid objects, one may obtain two different

Fredholm integral formulas. We derive both formulations in the remainder of this section, following the guidance of (Pozrikidis, 1992).

2.2.1 Single-layer potential (SLP)

We first derive the velocity with the single-layer potential alone. The solid boundary condition allows us to express the aggregate's velocity as

$$\vec{u}_s\left(\vec{x}\right) = \vec{U}_a + \vec{\Omega} \times \left(\vec{x} - \vec{x}_{cm}\right), \tag{2.3}$$

where $\vec{U}_a$ and $\vec{\Omega}$ are constant translational and angular velocities, respectively. Without loss of generality, we conveniently choose a zero center of mass, $\vec{x}_{cm} = \vec{0}$, for this derivation. Substituting the solid object velocity, equation (2.3), into the double-layer potential in equation (1.13) gives

$$\begin{aligned} &\int_S \left(\vec{U}_a + \vec{\Omega} \times \vec{x}\right) \cdot \bar{\bar{K}}(\vec{x}, \vec{y}) \cdot \hat{n}(\vec{x})\, \mathrm{d}S(\vec{x}) \\ &= \int_S \vec{U}_a \cdot \bar{\bar{K}}(\vec{x}, \vec{y}) \cdot \hat{n}(\vec{x})\, \mathrm{d}S(\vec{x}) + \int_S \left(\vec{\Omega} \times \vec{x}\right) \cdot \bar{\bar{K}}(\vec{x}, \vec{y}) \cdot \hat{n}(\vec{x})\, \mathrm{d}S(\vec{x}) \end{aligned} \tag{2.4}$$

The first integral on the right-hand side of equation (2.4) can be re-written as

$$\vec{U}_a \cdot \int_S \bar{\bar{K}}(\vec{x}, \vec{y}) \cdot \hat{n}(\vec{x})\, \mathrm{d}S(\vec{x}), \tag{2.5}$$

since the translational velocity $\vec{U}_a$ is constant. For the flow around (outside) and on the solid object, Pozrikidis provides a useful identity (Pozrikidis, 1992),

$$\int_S \bar{\bar{K}}(\vec{x}, \vec{y}) \cdot \hat{n}(\vec{x})\, \mathrm{d}S(\vec{x}) = \begin{cases} \bar{\bar{0}} & \text{if } \vec{y} \in \mathbb{R}^3 \setminus (S \cup \text{inside of aggregate}) \\ -4\pi \bar{\bar{I}} & \text{if } \vec{y} \in S \end{cases}. \tag{2.6}$$

Then, including the velocity $\vec{U}_a$, we get

$$\vec{U}_a \cdot \int_S \bar{\bar{K}}(\vec{x}, \vec{y}) \cdot \hat{n}(\vec{x})\, \mathrm{d}S(\vec{x}) = \begin{cases} \vec{0} & \text{if } \vec{y} \in \mathbb{R}^3 \setminus (S \cup \text{inside of aggregate}) \\ -4\pi \vec{U}_a & \text{if } \vec{y} \in S \end{cases}. \tag{2.7}$$

The second integral in equation (2.4) can be evaluated with the following identity, from (Pozrikidis, 1992), using Einstein (summation) notation,

$$\begin{aligned} &\varepsilon_{i\ell m} \int_S x_\ell\, K_{mjk}(\vec{x}, \vec{y})\, n_k(\vec{x})\, \mathrm{d}S(\vec{x}) \\ &= \begin{cases} \vec{0} & \text{if } \vec{y} \in \mathbb{R}^3 \setminus (S \cup \text{inside of aggregate}) \\ -4\pi\, \varepsilon_{i\ell j}\, x_\ell & \text{if } \vec{y} \in S \end{cases}, \end{aligned} \tag{2.8}$$

where $\varepsilon_{i\ell m}$ is the Levi-Civita permutation symbol. Multiplying both sides by the angular velocity, Ω, in equation (2.8), we get

$$\int_S \left(\vec{\Omega} \times \vec{x}\right) \cdot \bar{\bar{K}}(\vec{x}, \vec{y}) \cdot \hat{n}(\vec{x})\, \mathrm{d}S(\vec{x}) = \int_S (\varepsilon_{i\ell m}\, \Omega_i x_\ell)\; K_{mjk}(\vec{x}, \vec{y})\, n_k(\vec{x})\, \mathrm{d}S(\vec{x})$$

$$= \begin{cases} \vec{0} \\ -4\pi\, \varepsilon_{i\ell j}\, \Omega_i\, x^0_\ell \end{cases} = \begin{cases} \vec{0} & \text{if } \vec{y} \in \mathbb{R}^3 \setminus (S \cup \text{inside of aggregate}) \\ -4\pi\, (\Omega \times \vec{y}) & \text{if } \vec{y} \in S. \end{cases} \tag{2.9}$$

We now combine the two equations, (2.7) and (2.9),

$$\int_S \vec{u}(\vec{x}) \cdot \bar{\bar{K}}(\vec{x}, \vec{y}) \cdot \hat{n}(\vec{x})\, \mathrm{d}S(\vec{x}) = \begin{cases} \vec{0} & \text{if } \vec{y} \in \mathbb{R}^3 \setminus (S \cup \text{inside of aggregate}) \\ -4\pi \vec{u}(\vec{y}) & \text{if } \vec{y} \in S \end{cases}. \tag{2.10}$$

When the point $\vec{y}$ is strictly outside of the aggregate surface, S,

$$\vec{u}(\vec{y}) = -\frac{1}{8\pi\tilde{\mu}} \int_S \vec{f}(\vec{x}) \cdot \bar{\bar{G}}(\vec{x}, \vec{y})\, \mathrm{d}S(\vec{x}), \tag{2.11}$$

only the single-layer potential term. For evaluation points on the surface S, $\vec{y} = \vec{x}_s \in S$, since the double-layer potential is $-4\pi\vec{u}(\vec{x}_s)$, when we substitue into equation (1.16), we obtain exactly the same equation (2.11). This implies that the single-layer potential formula is continuous across the boundary surface S. To analyze the force and torque, we use the stress $\vec{f}$ from equation (2.11) to compute

$$\vec{F}_o = \int_s \vec{f}(\vec{x})\, \mathrm{d}S(\vec{x}) \qquad \text{and} \qquad \vec{Q}_o = \int_s (\vec{x} - \vec{x}_{cm}) \times \vec{f}(\vec{x})\, \mathrm{d}S(\vec{x}). \tag{2.12}$$

where $\vec{F}_o$ and $\vec{Q}_o$ represent the total force and torque, respectively, acting on the aggregate surface S.

2.2.2 Double-layer potential (DLP)

The second approach we can take is removing the single-layer potential. To derive the double-layer potential formulation, we consider a complimentary flow $\vec{u}_c$ for the points *inside* of the aggregate surface boundary S, having the same force on the boundary as $\vec{u}$. More specifically, the velocity $\vec{u}$ has the representation form, equation (1.13) and the complimentary flow $\vec{u}_c$ has the same stress, $\vec{f}$, on the boundary as $\vec{u}$. Before we proceed, we shall justify the existence of the complimentary flow. The new flow $\vec{u}_c$ can be found when the velocity $\vec{u}$ on the boundary satisfies

$$\int_S \vec{u}(\vec{x}) \cdot \hat{n} \, \mathrm{d}S(\vec{x}) = 0. \tag{2.13}$$

This condition is taken from (Pozrikidis, 1992). This can be fulfilled with our problem due to the continuity equation, $\nabla \cdot \vec{u} = 0$, and the divergence theorem. By the conservation of mass, we can say

$$\int_V \nabla \cdot \vec{u}(\vec{x}) \, \mathrm{d}V(\vec{x}) = 0. \tag{2.14}$$

By the divergence theorem, we have

$$\int_V \nabla \cdot \vec{u}(\vec{y}) \, \mathrm{d}V(\vec{y}) = \int_S \vec{u}(\vec{x}) \cdot \hat{n} \, \mathrm{d}S(\vec{x}) + \int_{S_f} \vec{u}(\vec{x}) \cdot \hat{n} \, \mathrm{d}S(\vec{x}) = 0, \tag{2.15}$$

where S_f is the surface of the control volume of the fluid, V, surrounding the solid particle. See Figure 2.2. Note that the fluid volume V is strictly outside the aggregate boundary S. The control volume could be a large sphere with a radius, r_f. Then the velocity $\vec{u}$ on S_f approaches zero with order $\mathcal{O}(1/r_f)$ and its associated stress tensor decays at the rate $\mathcal{O}(1/r_f^2)$. For large enough r_f, the surface integral on S_f in equation (2.15) is zero, implying that

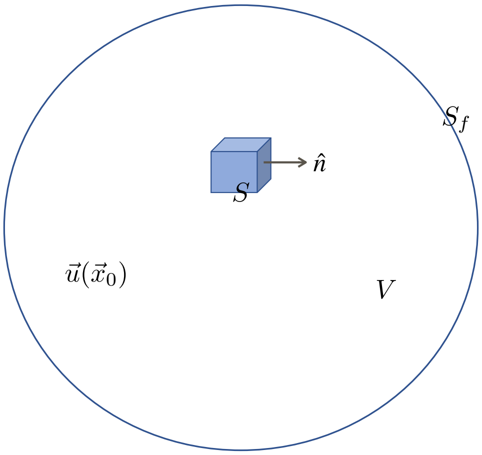

Figure 2.2: Schematic of the control volume and its surface.

$$\int_S \vec{u}(\vec{x}) \cdot \hat{n} \, \mathrm{d}S(\vec{x}) = 0.$$

Then, following (Pozrikidis, 1992), we have a complementary flow $\vec{u}_c$. By the Lorentz reciprocal identity, any two flows having the same force on the boundary satisfy

$$\int_S \vec{f}(\vec{x}) \cdot \bar{\bar{G}}(\vec{x}, \vec{x}_o) \, \mathrm{d}S(\vec{x}) - \tilde{\mu} \int_S \vec{u}_c(\vec{x}) \cdot \bar{\bar{K}}(\vec{x}, \vec{x}_o) \cdot \hat{n}(\vec{x}) \, \mathrm{d}S(\vec{x}) = 0, \tag{2.16}$$

Substituting equation (2.16) into the representation formula, equation (1.13), we obtain a flow

$$\vec{u}_{dl}(\vec{y}) = \frac{1}{8\pi}\int_S \vec{\psi}(\vec{x}) \cdot \bar{\bar{K}}(\vec{x},\vec{y}) \cdot \hat{n}(\vec{x})\, \mathrm{d}S(\vec{x}), \tag{2.17}$$

where $\vec{\psi}(\vec{x}) = \vec{u}(\vec{x}) - \vec{u}_c(\vec{x})$. When $\bar{\bar{K}}$ is a Green's function for an infinite flow, the velocity (2.17) satisfies the Stokes equation with any choice of $\vec{\psi}(\vec{x})$.

Due to our constraints to derive equation (2.17), the double-layer potential formula, $\vec{u}_{dl}$ is only valid for a particle that has a force- and torque-free body, such as a swimming microorganism. For other solid-body models, finite non-zero net force and torque models, the velocity we would like to find, $\vec{u}$, does not capture the force and torque on the surface S accurately, i.e.,

$$\vec{u}_{dl}(\vec{y}) = \vec{u}(\vec{y}) - \frac{1}{8\pi\tilde{\mu}}\vec{F}_o \cdot \bar{\bar{G}}(\vec{x}_0,\ \vec{x}_{cm}) - \frac{1}{8\pi\tilde{\mu}}\frac{\vec{Q}_o \times (\vec{y} - \vec{x}_{\mathrm{cm}})}{\|\vec{y} - \vec{x}_{\mathrm{cm}}\|^3}. \tag{2.18}$$

For the double-layer potential formula, we define the total force and torque as

$$\vec{F}_o = \frac{\tilde{\mu}}{L}\int_S \vec{\psi}(\vec{x})\, \mathrm{d}S(\vec{x}) \tag{2.19}$$

and

$$\vec{Q}_o = \frac{\tilde{\mu}}{L}\int_S (\vec{x} - \vec{x}_{cm}) \times \vec{\psi}(\vec{x})\, \mathrm{d}S(\vec{x}) \tag{2.20}$$

We multiply by $\tilde{\mu}/L$ to have the same physical meaning when the stress vector, $\vec{f}$, as we found the forces using the single-layer potential, equation (2.12). Note that equation (2.18) implies that the net force and torque associated with the velocity $\vec{u}_{dl}$ are zero. The second and third terms in equation (2.18), denoted by $\vec{u}_F$ and $\vec{u}_Q$, respectively, are a solution to the Stokes equations, except at the center of mass of the solid particle, $\vec{x}_{cm}$. The flow $\vec{u}_F$ is the velocity at a point $\vec{y}$ generated by a point force with strength $\vec{F}_0$ at $\vec{x}_{cm}$. In the same manner, the flow $\vec{u}_Q$ represents the velocity induced by the vorticity associated with the flow $\vec{u}_F$. With those two extra terms, Mikhlin 1957, p.172 (Smithies, 1959) and Power & Miranda 1987 (Power & Miranda, 1987) introduced the following double-layer potential formula,

$$\begin{aligned}\vec{u}(\vec{y}) =& \frac{1}{8\pi}\int_S \vec{\psi}(\vec{x}) \cdot \bar{\bar{K}}(\vec{x},\vec{y}) \cdot \hat{n}(\vec{x})\, \mathrm{d}S(\vec{x}) \\ &+ \frac{1}{8\pi\tilde{\mu}}\vec{F}_o \cdot \bar{\bar{G}}(\vec{x}_0,\vec{x}_{cm}) + \frac{1}{8\pi\tilde{\mu}}\frac{\vec{Q}_o \times (\vec{y} - \vec{x}_{cm})}{\|\vec{y} - \vec{x}_{cm}\|^3},\end{aligned} \tag{2.21}$$

for any points $\vec{y}$ in the fluid and strictly outside of the solid particle surface S.

Unlike the single-layer potential, the double-layer potential formula is not continuous across the surface S. We thus consider another velocity expression on the aggregate boundary surface with a jump condition (Pozrikidis, 1992),

$$\begin{aligned}\vec{u}(\vec{x}_s) = -\frac{1}{2}\vec{\psi}(\vec{x}_s) + \frac{1}{8\pi}\int_S \vec{\psi}(\vec{x}) \cdot \bar{\bar{K}}(\vec{x}, \vec{x}_s) \cdot \hat{n}(\vec{x})\, \mathrm{d}S(\vec{x}) \\ + \frac{1}{8\pi\tilde{\mu}}\vec{F}_o \cdot \bar{\bar{G}}(\vec{x}_s, \vec{x}_{cm}) + \frac{1}{8\pi\tilde{\mu}}\frac{\vec{Q}_o \times (\vec{x}_s - \vec{x}_{\mathrm{cm}})}{\|\vec{x}_s - \vec{x}_{\mathrm{cm}}\|^3},\end{aligned} \tag{2.22}$$

for the points on the surface, $\vec{x}_s \in S$.

2.3 Non-dimensionalization

For the convenience of further study, we write all equations in non-dimensional form using the following parameters:

$$\vec{x} = R_a\vec{x}', \ \ \vec{u} = U_s\vec{u}', \ \ \vec{f} = \frac{\tilde{\mu}U_s}{R_a}\vec{f}', \ \ \vec{\psi} = U_s\vec{\psi}', \ \ \vec{F}_o = \tilde{\mu}U_sR_a\vec{F_o}', \ \ \vec{Q}_o = \tilde{\mu}U_sR_a^2\vec{Q_o}'. \tag{2.23}$$

We use the values presented in Chapter 1, as we derived the Reynolds number (1.8). Neglecting inertial terms, the system of equations becomes

$$-\nabla' P_d' + \nabla'^2\vec{u}' = \vec{0} \tag{2.24}$$

$$\nabla' \cdot \vec{u}' = 0, \tag{2.25}$$

where we define the dynamic pressure as $P_d(\vec{x}) = P(\vec{x}) + \rho g\hat{k} \cdot \vec{x}$. Equation (2.3), used in both the single-layer and double-layer formulations, is thus non-dimensionalized as

$$\vec{u}'(\vec{x}_s') = \frac{\vec{U}_a}{U_s} + \frac{\vec{\Omega}R_a}{U_s} \times (\vec{x}_s' - \vec{x}_{cm}') = \vec{U}_a' + \vec{\Omega}' \times (\vec{x}_s' - \vec{x}_{cm}') \tag{2.26}$$

Furthermore, dimensionless forms of the single-layer potential formula for the velocity at a point outside of the surface S is

$$\vec{u}'(\vec{y}') = -\frac{1}{8\pi}\int_{S'} \vec{f}'(\vec{x}') \cdot \bar{\bar{G}}'(\vec{x}', \vec{y}')\, \mathrm{d}S'(\vec{x}'). \tag{2.27}$$

equations for the non-dimensional force and angular velocity, given dimensionally in equation (2.12), become

$$\vec{F}_o' = \vec{F}_o\frac{1}{\tilde{\mu}U_sR_a} = \int_{S'} \vec{f}'(\vec{x}')\, \mathrm{d}S'(\vec{x}') \tag{2.28}$$

$$\vec{Q}_o' = \vec{Q}_o\frac{1}{\tilde{\mu}U_sR_a^2} = \int_{S'} (\vec{x}' - \vec{x}_{cm}') \times \vec{f}'(\vec{x}')\, \mathrm{d}S'(\vec{x}'). \tag{2.29}$$

We also make dimensionless the double-layer potential in a similar manner,

$$\vec{u}(\vec{y}') = \int_{S'} \vec{\psi}'(\vec{x}') \cdot \overset{=}{K}'(\vec{x}', \vec{y}')\, \mathrm{d}S'(\vec{x}') + \vec{F'}_o \cdot \overset{=}{G}'(\vec{x}'_0, \vec{x}'_{cm}) + \frac{1}{8\pi} \frac{\vec{Q'}_o \times (\vec{y}' - \vec{x}'_{\mathrm{cm}})}{\|\vec{y}' - \vec{x}'_{\mathrm{cm}}\|^3}, \tag{2.30}$$

for points outside of S, and

$$\begin{aligned} \vec{u}(\vec{x}'_s) = -\frac{1}{2}\vec{\psi}'(\vec{x}'_s) + \frac{1}{8\pi} \int_{S'} \vec{\psi}'(\vec{x}') \cdot \overset{=}{K}'(\vec{x}', \vec{x}'_s) \cdot \hat{n}(\vec{x})\, \mathrm{d}S'(\vec{x}') \\ + \vec{F'}_o \cdot \overset{=}{G}'(\vec{x}'_s, \vec{x}'_{cm}) + \frac{1}{8\pi} \frac{\vec{Q'}_o \times (\vec{x}'_s - \vec{x}'_{\mathrm{cm}})}{\|\vec{x}'_s - \vec{x}'_{\mathrm{cm}}\|^3}, \end{aligned} \tag{2.31}$$

for points on S. The non-dimensional force and torque, in this case, are

$$\vec{F}'_o = \int_{S'} \vec{\psi}'(\vec{x}')\, \mathrm{d}S(\vec{x}') \tag{2.32}$$

$$\vec{Q}'_o = \int_{S'} \vec{\psi}'(\vec{x}') \cdot (\overset{\equiv}{\epsilon} \cdot \vec{x}')\, \mathrm{d}S(\vec{x}'), \tag{2.33}$$

which were given dimensionally, in equation (2.19).

2.4 Numerical methods

When solving for the velocity field exterior to a solid object or an aggregate, one may either prescribe the translation velocity, $\vec{U}'_a$, and angular velocity, $\vec{\Omega}'$, of the object or prescribe the total force and torque. We found the analysis easier to perform when setting $\vec{U}'_a$ and $\vec{\Omega}'$ to known values, providing us with the velocity on the surface of the object via equation (2.26). We thus know $\vec{u}'$ on the left-hand-side of equations (2.27) and (2.31). Provided we can evaluate the surface integrals, we may then solve for the unknown stress vector, $\vec{f}'$, or density, $\vec{\psi}'$, respectively. Once these are found, we can evaluate the velocity of the fluid at any point exterior to the aggregate using equations (2.27) or (2.30) and compute the force and torque via equations (2.28) and (2.29), or equations (2.32) and (2.33).

Because we consider aggregates that are composed of cubic particles, their surface is simply a collection of squares. In both the single and double-layer potential approach, we impose a velocity at the center of each square on the surface, $\vec{x}_{sq,i}$, where $i = 1, 2, \cdots, N_f$, with N_f denoting the total number of square faces of an aggregate. We thus need to compute integrals of the form

$$\vec{I}(\vec{x}'_{sq,i}) = \int_{S'} \vec{q}'(\vec{x}') \cdot \overset{=}{\vec{J}}(\vec{x}', vecx'_{sq,i})\, \mathrm{d}S'(\vec{x}'). \tag{2.34}$$

Here, $\vec{q}$ represents either $\vec{f}$ or $\vec{\psi}$, and $\bar{\bar{J}}$ stands for either $\bar{\bar{G}}$ or $\bar{\bar{\bar{K}}} \cdot \hat{n}$, depending on if the single or double-layer method is used, respectively. To allow an exact analytic computation of the integrals, we assume that on the kth square face, the vector $\vec{q}'(\vec{x}') = \vec{q}'_k$ is constant, for $k = 1, 2, \ldots, N_f$. The surface integrals over the entire aggregate may then be discretized as

$$\vec{I}(\vec{x}'_{sq,i}) = \sum_{k=1}^{N_f} \vec{q}'_k \int_{S'_k} \bar{\bar{J}}(\vec{x}', \vec{x}'_{sq,i}) \, \mathrm{d}S'(\vec{x}') = \sum_{k=1}^{N_f} \vec{q}'_k \, \bar{\bar{\Pi}}'_{i,k}. \tag{2.35}$$

where the coefficients $\bar{\bar{\Pi}}'_{i,k}$ are constant. These constants may be computed analytically, and the corresponding formulas are given in Appendix A. This discretization is equivalent to using a two-dimensional mid-point rule to estimate the integrals. Equation (2.35) is linear in $\vec{q}'_k$, resulting in a dense linear system of $3N_f$ equations for each of the N_f three-dimensional unknown vectors $\vec{q}'_k$ (either the stress vector or the density).

We note that the numerical method presented here describes the fluid flow around a single aggregate but a similar procedure can be employed to determine the flow exterior to several aggregates. Each aggregate then has its own translation and angular velocity vectors, as well as its own force and torque. In that case, it is more natural to set the force and torque on each particle, using equations (2.28) and (2.29) or equations (2.32) and (2.33), and then solve for the translation and angular velocities, adding two vector equations per aggregate to the linear system.

We now discuss specific features of the single- and double-layer potential methods. For the single-layer potential, we have $\bar{\bar{J}}(\vec{x}', \vec{x}'_k) = \bar{\bar{G}}(\vec{x}', \vec{x}'_k)$, and $\vec{q}'_k = \vec{f}'_k$. In that case, the $3N_f \times 3N_f$ linear system obtained is not full rank. Stress vectors are only found up to a constant multiple of the local normal vectors since a stress vector given by a constant multiple of the local normals results in a zero velocity at the interface and a zero net force and torque. To obtain a unique solution, we add an equation enforcing that

$$\sum_{k=1}^{N_f} \vec{f}'_k \cdot \hat{n}_k = 0, \tag{2.36}$$

where $\hat{n}_k$ is the outer normal on each face. The resulting $(3N_f + 1) \times 3N_f$ system has a unique solution vector $\vec{f}'_k$.

For the double-layer potential, the unknown density, $\vec{\psi}'_k$, is found using the same discretization (2.35) applied to equation (2.31), resulting in a system with no rank deficiency. See Appendix A. However, the values of the total force and torque terms must be solved simultaneously with the unknown density, resulting in a slightly larger system of size $3(N_f + 2) \times 3(N_f + 2)$. These additional equations, (2.32) and (2.33), are discretized as,

$$0 = \int_{S'} \vec{\psi}'(\vec{x}')\, \mathrm{d}S'(\vec{x}') - \vec{F}'_o = A' \sum_{k=1}^{N_f} \vec{\psi}'_k - \vec{F}'_o, \tag{2.37}$$

$$0 = \int_{S'} \vec{\psi}'(\vec{x}') \cdot (\bar{\bar{\bar{\epsilon}}} \cdot \vec{x}')\, \mathrm{d}S'(\vec{x}') - \vec{Q}'_o = A' \sum_{k=1}^{N_f} \vec{\psi}'_k \cdot \bar{\bar{\bar{\epsilon}}} \cdot \vec{x}'_k - \vec{Q}'_o \tag{2.38}$$

where $A' = 4$ is the non-dimensional area of each square.

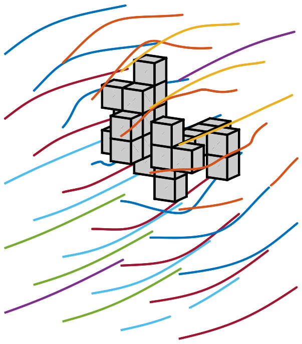

Figure 2.3: Sample streamlines of flow past a 20-cube aggregate. The aggregate is assumed to move horizontally, into the page and to the right.

In Figure 2.3, we present sample streamlines computed with this numerical method. Here, we show results obtained with the single-layer potential method where the aggregate is assumed to move horizontally with $\vec{U}'_a = (1, 0, 0)$ and $\vec{\Omega}' = (0, 0, 0)$. The double-layer potential would give visually identical results. Once the velocity was computed, the streamlines were obtained by performing a second-order Runge-Kutta time integration. The streamlines, computed in the frame of reference of the aggregate, can be seen to be deflected by the object, with weaker deflections further away from the aggregate.

2.4.1 Validation and Comparison

We proceed to validate and compare our implementation of the single and double-layer approaches. Although the single-layer approach is somewhat simpler to implement, it has been found to yield linear systems with larger condition numbers when

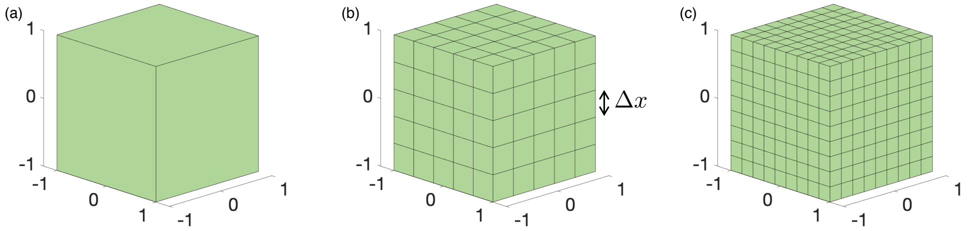

Figure 2.4: Cubes of various resolutions used for validation. All three cubes have the same volume and contain (a) 1 interior cube with length $\Delta x = 2$, (b) $5^3 = 125$ interior cubes with length $\Delta x = 2/5$, and (c) $9^3 = 729$ interior cubes with length $\Delta x = 2/9$.

integrated using boundary element methods, though with seemingly little impact on its accuracy (Youngren & Acrivos, 1975; Ingber & Mammoli, 1999). We consider a simple system where resolution may easily be varied and compute the flow around a single large cube, subdivided into smaller collated cubes, as shown in Figure 2.4. We define $\Delta x = 2/N_x$, where N_x is the number of cubes in each linear dimension, and increase the resolution by increasing N_x. The prescribed translation and angular velocities are kept constant at $\vec{U}'_a = (0, 0, -1)$ and $\vec{\Omega}' = (0, 0, 0)$, respectively. We then compute and compare the total force and torque on the cube.

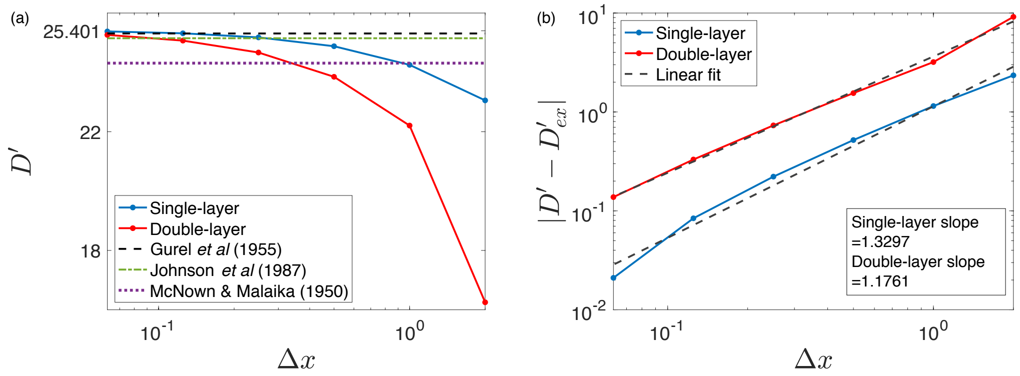

Figure 2.5: (a) Drag on a cube as a function of Δx for both the single- and double-layer methods. (b) The error of the drag as Δx is varied, shown on a log-log scale. Dashed lines are linear fits to the data. The error is computed by taking the difference between the limit shown in (a), $D'_{ex} = 25.401$, and drag values, D' when $\Delta x = 2, 1, 0.5, 0.25, 0.125$, and 0.0625.

In Figure 2.5(a), we present the non-dimensional drag, D', the z'-component of the total force on the cube,

$$D' = -\vec{F}_o' \cdot \frac{\vec{U}_a}{||\vec{U}_a||} = \vec{F}_o' \cdot \hat{k} = \frac{\vec{F}_o \cdot \hat{k}}{\tilde{\mu} U_s L}, \tag{2.39}$$

as computed by both methods, using equations (2.28) and (2.32), for various resolutions. We first observe that both methods converge to the same limit value of $D' \approx 25.401$ as we decrease Δx. These results agree very well with the observations of Gurel *e*t al. (Gurel, Ward, & Whitmore, 1955) who found a drag of 25.311, and with the empirical relation proposed by Johnson *e*t al. (D. L. Johnson, Leith, & Reist, 1987), which yields a drag of 25.150. Values given in earlier literature are similar but somewhat smaller, with McNown & Malaika (McNown & Malaika, 1950) reporting a drag of 24.311. These literature values are also plotted in Figure 2.5(a).

Figure 2.5(b) presents the error relative to the limit value of $D'_{ex} = 25.401$ for both methods. We notice that the convergence rate is similar in both methods, showing a convergence rate slightly higher than one. Typically, one expects to observe a quadratic order of convergence using the mid-point integration rule. However, the order of convergence is likely lower here owing to the presence of edges and corners, which are not treated specially as a resolution is increased.

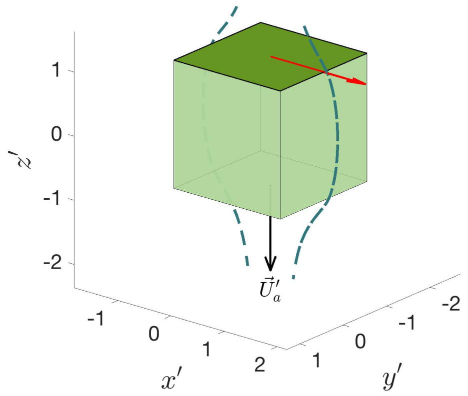

Figure 2.6: The shaded face is the domain where the stress vector and density shown in Figure 2.7 and 2.8 are computed. The red arrow shows the x-axis used in Figure 2.9. Sample streamlines, discussed in Section 2.4.2, are shown as dashed lines. We also show the translation vector, $\vec{U}_a'$.

The single-layer method is seen to be more accurate than the double-layer method, with an error approximately four times smaller. In other words, a similar degree of accuracy can be obtained with the single-layer method when using a value of Δx four times greater than the double-layer method. The other components of the force acting on the cube, as well as the total torque, are expected to be exactly zero because of the symmetry of the cube. In our computations, the torque and the other components of the force never exceed 10^{-10}, as anticipated.

We now consider point-wise quantities such as the stress vector, density function, and velocity on the surface of the cube and in the fluid exterior of the cube. These quantities are computed in the plane $z' = 1$, which coincides with the face of the cube normal to the incoming flow, as shown in Figure 2.6.

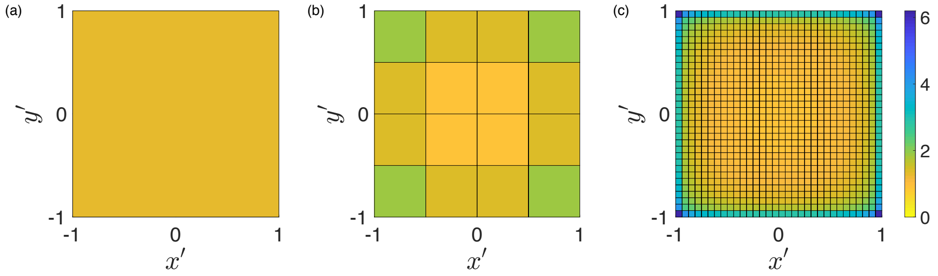

Figure 2.7: Vertical (z') component of the stress vector, $\vec{f}'$, computed using the single-layer potential shown at $z' = 1$, as illustrated in Figure 2.6. The resolution is: (a) $\Delta x = 2$, (b) $\Delta x = 0.5$, and (c) $\Delta x = 0.0625$. The color bar is the same for all three figures.

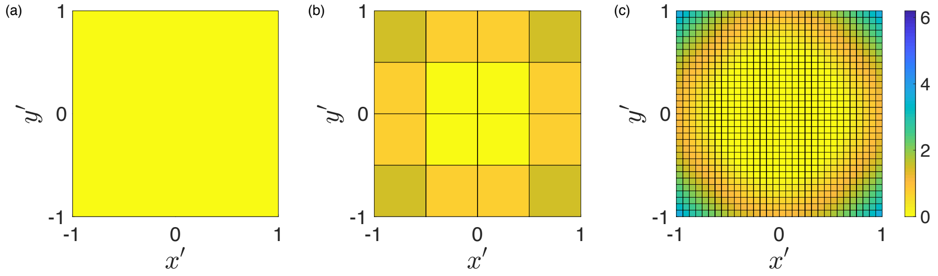

Figure 2.8: Vertical (z') component of the density, $\vec{\psi}'$, computed using the double-layer potential, shown at $z' = 1$, as illustrated in Figure 2.6. The resolution is: (a) $\Delta x = 2$, (b) $\Delta x = 0.5$, and (c) $\Delta x = 0.0625$. The color bar is the same for all three figures and the same as in Figure 2.7.

We show in Figure 2.7 and 2.8 the z'-component of the stress vector, $\vec{f}'$, and of the density, $\vec{\psi}'$, respectively. When varying the resolution of the cube, we obtain N_x^2 different values of the stress vector or density for each side of the cube; each assumed to be constant on a square with side length Δx. Comparing Figs. 2.7 and 2.8, it is clear that the stress vector is better approximated by a constant value than the density. As can be seen in both Figure 2.7 and 2.8, convergence is slowest at the edges and even more so at the corners. Despite the rapid variations of the stress vector and density at the corners, the drag is seen to converge with increased resolution, see Figure 2.5, though perhaps with a slower order of convergence than would be expected from a mid-point rule. The single-layer potential approach thus provides a good approximation of the total drag even at low resolution. In contrast, the double-layer potential method finds a density that varies to a greater extent over the face of the higher-resolution cube, making low-resolution estimates less accurate. On the other hand, the variations near the corners are smoother, which could make this method a better choice if one were focusing on the behavior at the edges or corners. These observations are consistent with the single-layer approach resulting in more accurate computations of the drag than the double-layer approach when using the same resolution.

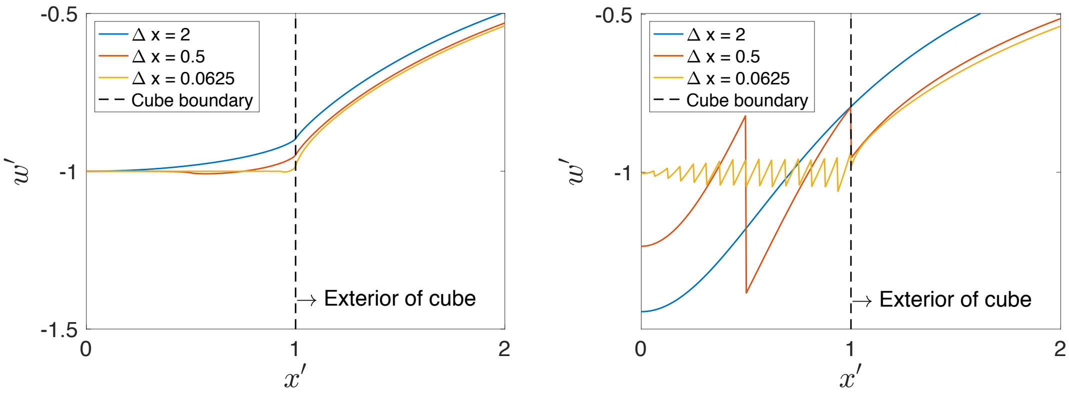

Figure 2.9: Vertical (z') component of the velocity, denoted by w', along the line $(x', 0, 1)$ as illustrated in Figure 2.6. We show three different resolutions for the (a) single-layer method and (b) double-layer method.

We next present analysis of the $z'-$component of the velocity, w', when the cube has the same translation velocity, $\vec{U}_a' = (0, 0, -1)$. In Figure 2.9, we present this velocity along the line $(x', 0, 1)$, shown in Figure 2.6 as the red arrow, as we vary the resolution of the cube for both the single-layer and double-layer approaches. When using the single-layer potential, we compute the velocity for all points using equation (2.27). For the double-layer potential approach, we compute the velocity at points on the surface of the cube using equation (2.31) and at points in the fluid exterior to the cube using equation (2.30). In Figure 2.9, dashed lines represent the edge of the cube, i.e., points $x' \in [0,1]$ are on the cube surface and points $x' \in (1,2]$ are exterior to the cube. Since we impose the translation velocity, $\vec{U}'_a$ at the center of each square, we expect that $w' = -1$ for $x' \in [0,1]$. We observe that on the cube surface, the single-layer method, shown in Figure 2.9(a), results in smoother velocities than the double-layer method, shown in Figure 2.9(b). In Figure 2.9(a), as Δx decreases, the velocities on the surface of the cube converge to -1. The velocity on the edge of the surface, at $x' = 1$, does not agree exactly with the expected value, though it approaches -1 as Δx decreases. On the other hand, the double-layer approach has discontinuous oscillations of the velocity on the surface. This is due to our assumption of locally constant, and thus discontinuous, $\vec{\psi}'$, which directly affects the velocity in equation (2.31). The oscillations decrease in amplitude as Δx decreases, and the velocity exterior to the cube is smooth. The discrepancy with the expected velocity at the edge of the cube, $x' = 1$, is greater than for the single-layer approach.

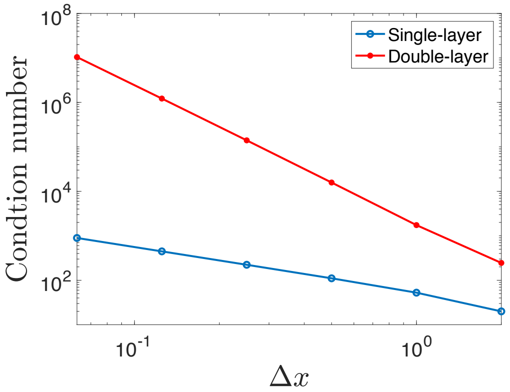

Figure 2.10: Comparison of the condition number for the linear system of both the single-layer and double-layer methods as the resolution of the cube is varied.

We conclude the comparison of the two methods by considering their computational complexity. It has been observed that Fredholm integral equations of the first kind, such as that associated with the single-layer potential, often lead to ill-posed numerical methods when the surface integral is discretized (Delves et al., 1974; Karrila & Kim, 1989). The main challenge is dealing with the singularity of the the integral kernel. However, in our method, we compute the surface integrals analytically over each square so that the kernel singularities are integrated exactly. In addition, we constrain the system to have a unique solution through equation (2.36). We compare the condition number of the linear system of each of our two methods for various resolutions in Figure 2.10. We find that the condition number of the single-layer method is approximately inversely proportional to Δx. On the other hand, the condition number of the double-layer method is approximately inversely proportional to $(\Delta x)^3$ and is thus much greater.

Based on our findings of more accurate drag, smoother and more accurate velocity, and smaller condition numbers, we conclude that the single-layer potential approach is more appropriate to model flow around aggregates made of cubic particles. In the remainder of this chapter, we, therefore, present results obtained using the single-layer approach.

2.4.2 Streamlines

To gain a better understanding of the flow around a cube, we present the streamlines generated when $\vec{U}'_a = (0, 0, -1)$. We show the streamlines around the cube in the frame of reference of the cube for $y' = 0$ in Figure 2.11 (see Figure 2.6 for the exact location of the face and sample streamlines). To compute the streamlines, we first obtain the values of stress vector, $\vec{f}'(\vec{x}'_s)$, on each square face of the cube using equation (2.27). We then chose initial positions below the cube and used a second-order Runge-Kutta method to advance the positions in time using the corresponding velocities computed using equation (2.27) at each position. We compare the streamlines with four different resolutions of the cube; $\Delta x = 2, 1, 0.5$, and 0.25. For the cube with $\Delta x = 2$, streamlines are seen to enter the interior of the cube.

In Figure 2.11 (a), we obtained the most inaccurate streamlines, violating our solid boundary surface assumption. This implies that we need more than one cube to model an aggregate. We observe the major error occurs at the corner of the cubes. We interpret the error at low resolution as smoothing of the cube. As we increase the resolution, the streamlines remain exterior to the cube. Moreover, higher resolutions result in streamlines following the cube boundary more accurately, showing the convergence of the method.

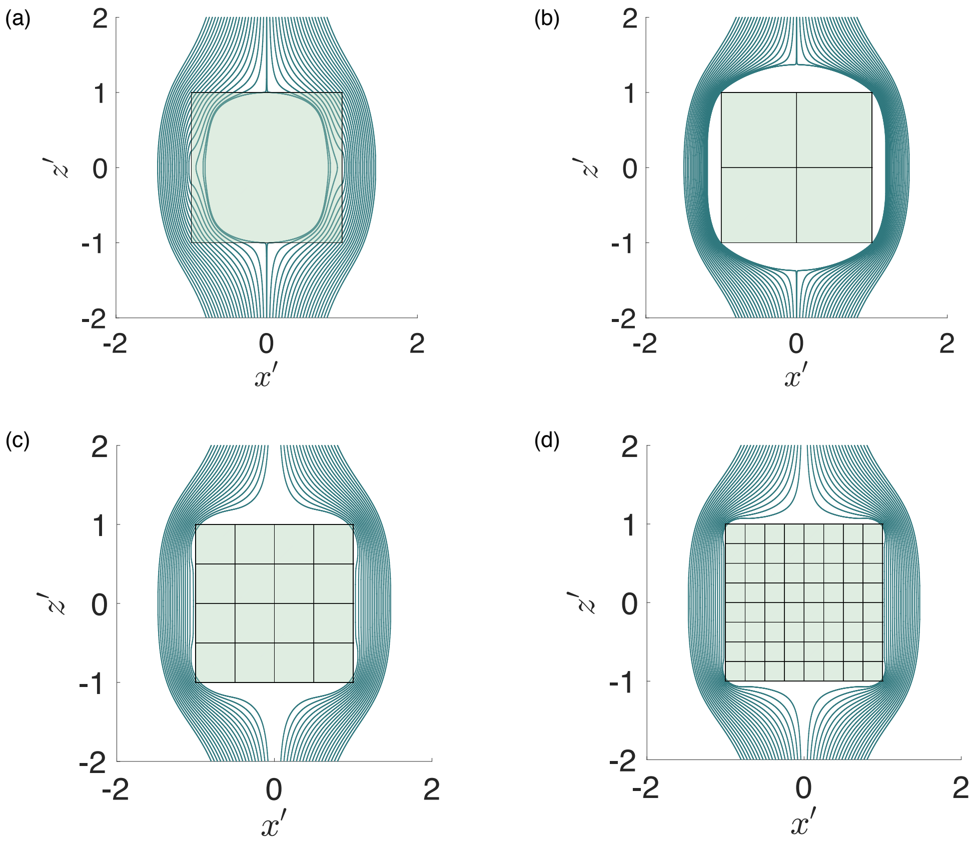

Figure 2.11: Streamlines around a cube with varying resolution moving in the z'−direction. The resolution is: (a) $\Delta x = 2$, (b) $\Delta x = 1$, (c) $\Delta x = 0.5$, and (d) $\Delta x = 0.25$.

2.5 Forces on Aggregates Subject to a Background Flow

In this section, we present the response of the aggregates when subjected to various flow fields. We consider an aggregate at rest, with boundary condition $\vec{u}' = 0$ on the surface of the aggregate, subject to a background flow. Three common background flows are considered, which can be combined to provide an approximation of any general flow to first order in space: $\vec{U}'_{bg}(\vec{x}) = -\vec{U}'_a - \vec{\Omega}' \times \vec{x}' + \bar{\bar{M}}' \cdot \vec{x}'$, the primes indicating dimensionless quantities as above. Here, $-\vec{U}'_a$ is the translation velocity of the flow past an aggregate or equivalently when changing the frame of reference, a constant settling velocity $\vec{U}'_a$ of the aggregate in a fluid at rest. Similarly, $-\vec{\Omega}'$ is the constant angular velocity of a rotating flow around an aggregate, or equivalently when changing the frame of reference, the constant angular velocity of a rotating aggregate in a fluid at rest. Lastly, $\bar{\bar{M}}'$ is a traceless, symmetric tensor that induces a straining flow around the aggregate. In all three cases, to solve for the response of the aggregates, we decompose the fluid velocity as $\vec{u}' = \vec{U}'_{bg} + \vec{U}'_c$, where the correction velocity, $\vec{U}'_c$, decays to zero at infinity and satisfies $\vec{U}'_c = -\vec{U}'_{bg}$ on the surface of the aggregate. Using this formulation allows for this correction to be computed via the single-layer potential boundary integral as described above in Sections 2.3 and 2.4.

2.5.1 Translation Flow

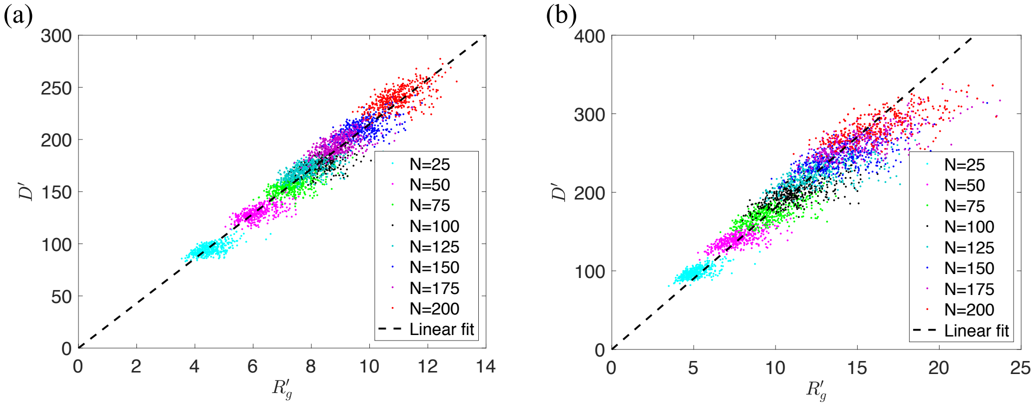

Figure 2.12: Non-dimensional drag of aggregates in a constant flow, $\vec{U}'_{bg} = -\vec{U}'_a = (0, 0, 1)$, as a function of gyration radius R'_g for aggregates of different sizes, N. We present in (a) the drag of individually-added-aggregates (IAA) and in (b) the drag of cluster-cluster-aggregates (CCA). The dashed lines are least-square linear fits: in (a) $D' = 21.47 R'_g$ and in (b) $D' = 18.04 R'_g$.

We first consider a constant background velocity, $\vec{U}'_{bg}(\vec{x}') = -\vec{U}'_a = (0, 0, 1)$. In Figure 2.12, we present the non-dimensional drag on the aggregate, D', as defined in equation (2.39), as a function of the non-dimensional gyration radius, R'_g, of each aggregate. We show in Figure 2.12(a) the drag on aggregates formed by individual random walkers (IAA) and in Figure 2.12(b) the drag on aggregates formed by cluster aggregation (CCA). Recall that aggregates formed by individually-added random walkers tend to be more compact. The drag appears to scale linearly with the gyration radius for both types of aggregates, as would be expected from dimensional considerations for the proper measure of the size of an aggregate. Note that for all the fits presented in this section, we compute the coefficient of determination, $\mathbf{R}^2$, using either the gyration or maximum radius as an independent variable to assess how closely each model fits the data.

To verify this linear relationship between the drag and the gyration radius, we found the slope of D' as a function of R'_g on a log-log plot, giving the best exponent, α, in the relation $D' \sim (R'_g)^{\alpha}$. This confirmed that a linear fit was optimal for IAA, finding $\alpha = 1.00$, and found a somewhat smaller exponent for CCA, with $\alpha = 0.85$. Assuming a linear relation, we find for individual aggregation (IAA) that a least-square fit has a slope of 21.47 with a coefficient of determination of $\mathbf{R}^2 = 0.95$ (Figure 2.12(a)) For cluster aggregation (CCA), we find a best-fit line with a slope of 18.04 and a corresponding coefficient of determination of $\mathbf{R}^2 = 0.86$ (Figure 2.12(b)).

These results are consistent with experimental results, which showed a linear relationship between the drag on an aggregate and the square root of A'_p, the two-dimensional projected area of the aggregate (Tang, Greenwood, & Raper, 2002). In addition to computing the drag as a function of the gyration radius, we computed the drag of aggregates as a function of their projected area. We found that A'_p was not a good predictor of the drag experienced by the aggregate. In particular, for aggregates containing a fixed number of cubes, we observed no correlation between the projected area and the drag experienced by the aggregate. A similar observation holds for the torque and straining force discussed below, and as a result, we choose to present all of our results in terms of either the maximum or gyration radius.

Although the relationship between the drag and gyration radius is nearly linear, there appears to be further structure in the data obtained, as is particularly visible for CCA in Figure 2.12(b). For an aggregate composed of a fixed number of cubes, N, the drag increases linearly with aggregate size but at a slower rate than when N is also allowed to vary. To better characterize this dependency, we introduce a rescaled non-dimensional drag that takes into account the difference between the gyration radius of a given aggregate and the mean gyration radius of all aggregates with the same number of cubes. We denote the average gyration radius for aggregates of N cubes as $\bar{R}'_g(N)$. Similarly, we define an average maximum radius for aggregates made of N cubes as $\bar{R}'_m(N)$. We may then define the departure from these average values as

$$\sigma_g = \frac{R'_g - \bar{R}'_g}{\bar{R}'_g} \qquad \text{and} \qquad \sigma_m = \frac{R'_m - \bar{R}'_m}{\bar{R}'_m}.$$

These measures are positive when the aggregate is more spread out than the mean aggregate size and negative when the aggregate is more compact than the mean. We use

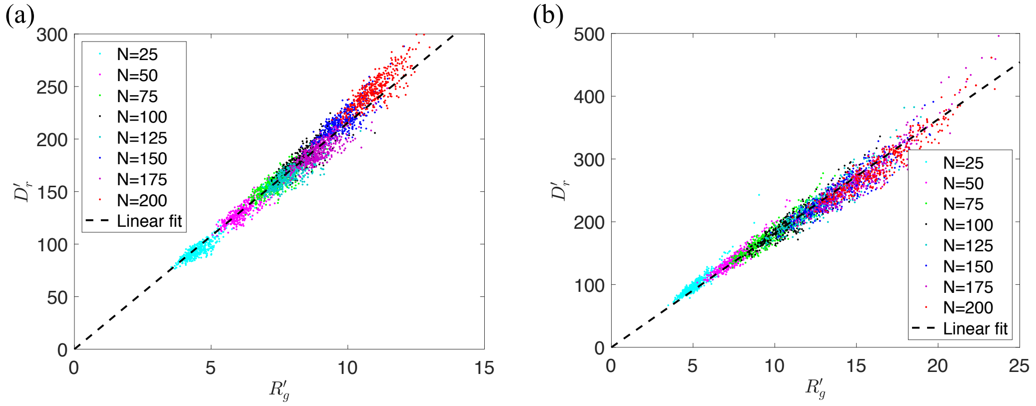

Figure 2.13: Rescaled non-dimensional drag, D'_r, as a function of gyration radius R'_g for (a) individually-added aggregates (IAA) and for (b) cluster-cluster-aggregates (CCA). The rescaled drag, D'_r, is defined in equation (2.40), and the fits to the data, plotted as dashed lines, are given in equation (2.41) for (a) and in equation (2.42) for (b).

these measures to define a rescaled drag that accounts for the variability in the aggregate radius as

$$D'_r = \frac{D'}{1 + \gamma \sigma_g} \, , \tag{2.40}$$

where γ is an empirical parameter that we fit based on the data. To optimize the collapse, we choose γ to maximize the correlation coefficient between the rescaled drag and the gyration radius.

As seen in Figure 2.13 the data collapses better. For IAA, we find $\gamma = -0.43$, with a best-fit line of $D'_r = 21.55 R'_g$, which improves the coefficient of determination to 0.97, which is a relatively small gain as the data was already nearly linear. This negative value of γ indicates that less compact aggregates experience more drag than more compact aggregates when composed of the same number of cubes. The drag is thus well described by

$$D' = 21.55 \left(1 - 0.43 \frac{R'_g - \bar{R}'_g}{\bar{R}'_g} \right) R'_g \, . \tag{2.41}$$

where the mean gyration radius is $\bar{R}'_g = 1.32 N^{0.39}$, as described in Section 3. For CCA, the same procedure yielded $\gamma = -0.64$, and the resulting collapse is shown in Figure 2.13(b). The rescaled drag follows a much improved linear relationship as a function of the gyration radius, with a slope of 18.16 and a coefficient of determination of $\mathbf{R}^2 = 0.97$. A complete description of the drag for CCA is thus

$$D' = 18.16 \left(1 - 0.64 \frac{R'_g - \bar{R}'_g}{\bar{R}'_g}\right) R'_g \tag{2.42}$$

where the mean gyration radius is $\bar{R}'_g = 0.85N^{0.56}$. A similar dependence was found when replacing the gyration radius with the maximum radius or the square root of the projected area. However, the coefficients of determination were then lower, by approximately 2%, and the best-fit exponents, α, were lower for the gyration radius and further from one for the projected area (lower for IAA, higher for CCA). This indicates that the gyration radius is a better descriptor of the size of an aggregate when considering the drag.

2.5.2 Rotating flow

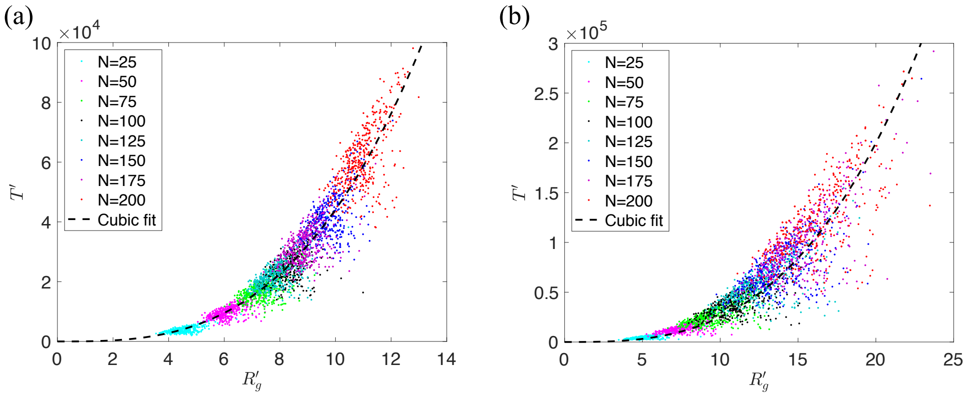

Figure 2.14: Non-dimensional torque, T', defined in equation (2.43), as a function of gyration radius, R'_g, for aggregates composed of a varying number of cubes, N. In (a) individually-added-aggregates (IAA) are presented, and in (b) cluster-cluster-aggregates (CCA) are presented. The dashed lines are least-square cubic fits: in (a) $T' = 44.12(R'_g)^3$ and in (b) $T' = 24.98(R'_g)^3$.

In Figure 2.14, we present the non-dimensional torque as a function of gyration radius for aggregates subject to a rotating background flow, $\vec{U}'_{bg}(\vec{x}') = -\vec{\Omega}' \times \vec{x}'$. We present only the component of the torque parallel to $\vec{\Omega}'$, as the other two components both average to zero. This component, T', is non-dimensionalized using the angular velocity,

$$T' = -\vec{Q}'_o \cdot \frac{\vec{\Omega}'}{||\vec{\Omega}'||} \quad \text{and} \quad \vec{Q}'_o = \frac{\vec{Q}_o}{\tilde{\mu}||\vec{\Omega}||L^3} \tag{2.43}$$

Here, we expect a cubic dependence of the torque on a properly chosen measure of the size of the aggregate, in contrast to the linear dependence of the drag as described in Section 2.5.1. This is because computing a torque rather than a force increases the order of dependence on the gyration radius by one. In addition, this calculation is based on an imposed angular velocity, $\vec{\Omega}'$, rather than a translation velocity, which also increases the order of the dependence on the gyration radius by one. We verified that a cubic fit was the most appropriate by finding the slope on a log-log plot of the torque as a function of gyration radius, yielding the best exponent α in the relation $T' \sim (R'_g)^\alpha$. This confirmed that a cubic fit was optimal for IAA, with $\alpha = 3.00$, and again we observed a somewhat smaller exponent for CCA, with $\alpha = 2.68$, indicating that the torque of CCA shows a slower average growth. Furthermore, for CCA, as can be seen in Figure 2.14(b), there is noticeably more variability. Assuming a cubic fit, we find for the IAA a least-square fit of $T' = 44.12(R'_g)^3$ with the coefficient of determination $\mathbf{R}^2 = 0.91$ and for the CCA a least-square fit of $T' = 24.98(R'_g)^3$ with the coefficient of determination $\mathbf{R}^2 = 0.81$. Here too, a similar dependence was found when replacing the gyration radius with the maximum radius or projected area, though again with smaller coefficients of determination and best-fit exponents further from three as expected from dimensional analysis, so that the gyration radius is also a more useful descriptor of the size of an aggregate when studying the torque.

2.5.3 Extensional flow

We now consider the response of an aggregate to an extensional flow, $\vec{U}'_{bg}(\vec{x}') = \bar{\bar{M}}' \cdot \vec{x}'$. In such a background flow, for an object with no preferred orientation, the drag and torque both average to zero. However, the aggregate will be under effective tension or compression, an effect that could lead to rupture. Quantifying these forces is relevant to the formation and breakup of marine aggregates. We, therefore, define a straining force vector, $\vec{E}$, that quantifies this effect. We non-dimensionalize this force using the largest eigenvalue in the magnitude of the matrix $\bar{\bar{M}}$ which we denote by $|\lambda|$ and obtain

$$\vec{E}' = \frac{\vec{E}}{\tilde{\mu}|\lambda|L^2}. \tag{2.44}$$

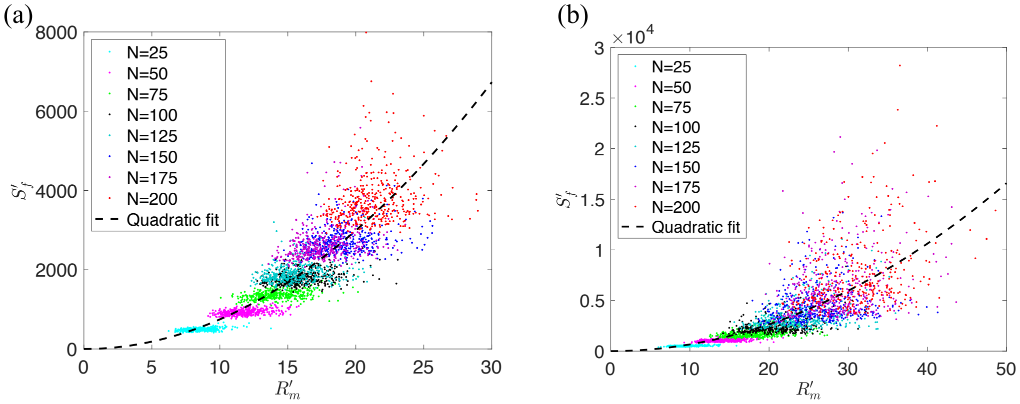

Figure 2.15: Non-dimensional straining force, S'_f, defined using equations (2.44) and (2.45), as a function of the maximum radius, R'_m, for aggregates of different sizes N. In (a) individually-added-aggregates (IAA) and (b) cluster-cluster-aggregates (CCA) are presented. The dashed lines are least-square quadratic fits: in (a) for IAA, $S'_f = 7.48(R'_m)^2$ and in (b) for CCA, $S'_f = 6.64(R'_m)^2$.

The straining force may be decomposed as $\vec{E}' = E'_1\hat{v}_1 + E'_2\hat{v}_2 + E'_3\hat{v}_3$, where the $\hat{v}_i$ are the real, orthonormal eigenvectors in the spectral decomposition of $\bar{\bar{M}}'$, which is always possible since $\bar{\bar{M}}'$ is symmetric. The components of $\vec{E}'$ are then defined as

$$E'_i = \frac{1}{2}\left(\int_{S'} |\vec{f}' \cdot \hat{v}_i| \, dS' - \left|\int_{S'} \vec{f}' \, dS'\right| \cdot \hat{v}_i\right), \tag{2.45}$$

where $\vec{f}' \cdot \hat{v}_i$ is the projection of the stress vector in the direction of the eigenvector $\hat{v}_i$. This straining force is a measure of how much stress imposed in one direction is also applied in the opposite direction resulting in a strain on the aggregate. The factor of $1/2$ accounts for the double counting of the tensile or compressive forces when integrating the stress vector in the direction of, and opposite to, the vector $\hat{v}_i$. We have subtracted the component of the net force in each direction to obtain a straining force that is independent of the net force on the object. In the results shown in this section, we consider two-dimensional extensional flows, for which the eigenvalues are -1 in the x'-direction, 1 in the y'-direction, and 0 in the z'-direction. We present the component of the straining force in the y'-direction, denoted as S'_f.

For the straining force, dimensional considerations lead us to expect a quadratic dependence on an appropriate measure of the aggregate's size. However, we found that the slope of the straining force as a function of gyration radius on a log-log plot, giving the exponent α in the relation $S'_f \sim (R_g)'^{\alpha}$, yielded values greater than two for both IAA and CCA, with exponents of 2.1 and 2.2, respectively. In contrast, using the maximum radius as a measure of the aggregate's size resulted in a dependence that was much closer to being quadratic, with best fits on the growth exponent giving $S'_f \sim (R'_m)^{1.98}$ for IAA and $S'_f \sim (R'_m)^{2.01}$ for CCA. We, therefore, present the data as a function of the maximum radius rather than the gyration radius, as R'_m appears to be a better predictor of the straining force. In Figure 2.15, we present S'_f for aggregates of different sizes as a function of the maximum radius, R'_m. The dashed lines in Figure 2.15 are quadratic fits to the data as a function of maximum radius and we find best fits of $S'_f = 7.48(R'_m)^2$ for IAA with the coefficient of determination of $\mathbf{R}^2 = 0.74$, and $S'_f = 6.64(R'_m)^2$ with the coefficient of determination of $\mathbf{R}^2 = 0.56$ for CCA. For both IAA and CCA, we observe that if N is held constant and the maximum radius is varied, the growth of the straining force seems to be significantly slower than quadratic. This once again suggests a rescaling as in Section 2.5.1.

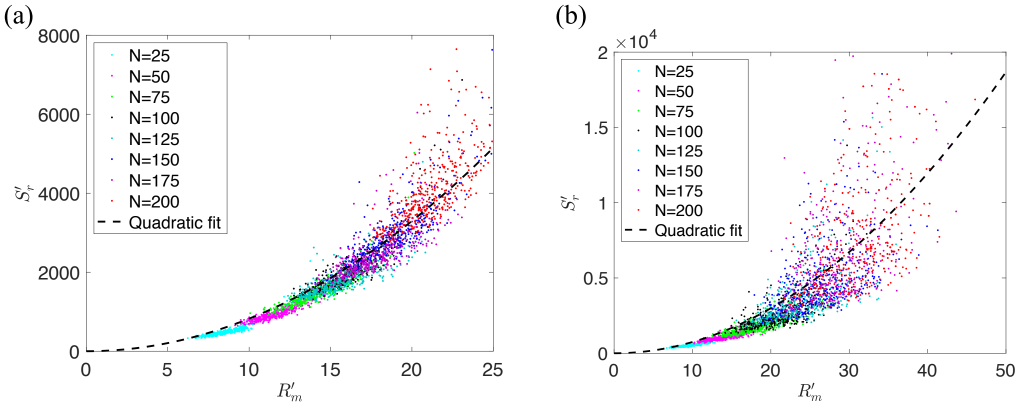

Figure 2.16: Rescaled non-dimensional straining force, S'_r, as a function of maximum radius R'_m for aggregates of different sizes N. In (a) individually-added-aggregates (IAA) and (b) cluster-cluster-aggregates (CCA) are presented. The dashed lines are least-square quadratic fits: in (a) for IAA, $S'_r = 8.24(R'_m)^2$, in (b) for CCA, $S'_r = 7.47(R'_m)^2$.

To rescale the straining force, we define

$$S'_r = \frac{S'_f}{1 + \gamma\sigma_m},$$

with σ_m defined above as the non-dimensional deviation from the average maximum radius for aggregates of the same size. This rescaled force yields a better collapse of the data, as can be seen in Figure 2.16, particularly for IAA. We found that the best rescaling value was $\gamma = -1.32$ for IAA and $\gamma = -0.92$ for CCA. In the CCA case, the resulting data appears to grow slightly faster than quadratic. Nonetheless, it is possible to fit a quadratic to the rescaled drag, and doing so yields $S_r' = 8.24R_m^2$ with coefficient of determination $\mathbf{R}^2 = 0.89$ for IAA and $S_r' = 7.47R_m^2$ with coefficient of determination $\mathbf{R}^2 = 0.63$ for CCA.

We note that the straining force, even when rescaled, exhibits a large amount of scatter compared to the torque and drag, particularly for CCA, which tend to have more elongated aggregates. Observing individual aggregates of similar size but different straining forces reveals that the straining force is particularly sensitive to the orientation of an aggregate. The scatter is thus largely due to this sensitivity, as the same aggregate oriented differently can experience a significantly different straining force.

2.6 Discussion

The results presented above all use a resolution of $\Delta x = 2$, which corresponds to using aggregates made of cubes of non-dimensional side length 2, not further refined. To assess the accuracy of results with this resolution, we considered 16 different aggregates made of 100 cubes of side length two and refined the resolution to use $\Delta x = 2, 1$, and $2/3$, thus increasing the number of cubes from 100 to 800 and 2700 while maintaining the aggregate shape. Both the drag and torque were seen to converge as the resolution was increased. The coarsest resolution, used in the section above, yielded results that were less than 2% away from the more highly resolved results for the drag and less than 5% away for the torque (we found for similar sampling that the extensional force behaved in a manner between that of the drag and torque). For comparison, the standard deviation of the drag and torque of the samples considered was approximately three times as large for all resolutions studied. The variability between aggregates of a given size thus far exceeds the error due to a coarse resolution. Further, we performed a similar study on aggregates of various sizes and found that the effects of a coarse resolution decreased as the size of the aggregate increased. The data we present is for aggregates of size ranging from 25 to 200 cubes with $\Delta x = 2$ and is, therefore, sufficiently accurate to allow a meaningful quantification of the drag, extensional force, and torque.

To put the results for aggregates obtained in section 2.5 into context, we compare them to the well-known corresponding results for a sphere (Guazzelli & Morris, 2011).

The gyration radius of a sphere of radius R_s is $R_g = \sqrt{2/5}R_s$, and thus the Stokes hydrodynamic force acting on a sphere is $\vec{F}_o = 6\pi\tilde{\mu}\vec{U}_a R_s \approx 29.8\tilde{\mu}\vec{U}_a R_g$. Also, the torque on a rotating sphere is $\vec{Q}_o = 8\pi\tilde{\mu}\vec{\Omega}R_s^3 \approx 99.35\tilde{\mu}\vec{\Omega}R_g^3$. For a sphere in an extensional flow, the exact solution of the straining force for the flow satisfying $\vec{U}_{bg} = \bar{\bar{M}} \cdot \vec{x}$ at infinity and $\vec{U}_{bg} = 0$ on the surface of the sphere is known (Guazzelli & Morris, 2011). The details of the computation of the corresponding straining force are given in the appendix. We find that for a matrix $\bar{\bar{M}}$ with unit eigenvector $\hat{v}_i$ and corresponding eigenvalue λ_i, the straining force is

$$E_i = \frac{1}{2}\int_S |\vec{f} \cdot \hat{v}_i| \, dS = 5\pi\tilde{\mu}R_s^2\lambda_i \approx 15.7\tilde{\mu}R_m^2\lambda_i,$$

where we used that the maximum radius R_m of a sphere is simply its usual radius R_s and that a sphere in an extensional flow experiences no net force.

Our results from Section 2.5, and the corresponding results for a sphere, are summarized in Table 2.1. We first note that the hydrodynamic force acting on translating aggregates is significantly less than that acting on a translating sphere of the same gyration radius. This is presumably because the aggregates are not densely filled and thus allow some flow to effectively go through them. For the same reason, the force on the more compact IAA is also greater than that on the less compact CCA. Similarly, the coefficients of the torque for both types of rotating aggregates are less than those of the corresponding rotating sphere. This is, once again, because less compact structures encounter less torque from the fluid when rotating. Further, a similar observation also holds for the straining force when in an extensional flow, where denser structures are subject to a larger straining force for an equivalent radius.

	Sphere	IAA	CCA
Force ($-\vec{F}$)	$29.8\tilde{\mu}\vec{U}_a R_g$	$21.47\tilde{\mu}\vec{U}_a R_g$	$18.04\tilde{\mu}\vec{U}_a R_g$
Rescaled Force ($-\vec{F}_r$)	N/A	$21.55(1-0.43\sigma_g)\tilde{\mu}\vec{U}_a R_g$	$18.16(1-0.64\sigma_g)\tilde{\mu}\vec{U}_a R_g$
Torque ($-\vec{Q}$)	$99.35\tilde{\mu}\vec{\Omega}R_g^3$	$44.12\tilde{\mu}\vec{\Omega}R_g^3$	$24.98\tilde{\mu}\vec{\Omega}R_g^3$
Straining Force ($\vec{E}$)	$15.7\tilde{\mu}R_m^2\lvert\lambda\rvert\hat{v}$	$7.48\tilde{\mu}R_m^2\lvert\lambda\rvert\hat{v}$	$6.64\tilde{\mu}R_m^2\lvert\lambda\rvert\hat{v}$
Rescaled Strain. For. (S_r)	N/A	$8.24(1-1.32\sigma_m)\tilde{\mu}\lvert\lambda\rvert R_m^2$	$7.47(1-0.92\sigma_m)\tilde{\mu}\lvert\lambda\rvert R_m^2$

Table 2.1: Summary of results from section 2.5 compared to corresponding results for a sphere.

We may use our results to define a hydrodynamic radius, R_h, as the radius of a sphere subject to similar forces or torque as a given aggregate. The exact hydrodynamic radius varies if we consider the force, torque, or straining force in their corresponding flows. On average, we find that the hydrodynamic radius obtained considering forces and torques was approximately $R_h \approx 1.15R_g$ for individually-added aggregates, and $R_h \approx 1.01R_g$ for cluster-cluster aggregates. These results are consistent, though with a smaller coefficient, with results found in terms of the maximum radius and based on the drag alone by Zhang and Zhang (Zhang & Zhang, 2015). It should be noted that corresponding spheres would also have a far larger volume, as volume scales like $V \sim R_g^3$ for spheres, while the volume of individually formed aggregates scales as $V \sim R_g^{2.57}$ and that formed by cluster aggregation scales as $V \sim R_g^{1.79}$.

As stated in the introduction, many models make use of the settling speeds of aggregates. We can use our computed force to obtain a settling speed for an aggregate with a given departure from the mean radius of aggregates of similar size, σ_g, and gyration radius R_g. To do so, we match the hydrodynamic force with the buoyancy force, $\vec{F_b} = \vec{g}V\Delta\rho$. Here $\Delta\rho$ is the density difference between the aggregate and the external fluid, and $V = 8L^3N$ is the aggregate volume, with L the half-width of the cubes forming the aggregates and N the number of cubes within an aggregate. Depending on the aggregate formation mechanism, the number of cubes will scale differently with the gyration radius. For IAA, we found that $N = 0.24(R'_g)^{2.56}$ and for CCA, we found that $N = 1.34(R'_g)^{1.79}$. Using equation (2.41) for IAA and equation (2.42) for CCA, we may solve for the Stokes settling speed of aggregates. We thus find, for IAA

$$\vec{U}_a = 0.19\left(\frac{\vec{g}\Delta\rho L^{0.44}R_g^{1.56}}{\tilde{\mu}}\right)\left(\frac{1}{1-0.43\sigma_g}\right), \tag{2.46}$$

and for CCA

$$\vec{U}_a = 0.58\left(\frac{\vec{g}\Delta\rho L^{1.21}R_g^{0.79}}{\tilde{\mu}}\right)\left(\frac{1}{1-0.64\sigma_g}\right). \tag{2.47}$$

For comparison, the settling speed of a sphere in terms of its gyration radius is

$$\vec{U}_a = \frac{5}{9}\left(\frac{\vec{g}\Delta\rho R_g^2}{\tilde{\mu}}\right). \tag{2.48}$$

These results are consistent with measurements that found that aggregates of fractal dimension close to three, more similar to IAA, had a settling speed of aggregates slower than predictions based on the settling speed of a corresponding sphere (Alldredge & Gotschalk, 1988).

We note that the increase of the settling speed as a function of aggregate size is slower than for solid objects, particularly for CCA, where the growth only scales as $R_g^{0.79}$. Moreover, we remark that our initial estimate of the Reynolds number of an aggregate was based on the Stokes settling speed of a sphere, which overestimates the settling speed of an aggregate. The use of the Stokes equations is therefore appropriate for aggregates with diameters even larger than 1mm, as initially argued.

Finally, we note that settling aggregates are generally subject to a non-zero torque and, equivalently, rotating aggregates are subject to a non-zero force. This is a result of the asymmetrical shape of any particular aggregate, which causes aggregates to spin as they settle, or equivalently, to settle as they spin. This induced motion has no preferred direction, and so the average over all the aggregates generated here is zero. However, we have computed the standard deviation of the drag of all aggregates subject to an angular velocity $\vec{\Omega}$ and found that it scaled roughly quadratically with the gyration radius. In general, then, one finds that a settling aggregate spins at a rate given by a fraction of the ratio of its settling speed over its gyration radius, $||\vec{\Omega}|| \sim ||\vec{U}_a||/R_g$, with the proportionality constant being approximately 0.005 for IAA and 0.013 for CCA.

2.7 Concentration dynamics simulations

The depth of the fluid or shape of aggregates is typically considered to quantify the efficiency of transferring organic carbon via settling aggregates. In the euphotic zone, which is the uppermost layer of the oceans, the majority of marine aggregates are remineralized by metabolic processes (Henson, Sanders, & Madsen, 2012). Omand *et al.* presented a model to study the sensitivity of the shape of the aggregates with its remineralization rate and density (Omand et al., 2020). Our model of the gravitational sinking aggregates can contribute to understanding the oceanic carbon cycle.

To understand this application and track the concentration dynamics of a marine aggregate, we solve the three-dimensional advection-diffusion equation, that is

$$\frac{\partial C}{\partial t} = -\vec{u} \cdot \nabla C + D_C \nabla^2 C, \tag{2.49}$$

where C represents the CO_2 concentration. Note that another type of concentration can be considered depending on one's interest. We denote the diffusivity (m^2/s) of C as D_C. We may non-dimensionalize equation (2.49) using the same parameters as shown in (2.23), in addition to the time parameter, $t' = (U_s/L)\,t$. As we non-dimensionalize equation (2.49), we find a dimensionless quantity, the Péclet number (Pe),

$$\mathrm{Pe} = \frac{U_s R_a}{D_C}. \tag{2.50}$$

It describes the ratio between the advection and diffusion time scales of the aggregate. One can also find the Schmidt number to understand the diffusion rate of the fluid. Since we consider the Stokes flow, the Schmidt number is effectively infinite.

With the Péclet number, the resulting advection-diffusion equation is

$$\frac{\partial C'}{\partial t'} = -\vec{u}' \cdot \nabla' C' + \frac{1}{\mathrm{Pe}} \nabla'^2 C'. \tag{2.51}$$

Based on the the diffusivity of CO_2 in seawater (Park & Choi, 2020) measured, we find the Péclet number,

$$\mathrm{Pe} = \frac{U_s R_a}{D_{CO_2}} \approx \frac{3.8 \times 10^{-4}(\mathrm{m/s}) \times \left(5 \times 10^{-5}\right)(\mathrm{m})}{6 \times 10^{-9}(\mathrm{m}^2/\mathrm{s})} \approx 3.2 \tag{2.52}$$

Note that this could differ for sizes of an aggregate, and we will explore various Péclet numbers for our simulations within a reasonable range.

In the following subsection, we explain the numerical methods to solve and couple the boundary integral equation with the advection-diffusion equation in time and space. We close this chapter by presenting preliminary results of the concentration dynamics in a homogeneous fluid.

2.7.1 Time integration

The main role of coupling the advection-diffusion equation is to update the concentration C in time. The velocity field of the advection term in equation (2.51) is obtained using the boundary integral equations. Note that the velocity does not depend on time. We only update C in time. Since our entire fluid velocity computation is already large and slow, we try to focus on efficiency for the concentration evaluation.

For the time integration, we initially selected the trapezoidal rule as the implicit method,

$$C_j^{n+1} = C_j^n + \frac{\Delta t}{2}\left[\boldsymbol{F}\left(C_j^{n+1}\right) + \boldsymbol{F}\left(C_j^n\right)\right], \tag{2.53}$$

and the two-stages Runge-Kutta as the explicit scheme,

$$C_j^{temp} = C_j^n + \frac{\Delta t}{2}\boldsymbol{F}\left(C_j^n\right) \tag{2.54}$$

$$C_j^{n+1} = C_j^n + \Delta t \boldsymbol{F}\left(C_j^{temp}\right), \tag{2.55}$$

where C_j^n represents the discrete concentration value C' at a numerical grid x_j and $n-$th time step. Here, the function, $\boldsymbol{F}$, represents any choice of spatial discretization method.

2.7.2 Spatial discretization

There are two spatial discretizations we considered: 1) finite differences (central differences) and 2) discrete Fourier transform (DFT). For this comparison, we consider the one-dimensional (1D) version of the advection-diffusion equation,

$$\frac{\partial C}{\partial t} = -u(x)\frac{\partial C}{\partial x} + \frac{1}{\text{Pe}}\frac{\partial^2 C}{\partial x^2}. \tag{2.56}$$

The finite differences method allows us to set various boundary conditions. We apply the central differences for both the advection and diffusion terms to obtain second-order convergence in space with finite differences. One concern is the stability of numerical methods. We, therefore, want to be careful about and keep track of the Courant-Friedrichs-Levy (CFL) condition for both the advection and diffusion terms,

$$\max(|u|)\frac{\Delta t}{\Delta x} \leq 1 \quad \text{for advection, and,} \quad \frac{1}{\text{Pe}}\frac{\Delta t}{\Delta x^2} \leq 1 \quad \text{for diffusion.} \tag{2.57}$$

On the other hand, the DFT is a well-known method to obtain spectral accuracy on a simple periodic domain with smooth data. It is a discretized version of the Fourier transform using the concept of Riemann sums in a bounded domain instead of infinite space. When we use a product of a small prime factor as the number of discretization nodes, typically, DFT is more efficient than finite differences. Thus, it is worthwhile to compare both methods before we choose one. In the one-dimensional domain $x \in (-L_x/2, L_x/2]$, with period L, we discretize the domain with N points. The stepsize, then, Δx is $\Delta x = L_x/N$. We use MATLAB built-in tools `fft` and `ifft` to compute the DFT and inverse DFT conveniently. The output of `fft` of $f(x_j)$ is $\hat{f}_k$. Once we have values in Fourier space, $\hat{f}_k$, we simply multiply by ik or $-k^2$ to obtain $\hat{f}'_k$ or $\hat{f}''_k$, respectively. One advantage of the DFT can be seen by letting N with the power of a small prime number, typically 2. This allows the floating point operations to become $\mathcal{O}(N \log N)$ instead of $\mathcal{O}(N^2)$. Additionally, if the solution is m times differentiable, the convergence rate for a spectral method is $\mathcal{O}(N^{-m})$.

Comparison between two spatial methods

Since our boundary integral method requires an infinite ambient, we approximate periodic boundary conditions by using a large domain size that does not affect the accuracy of the solutions near the aggregate. The velocity decreases toward zero on the edge of our domain, but it is not exactly zero, resulting in a jump at the boundary. We, therefore, compare the finite differences and the discrete Fourier transform methods to determine the one that best handles the jump at the boundaries. We investigate the error versus computing time by fixing a jump size with various resolutions. We ran the code for $t = 10\pi$ in the 1D domain $[0, 2\pi]$. In Figure 2.17, each start point represents the error obtained with the largest spatial discretization ($\Delta x \approx 0.1$). Note that the finest solution with $\Delta x \approx 0.003$ is used as the reference solution when computing the error.

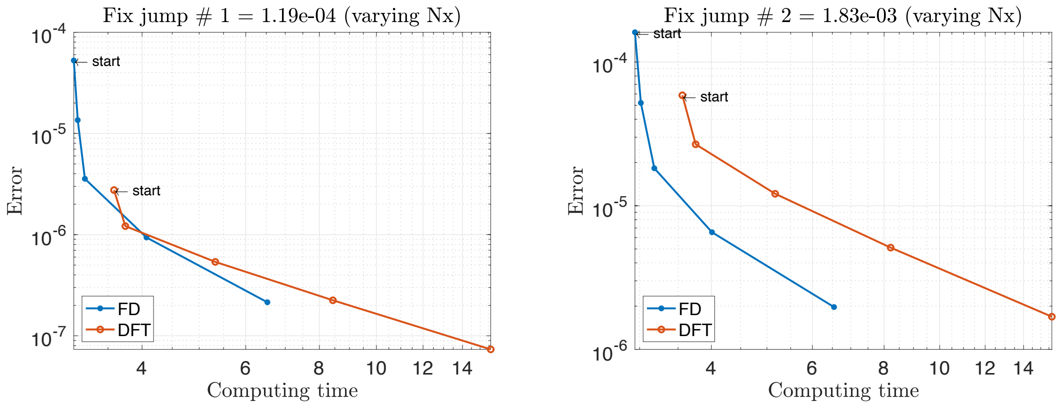

Figure 2.17: Error and computing time with jump size (left) $\mathcal{O}(10^{-4})$ and (right) $\mathcal{O}(10^{-3})$ with various resolutions ($\Delta x \approx [0.1, 0.05, 0.025, 0.01, 0.006]$)

At a glance, the error decreases, and computing time increases with higher resolutions, as we expected. In particular, the left panel of Figure 2.17 shows a smaller error due to the jump size that is about $\mathcal{O}(10^{-4})$. We note the computing time differences between the two methods. We can see this clearly in the right panel of Figure 2.17. To get a particular error size, the finite differences scheme requires less time than the DFT method. The gap between the two methods becomes larger as we compute the solution with finer resolution. This is explained by the fact that the MATLAB built-in functions, `fft`, and `ifft`, spend more time than building the sparse matrix for the finite differences to compute derivatives. It shows that finite differences are more efficient for our situation. Thus, we have decided to use the finite differences scheme for spatial discretization of the advection-diffusion equation.

2.7.3 Frames of reference

Throughout this work, we use two frames of reference: 1) lab and 2) moving frame of reference. First, for the fluid velocity computation, we use the lab frame of reference to take advantage of the zero velocity boundary condition at infinity, as shown in Figure 2.18 (left). This condition implies that the domain is large enough compared to the aggregate. We solve for the stress on the aggregate boundary by prescribing the constant velocity or the body force of the aggregate to compute the fluid velocity field.

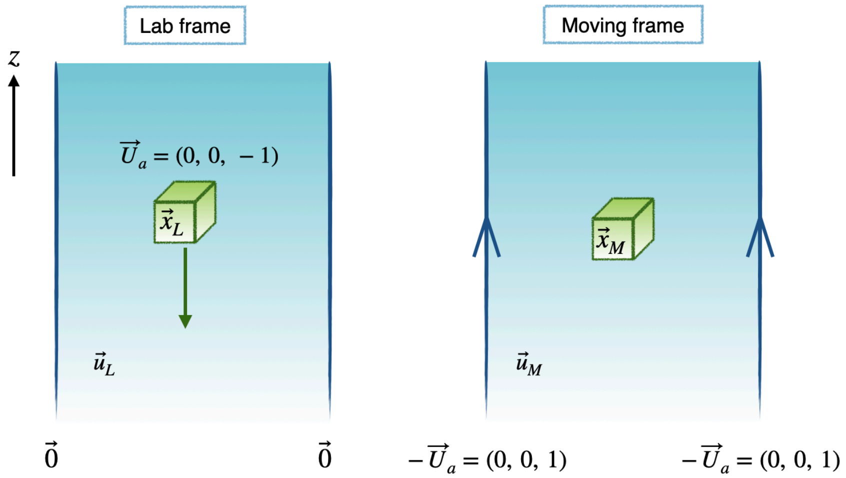

Figure 2.18: Schematics of frames of reference. (Left) lab frame and (right) moving frame of reference

On the other hand, we use the moving frame to model the concentration dynamics. In this setting, we fix the aggregate in the middle of the fluid domain and move the fluid upward to describe the settling motion, as shown in Figure 2.18 (right). This can be done by changing variable from the velocities in the lab frame; we simply add $-\vec{U}_a$ to all velocities in the lab frame of reference,

$$\vec{u}_M = \vec{u}_L - \vec{U}_a.$$

The velocity at the boundary of the fluid domain becomes the same speed but in the opposite direction, i.e., $-\vec{U}_a = (0,\ 0,\ 1)$. We also can see that now the aggregate has zero velocity in the moving frame of reference.

2.7.4 Simulations

As a sample simulation, we use ten cubes to model an aggregate with a discontinuous initial concentration, zero throughout the fluid domain, outside of the aggregate, and a higher concentration inside and on the aggregate. Specifically, we prescribe values of 1 for the inside of each cube and 0.5 for all square faces. We also place 0.25 and 0.125 for all edges and corners of cubes, respectively. This intuitive concentration setup is to reduce the risk of any stability issue due to the discontinuity at the aggregate boundary.

In addition to the initial concentration, the following conditions are set:

- Number of cubes NC = 10
- Settling velocity $\vec{U}_a$ = $(0, 0, -1)$
- Center of mass of the aggregate $\vec{x}_{cm}$ = $(-0.8,\ 0.4,\ 0)$
- Maximum radius of the aggregate $R_m \approx 5.3472$
- Domain = $[-11.50, 9.90] \times [-10.29, 11.09] \times [-21.39, 21.39]$
  (Centered at the center of mass of the aggregate.)
- Spatial step size: $Nx = Ny = 50, Nz = 100$; $\Delta x = \Delta y = \Delta z \approx 0.43$
- Péclet number Pe = 100
- Time step $\Delta t = 0.1$
- Final time $Nt = 500$

For the sample simulation, we set Pe $= 100$. This is in case it is necessary to observe a larger Péclet number that could have more numerical error. We compute the fluid velocity field once using the boundary integral method and keep it fixed while we update the concentration.

We simulated this problem using both the implicit (trapezoid) and the explicit (RK2) time integration. Under the conditions provided above, we get an advection CFL condition number of approximately 0.03 and a diffusion one of 0.08. Since the CFL numbers are less than 1, we can use the RK2 method with no stability issue. The main reason we wanted to try the explicit method is to reduce computing time if possible. However, we found that both time integration methods gave us similar results in terms of computing time.

We present snapshots of the simulation using the discontinuous initial concentration in Figure 2.19. It is a three-dimensional simulation; however, for clear visualization, we slice the domain at $x = -0.8$, which is the middle of $x-$axis. Note that we are using a moving frame of reference such that the surrounding fluid is flowing upward to represent the settling aggregate motion. After time $t \approx 30$ in Figure 2.19, we can see lower concentration is going outside of our numerical domain.

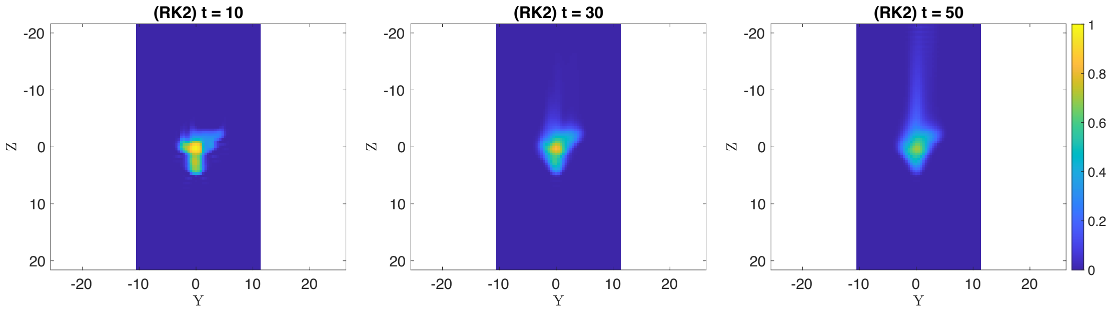

Figure 2.19: Snapshots of concentration dynamics with a discontinuous initial concentration with finite differences in space and RK2 for time.

Figure 2.20 shows the sum of the concentration of the fluid over time. The results seem to be consistent with our expectation that the mass is conserved until the flow reaches the upper boundary of our domain. The right plot in Figure 2.20 shows the concentration difference between each time and the initial one up to time $t = 20$.

2.7.5 Discussion

There are several topics we can study further with the homogeneous ambient fluid case. We may continue analyzing the preliminary results for the dissolved CO_2 model we presented. As an application of the dissolved CO_2 simulation, we consider the remineralization of marine aggregates. In particular, We can apply a method of remineralization and model dissolved CO_2 of marine aggregates to study the carbon flux profile in a homogeneous fluid. In a recent article, Omand *et al.* (Omand et al.,

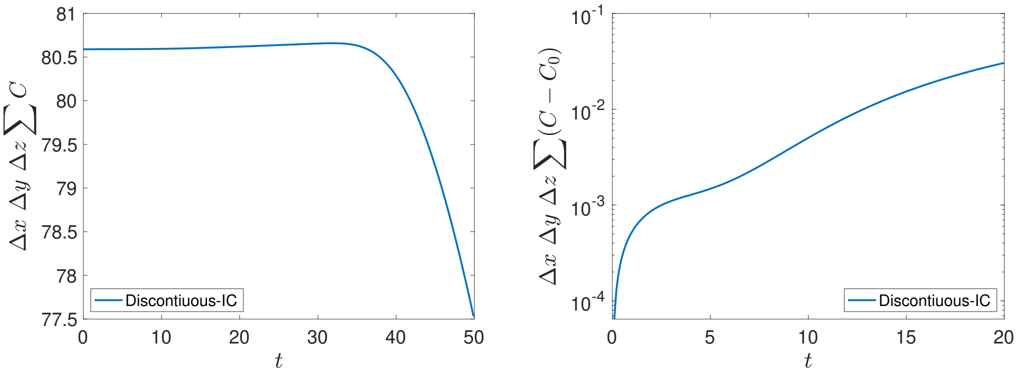

Figure 2.20: (Left) Variation of total concentration in the fluid domain in time. (Right) The error between the total concentration at each time and the initial sum of concentration.

2020) proposed a derivation of the sinking particle flux model with a sphere. Several aspects of this derivation can be improved with a model such as ours, and we can provide justifications for features that were assumed or roughly estimated. With our randomly shaped aggregate model, we expect to present more accurate dynamics and could calculate the size of a sphere with equivalent diffusive properties as a function of aggregate size and fractal dimension.

2.8 Conclusion

We have developed a novel implementation of boundary integral methods for flow around aggregates composed of cubes. In this case, we found that the single-layer approach was more accurate and therefore used it to study the flow around randomly formed aggregates. We have presented the results of the flow around individually-added and cluster-to-cluster aggregates and characterized the resulting forces. We have identified a suitable length scale to characterize the behavior of fractal aggregates in various contexts. To describe the drag or force, and torque, on an aggregate, the gyration radius, R_g, is the best choice, with respective scalings of $\vec{F}_o \sim \tilde{\mu}\vec{U}_a R_g$ and $\vec{Q}_o \sim \tilde{\mu}\vec{\Omega} R_g^3$, as should be expected in Stokes flow. An improved collapse of the drag is possible if we account for an aggregate's departure from its typical size, $\bar{R}_g$, through the factor $\sigma_g = \frac{R_g - \bar{R}_g}{\bar{R}_g}$. The nearly linear relationship between the drag and the gyration radius indicates that the choice of R_g to describe the size of an aggregate is an appropriate one while, for example, the volume-based size $L = V^{1/3}$ would not yield a linear relationship with the drag.

We have also considered the effects of extensional flow on aggregates, an aspect that has been understudied. We introduced a simple characterization of the straining force, $\vec{E}$, on a solid object. We used computations of the straining force to determine that the maximum radius, R_m, is the most appropriate length scale to predict the impact of extensional flow on an aggregate and found that $\vec{E} \sim \tilde{\mu}|\lambda|R_m^2\hat{v}$. This is particularly relevant when considering aggregate formation and break up. As in the case of the force, an improved collapse of straining force is possible using an aggregate's departure from its typical size, $\sigma_m = \frac{R_m - \bar{R}_m}{\bar{R}_m}$.

Our numerical approach can be directly applied to compute the flow around several particles. Our method can thus be used to conduct a more accurate investigation of aggregate formation. In the present study, as is the case in the vast majority of diffusion-limited aggregation studies, aggregates were formed without factoring in flow dynamics. Our numerical approach allows us to determine the response of the system dynamically when subjected to stochastic forces. Rather than assuming a constant drag and no deformation, we may instead calculate the forces acting on every particle, determine the deformation or potential break-up of the particles by matching the viscous stress with the particle's elastic stress, and determine the aggregates settling velocity as it deforms. Such an approach should provide the most accurate aggregate formation model yet, which in turn will allow for a more accurate characterization of their properties.

Another promising avenue for future work is the incorporation of stratification effects. Marine aggregates typically settle in a water column where the density increases with depth, owing to salinity and temperature variations. Since aggregates are very porous, they are sensitive to stratification (Prairie et al., 2013). Fluid entrainment and diffusive effects play a role in first stopping and then restarting the settling of the porous aggregate (Panah, Blanchette, & Khatri, 2017; Camassa et al., 2013). This process has already been modeled using spherical particles, but how diffusion and ambient stratification affect fractal-like aggregates remains unclear. By coupling the current simulations to a concentration field subject to advection-diffusion and tracking its effect on the fluid density within an aggregate, one should be able to obtain an improved approximation of the behavior of aggregates settling in a stratified ambient. Accounting for the effects of stratification on the flow itself requires the addition of a volume integral of the concentration to equation (2.11). This implies a significant increase in computational effort, but a careful implementation can be done that results in reasonable run-time. Such a derivation and implementation are the subject of the next chapter of this thesis.

Chapter 3

Settling marine aggregates in a stratified fluid

In the last few decades, several scientists have modeled the dynamics and ecological impact of marine aggregates (Jackson & Burd, 1998; Kiørboe et al., 2002). Their effects on bacterial transport (Jackson, 1989) and algal bloom (Jackson, 1990) have been described in models that use simplified descriptions of the aggregates' settling speeds. Moreover, accumulation of aggregates in thin layers where the ambient fluid is stratified has been reported (MacIntyre, Alldredge, & Gotschalk, 1995; Alldredge et al., 2002) and more recently modeled experimentally (Prairie et al., 2013), analytically (Camassa et al., 2013), and computationally (Panah, Blanchette, & Khatri, 2017). Understanding marine aggregate formation, settling speed, and persistence of these thin layers is ecologically important. Therefore, in this chapter, we discuss the dynamics of settling marine aggregates in a density-stratified fluid.

3.1 Governing Equations

In this chapter, instead of constant density ρ, as in Chapter 2, we suppose that the background fluid density varies linearly in the vertical direction,

$$\rho_{bg}(z) = \rho_0 \left(1 - \gamma z\right), \tag{3.1}$$

where ρ_0 is the fluid density where the aggregate's center of mass is located at rest initially and $\gamma > 0$ is constant. Over time, perturbations, $C(\vec{y}, t)$, occur due to the settling motion due to non-homogeneous fluid. More specifically, we define C as the concentration difference between the initial value and time t. From this, we can establish the fluid density variation over time,

$$\rho(\vec{y}, t) = \rho_{bg}(z) + \alpha\rho_0 C(\vec{y}, t) = \rho_0 \left(1 - \gamma z + \alpha C(\vec{y}, t)\right), \tag{3.2}$$

where the non-zero constant α depends on the type of solute. We provide the schematic of the perturbation effect on the top of the background fluid density in Figure 3.1. The non-constant density $\rho(\vec{y}, t)$ changes the momentum equation from (1.12) to

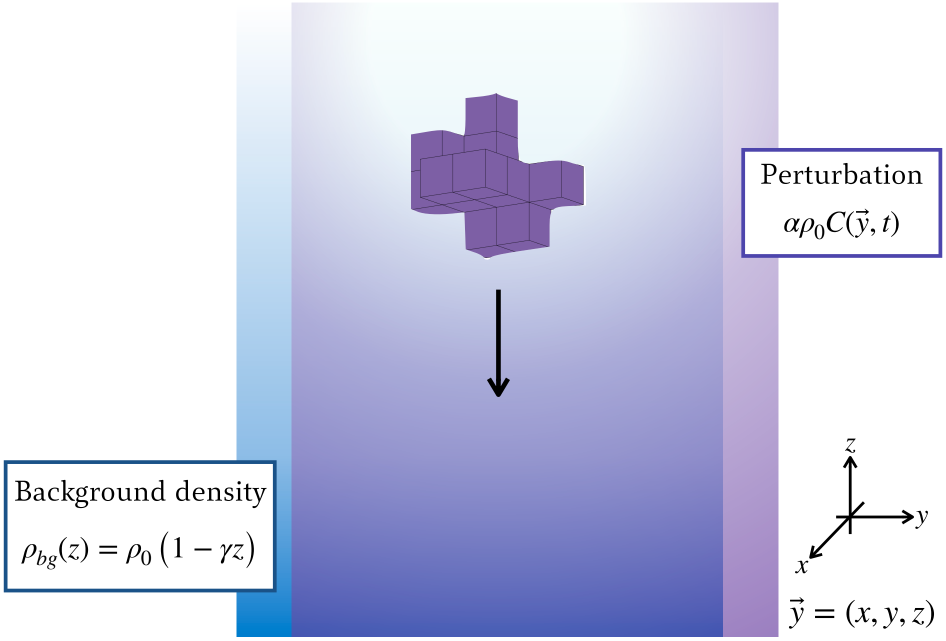

Figure 3.1: Description of fluid density stratification.

$$\tilde{\mu}\nabla^2\vec{u}(\vec{y}) - \nabla P_d(\vec{y}) \ + \ \rho_0\alpha C(\vec{y}, t)\vec{g} = 0, \tag{3.3}$$

where P_d is the dynamic pressure, defined as

$$P_d(\vec{y}) = P(\vec{y}) \ - \int \rho_{bg}(z) g \mathrm{d}z. \tag{3.4}$$

To take the density perturbation of the ambient fluid into account, we find a particular solution to the momentum equation (3.3). Once we have it, simple addition to the homogenous solution gives the entire solution due to the linearity of the system.

To derive a particular solution, we consider the singularly forced Stokes problem (Pozrikidis, 1992),

$$\tilde{\mu}\nabla^2\vec{u}(\vec{y}) - \nabla P(\vec{y}) + \vec{q}\,\delta\,(\vec{x}-\vec{y}) = 0, \tag{3.5}$$

where $\vec{q}$ is an arbitrary constant vector, $\vec{x}$ is an arbitrary point in fluid domain, and δ is the three-dimensional delta function. The problem (3.5) describes the effect coming from a singular force applied at $\vec{y}=\vec{x}$. The fundamental solution to equation (3.5) coupled with the continuity equation (1.1) are

$$\vec{u}(\vec{y}) = \frac{1}{8\pi\tilde{\mu}}\bar{\bar{G}}\,(\vec{x},\vec{y})\cdot\vec{q} \tag{3.6}$$

$$P(\vec{y}) = \frac{1}{4\pi}\frac{\vec{x}-\vec{y}}{\|\vec{x}-\vec{y}\|^3}\cdot\vec{q}, \tag{3.7}$$

where the kernel $\bar{\bar{G}}$ is the *Stokeslet*, introduced in Chapter 1, equation (1.14). This implies that the solutions (3.6) and (3.7) satisfy equation (3.5) as

$$\tilde{\mu}\nabla^2\left(\frac{1}{8\pi\tilde{\mu}}\bar{\bar{G}}\,(\vec{x},\vec{y})\cdot\vec{q}\right) - \nabla\left(\frac{1}{4\pi}\frac{\vec{x}-\vec{y}}{\|\vec{x}-\vec{y}\|^3}\cdot\vec{q}\right) + \vec{q}\,\delta\,(\vec{x}-\vec{y}) = 0. \tag{3.8}$$

When we multiply by $C(\vec{x},t)$ on both sides and integrate the entire equation over the domain, $V(\vec{x})$, we get

$$\int_V \left[\tilde{\mu}\nabla^2\left(\frac{\bar{\bar{G}}\,(\vec{x},\vec{y})\cdot\vec{q}}{8\pi\tilde{\mu}}\right)C(\vec{x},t) - \nabla\left(\frac{(\vec{x}-\vec{y})\cdot\vec{q}}{4\pi\|\vec{x}-\vec{y}\|^3}\right)C(\vec{x},t) + \vec{q}\,\delta\,(\vec{x}-\vec{y})\,C(\vec{x},t)\right]\mathrm{d}V(\vec{x}) = 0. \tag{3.9}$$

Note that the operator ∇ is linear and describes derivatives in $\vec{y}$. Additionally, since the volume V stays the same, we are able to switch the order with the integral operator as follows,

$$\tilde{\mu}\nabla^2\int_V\left(\frac{\bar{\bar{G}}\,(\vec{x},\vec{y})\cdot\vec{q}}{8\pi\tilde{\mu}}\right)C(\vec{x},t)\,\mathrm{d}V(\vec{x}) - \nabla\int_V\left(\frac{C(\vec{x},t)(\vec{x}-\vec{y})\cdot\vec{q}}{4\pi\|\vec{x}-\vec{y}\|^3}\right)\mathrm{d}V(\vec{x}) + \vec{q}C(\vec{x},t) = 0. \tag{3.10}$$

By choosing $\vec{q}=\rho_0\alpha\vec{g}$, we can find a particular solution to our modified Stokes momentum equation, (3.3),

$$\vec{u}(\vec{y}) = \frac{\rho_0\alpha}{8\pi\tilde{\mu}}\int_V \bar{\bar{G}}\,(\vec{x},\vec{y})\cdot C(\vec{x},t)\vec{g}\,\mathrm{d}V(\vec{x}). \tag{3.11}$$

$$P(\vec{y}) = \frac{\rho_0\alpha}{4\pi}\int_V \frac{\vec{x}-\vec{y}}{\|\vec{x}-\vec{y}\|^3}\cdot C(\vec{x},t)\vec{g}\,\mathrm{d}V(\vec{x}). \tag{3.12}$$

The entire velocity solution, thus, becomes

$$\vec{u}\,(\vec{y},t) = -\frac{1}{8\pi\tilde{\mu}}\int_S \vec{f}(\vec{x})\cdot\bar{\bar{G}}\,(\vec{x},\vec{y})\,\mathrm{d}S(\vec{x}) + \frac{\rho_0\alpha}{8\pi\tilde{\mu}}\int_V C\,(\vec{x},t)\,\vec{g}\cdot\bar{\bar{G}}\,(\vec{x},\vec{y})\,\mathrm{d}V(\vec{x}). \tag{3.13}$$

As we see, the velocity at a point $\vec{u}(\vec{y},t)$ is now dependent on space and time compared to the homogeneous fluid case. We can update the velocity field in time by coupling the solution (3.13) with the advection-diffusion equation (2.51) to model the solute perturbation, C.

3.1.1 Force balance

Since the velocity of the aggregate is no longer constant in time, we now need to solve it. Specifically, we now need to solve for the translational and angular velocity, $\vec{U}_a$ and $\vec{\Omega}$, respectively, by prescribing the total body force and total torque from the fluid on the aggregate. To close the system of equations, we prescribe the total drag force, $\vec{F}_o$, and total torque, $\vec{Q}_o$.

First, we know that the total drag is the sum of the stress, $\vec{f}$,

$$\vec{F}_o = \int_S \vec{f}(\vec{x})\,\mathrm{d}S = -\int_S \left[-\left(P - \int \rho_{bg}(z)g\,\mathrm{d}z\right)\bar{\bar{I}} + \tilde{\mu}\left(\nabla\vec{u} + (\nabla\vec{u})^T\right)\right]\cdot\hat{n}\,\mathrm{d}S(\vec{y}). \tag{3.14}$$

To impose the total drag (3.14), we observe the right-hand side of equation (3.14) includes the buoyancy force, $\vec{F}_b$. As we work in the Stokes regime, the net force on the aggregate must be zero, so we have

$$\vec{F}_o(t) + \vec{F}_g(t) + \vec{F}_b = \vec{0}, \tag{3.15}$$

where the gravity force acting on the aggregate, $\vec{F}_g$, can be expressed as

$$\vec{F}_g = \rho_a V_a \vec{g}, \tag{3.16}$$

with aggregate density ρ_a and volume V_a. To calculate the aggregate density, ρ_a, we consider aggregate porosity, ϕ, that is $0 \le \phi \le 1$. We then define the density of an aggregate as

$$\rho_a = \phi\rho_f + (1-\phi)\rho_s, \tag{3.17}$$

where ρ_f and ρ_s are the density of the fluid and solid portion of the aggregate, respectively. To obtain the fluid portion of the aggregate density, we take an average of the fluid density where the aggregate is located,

$$\rho_f(t) = \frac{1}{V_a}\int_{V_a}\rho(\vec{x},t)\,\mathrm{d}V(\vec{x}) \tag{3.18}$$

We here consider the solid part of the aggregate density as $\rho_s \approx 1400\text{kg/m}^3$. We also set the porosity to $\phi = 0.95$. Meanwhile, we find the buoyancy force, $\vec{F}_b$, from equation (3.14),

$$\vec{F}_b = -\int_S \left(\int \rho_{bg}(z) g \, \mathrm{d}z \right) \bar{\bar{I}} \cdot \hat{n} \, \mathrm{d}S(\vec{y}). \tag{3.19}$$

For the total torque, we use the form (2.29), and set the value to zero,

$$\vec{Q}_o = \int_S \vec{f} \times (\vec{x} - \vec{x}_{cm}) \, \mathrm{d}S = \vec{0}. \tag{3.20}$$

Note that this does not imply that the aggregate is not rotating.

3.1.2 Perturbation variation

As the aggregate settles, the concentration, and therefore the fluid density, changes

$$\frac{\partial \rho(\vec{y}, t)}{\partial t} + \vec{u}(\vec{y}) \cdot \nabla \rho(\vec{y}, t) = D \nabla^2 \rho(\vec{y}, t), \tag{3.21}$$

where D is the diffusion coefficient. By applying the relationship between fluid density ρ and the concentration perturbation C from equation (3.2), we can rewrite the equation (3.21) in terms of C,

$$\frac{\partial C(\vec{y}, t)}{\partial t} + \vec{u}(\vec{y}) \cdot \nabla C(\vec{y}, t) = D \nabla^2 C(\vec{y}, t) + \frac{\gamma}{\alpha} \vec{u}(\vec{y}) \cdot \hat{k}. \tag{3.22}$$

Note that the advection-diffusion equation for C contains an additional source term that depends on the vertical component of the fluid velocity.

3.2 Dimensional analysis

To facilitate further analysis, we non-dimensionalize our new equations. We mainly use the same parameters we introduced in section 2.3, equations (2.23), in addition to the following dimensionless parameters:

$$C = C_{max} C' \qquad \rho = \frac{\tilde{\mu}}{U_s R_a} \rho', \tag{3.23}$$

In this chapter, the Stokes settling speed U_s, defined in equation (1.6), becomes

$$U_s = \frac{g R_a^2}{\tilde{\mu}} (\rho_s - \rho_0)(1 - \phi),$$

since we consider the porosity of an aggregate as (3.17). For the scale of the perturbation, C, we introduce the maximum density difference of the background density profile in the fluid domain at the initial time, i.e.,

$$C_{max} = \frac{1}{\alpha\rho_0}\left|\max_{\vec{x}\in V}\left(\rho_{bg}(z)\right) \; - \min_{\vec{x}\in V}\left(\rho_{bg}(z)\right)\right|. \tag{3.24}$$

We first derive the dimensionless modified Stokes momentum equation, using primes to indicate dimensionless variables,

$$\nabla'^2\vec{u}'(\vec{y}) = \nabla P_d{}'(\vec{y}) \; - \; \frac{\alpha\rho_0 C_{max}}{(\rho_s-\rho_0)(1-\phi)} C'\left(\vec{y},t\right)\hat{k}, \tag{3.25}$$

which is then solved for the velocity,

$$\begin{aligned}\vec{u}'(\vec{y}) = &-\frac{1}{8\pi}\int_{S'}\vec{f}'(\vec{x})\cdot\bar{\bar{G}}'\left(\vec{x},\vec{y}\right)\mathrm{d}S'(\vec{x}) \\ &-\frac{\alpha C_{max}}{8\pi}\frac{\rho_0}{(\rho_s-\rho_0)(1-\phi)}\int_{V'} C'\left(\vec{x},t\right)\hat{k}\cdot\bar{\bar{G}}'(\vec{x},\vec{y})\,\mathrm{d}V'(\vec{x})\end{aligned} \tag{3.26}$$

where S' is the aggregate surface. Moreover, the force balance equation (3.15) becomes

$$\vec{F'}_o(t) = \frac{1}{\tilde{\mu}U_sR_a}\left(-\rho_a V_a g\hat{k} + \int_S\left(\int\rho_{bg}(z)g\,\mathrm{d}z\right)\bar{\bar{I}}\cdot\hat{n}\,\mathrm{d}S(\vec{x})\right). \tag{3.27}$$

Lastly, the advection-diffusion equation becomes,

$$\frac{\partial C'(\vec{x},t)}{\partial t'} + \vec{u}'(\vec{x})\cdot\nabla' C'(\vec{x},t) = \frac{1}{\mathrm{Pe}}\nabla'^2 C'(\vec{x},t) + \frac{\gamma R_a}{\alpha C_{max}}\vec{u}'\cdot\hat{k}, \tag{3.28}$$

using the velocity field from equation (3.26), for the advection term. Note that we discussed the Péclet number with CO_2 diffusivity in Chapter 2.7 while introducing its definition in equation (2.50). In addition, using the thermal diffusivity of the ocean, D_{heat} (Nayar et al., 2016; Sharqawy, Lienhard, & Zubair, 2010): we get a Péclet number of

$$\mathrm{Pe}_{heat} = \frac{U_sR_a}{D_{heat}} \approx \frac{3.8\times10^{-4}(\mathrm{m/s})\times\left(5\times10^{-5}\right)(\mathrm{m})}{1.5\times10^{-7}(\mathrm{m^2/s})} \approx 10^{-2}, \tag{3.29}$$

and the diffusion effect due to salinity (Wollast & Garrels, 1971),

$$\mathrm{Pe}_{salt} = \frac{U_sR_a}{D_{salt}} \approx \frac{3.8\times10^{-4}(\mathrm{m/s})\times\left(5\times10^{-5}\right)(\mathrm{m})}{2\times10^{-9}(\mathrm{m^2/s})} \approx 9.5. \tag{3.30}$$

For the rest of this chapter, we drop the prime for simplicity and use only dimensionless forms.

3.3 Numerical methods

In this section, we first consider drag computation on an aggregate. We derive the simplest form to implement. We then revisit the velocity field calculation in a homogeneous fluid. We briefly introduce the linear system to solve for the aggregate's stress and velocity. Lastly, we present the method to compute the velocity field in a fluid with density stratification, involving a volume integral of the perturbation $C(\vec{x}, t)$. Due to the high computational cost, we use the fast multipole method (FMM). We briefly introduce the FMM and its framework for the Stokes kernel.

3.3.1 Aggregate force balance

We first recall the force balance equation (3.15), introduced in section 3.1.1. To obtain the total drag, there are two types of forces we consider: 1) aggregate body force, $\vec{F}_g$, and 2) fluid buoyancy force, $\vec{F}_b$. The aggregate density, ρ_a, of the fluid portion changes over time, which affects its (dimensionless) gravitational body force,

$$\vec{F}_g = -\frac{1}{\tilde{\mu} U_s R_a}\left(\rho_a V_a g \hat{k}\right). \tag{3.31}$$

We also need to track the buoyancy, depending on the aggregate's vertical position,

$$\vec{F}_b = \frac{1}{\tilde{\mu} U_s R_a}\left(\int_S \left(\int \rho_{bg}(z) g \, \mathrm{d}z\right) \bar{\bar{I}} \cdot \hat{n} \, \mathrm{d}S(\vec{x})\right), \tag{3.32}$$

since the surrounding fluid density changes while the aggregate settles. For further simplicity, we find an antiderivative of the background density,

$$\mathcal{P}_{bg}(z) = \int \rho_{bg}(z) g \, \mathrm{d}z = \rho_0 \left(z - \frac{1}{2}\gamma z^2\right) g, \tag{3.33}$$

by choosing the lower bound of the integral as zero without loss of generality. In practice, we can easily evaluate the gravitational force (3.31). While settling, we compute the fluid density where the aggregate is located. Once we know which grid points are inside the aggregate, simply adding the densities at those points gives us the fluid density portion of the aggregate, which eventually plays a role in updating ρ_a.

Next, we investigate the buoyancy force (3.32) with a single cube case for simplicity. We can extend this case to multiple cubes in the same manner by addition. We consider the discretized version of integral (3.32),

$$\vec{F}_b \approx \frac{1}{\tilde{\mu} U_s R_a} \sum_{i=1}^{N_f} R_a^3 \int_{S^i} \mathcal{P}_{bg}(z) \bar{\bar{I}} \cdot \hat{n}_i \, \mathrm{d}S^i(\vec{x}), \tag{3.34}$$

where i represents the index of square faces (not power), and N_f is the number of square faces: $N_f = 6$ for one cube case. Depending on the orientation of each square face, or the axis of S^n, is different. For example, let S^1 be the first square with the normal $\hat{n}_1 = (1, 0, 0)$, and surface parametrized with y and z between -1 and 1,

$$\mathcal{L}_1 \equiv R_a^3 \int_{S^1} \mathcal{P}_{bg}(z)\bar{\bar{I}} \cdot \hat{n}_1 \, \mathrm{d}S^1(\vec{x}) = R_a^3 \int_{-1}^{1}\int_{-1}^{1} \mathcal{P}_{bg}(z)\bar{\bar{I}} \cdot \hat{n}_1 \, \mathrm{d}y\mathrm{d}z. \tag{3.35}$$

See Figure 3.2 for notation. Since the background density ρ_{bg} is a function of z, we can intuitively see that the value (3.35) and the one with the normal $\hat{n}_6 = -\hat{n}_1 = (-1, 0, 0)$ has the same magnitude but in the opposite direction, and thus, we have $\mathcal{L}_6 = -\mathcal{L}_1$. This implies the following,

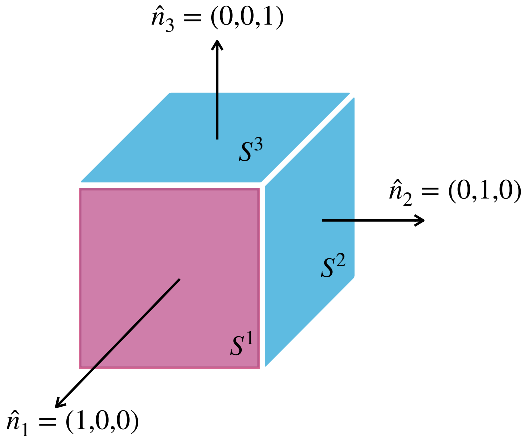

Figure 3.2: Example cube to describe the buoyancy force computation. The pink area is the S^1 integral domain.

$$\sum_{i=1,2,5,6} R_a^3 \int_{S^i} \mathcal{P}_{bg}(z)\bar{\bar{I}} \cdot \hat{n}_i \, \mathrm{d}S^i(\vec{x}) = 0 \tag{3.36}$$

for the one cube case of discretized buoyancy equation (3.34).

The integrals on S^3 and S^4 are slightly different since the square faces are perpendicular to the $z-$axis. On the face S^3, which has normal $\hat{n}_3 = (0, 0, 1)$, we get

$$R_a^3 \rho_0 \int_{-1}^{1}\int_{-1}^{1} \left(z - \frac{\gamma}{2} z^2\right) g\bar{\bar{I}} \cdot \hat{n}_3 \, \mathrm{d}x\mathrm{d}y = 4R_a^3 \rho_0 \left(z_T - \frac{\gamma}{2} {z_T}^2\right) g\hat{n}_3, \tag{3.37}$$

where z_T is the constant $z-$level value on the face S^3. The integral value on the face S^4 would be the same as (3.37), having $\hat{n}_4 = (0, 0, -1)$ instead of $\hat{n}_3$. We then can have a more explicit expression for the discretized buoyancy equation (3.34),

$$\begin{aligned}&\sum_{i=1}^{6} R_a^3 \int_{S^i} \mathcal{P}_{bg}(z) g \bar{\bar{I}} \cdot \hat{n}_i \, \mathrm{d}S^i(\vec{x}) \\ &= 4R_a^3\rho_0 \left(z_T - \frac{\gamma}{2}{z_T}^2\right) g\hat{n}_3 + 4R_a^3\rho_0 \left(z_B - \frac{\gamma}{2}{z_B}^2\right) g\hat{n}_4, \end{aligned} \tag{3.38}$$

where z_B is the constant $z-$value on the surface S^4 (bottom face). By substituting the normals $\hat{n}_3$ and $\hat{n}_4$, we can simplify the right-hand side of equation (3.38), knowing that $z_T - z_B = 2$, equation (3.38) becomes

$$\sum_{i=1}^{6} R_a^3 \int_{S^i} \mathcal{P}_{bg}(z) g \bar{\bar{I}} \cdot \hat{n}_i \, \mathrm{d}S^i(\vec{x}) = 8R_a^3\rho_0 \left(1 - \gamma z_{c_n}\right) g, \tag{3.39}$$

where we define the $z-$component of the center of the $n-$th cube forming an aggregate, z_{c_n} ($n = 1, 2, \cdots, NC$). We thus have shown that the only information we need to keep track of is the location of the center of each cube that forms an aggregate.

3.3.2 Linear system for velocity and stress on aggregates

As mentioned in section 3.1.1, we do not prescribe the settling velocity of an aggregate, and it becomes one of our unknowns. We thus need to solve for 1) translational velocity ($\vec{U}_a$), 2) rotational velocity ($\vec{\Omega}$), and 3) stress vector ($\vec{f}_k$) on each square face k. To do so, for any point $\vec{y}$ on the surface of the aggregate, we consider the surface velocity equations (3.26) with the solid body motion, (2.3),

$$\begin{aligned}&\vec{U}_a + \vec{\Omega} \times (\vec{y} - \vec{x}_{cm}) + \frac{1}{8\pi} \int_S \vec{f}(\vec{x}) \cdot \bar{\bar{G}}(\vec{x}, \vec{y}) \, \mathrm{d}S(\vec{x}) \\ &= -\frac{\alpha C_{max}}{8\pi} \frac{\rho_0}{(\rho_s - \rho_0)(1-\phi)} \int_V C\left(\vec{x}, t\right) \hat{k} \cdot \bar{\bar{G}}(\vec{x}, \vec{y}) \, \mathrm{d}V(\vec{x}), \end{aligned} \tag{3.40}$$

where the volume integral value on the right-hand side is known. To set up the linear system accordingly, We discretize the boundary integral as described in equation (2.35), choosing $\vec{f}_k$ for $\vec{q}_k$, and $\bar{\bar{G}}$ for $\bar{\bar{J}}$,

$$\vec{I}(\vec{x}_{sq,i}) = \sum_{k=1}^{N_f} \vec{f}_k \int_{S_k} \bar{\bar{G}}(\vec{x}, \vec{x}_{sq,i}) \, \mathrm{d}S(\vec{x}) = \sum_{k=1}^{N_f} \vec{f}_k \, \bar{\bar{\Pi}}_{i,k} \approx \int_S \vec{f}(\vec{x}) \cdot \bar{\bar{G}}(\vec{x}, \vec{x}_{sq,i}) \, \mathrm{d}S(\vec{x}), \tag{3.41}$$

where $\vec{x}_{sq,i}$ is the center of each square on the surface for $i = 1, 2, \cdots, N_f$. With equations (3.14), (3.20), the exact linear system of the equations we implement is as follows.

$$\left[\begin{array}{c|c|c}
\begin{bmatrix}\bar{\bar{\Pi}}_{1,1} & \bar{\bar{\Pi}}_{1,2} & \cdots & \bar{\bar{\Pi}}_{1,N_f}\\ \bar{\bar{\Pi}}_{2,1} & \bar{\bar{\Pi}}_{2,2} & \cdots & \bar{\bar{\Pi}}_{2,N_f}\\ \vdots & \vdots & \ddots & \vdots \\ \bar{\bar{\Pi}}_{N_f,1} & \bar{\bar{\Pi}}_{N_f,2} & \cdots & \bar{\bar{\Pi}}_{N_f,N_f}\end{bmatrix} & \begin{bmatrix}\bar{\bar{I}}\\ \vdots \\ \bar{\bar{I}}\end{bmatrix} & -\begin{bmatrix}[\vec{x}_{sq,1}-\vec{x}_{cm}]_\times \\ \vdots \\ [\vec{x}_{sq,N_f}-\vec{x}_{cm}]_\times\end{bmatrix} \\ \hline
4\begin{bmatrix}\bar{\bar{I}} & \cdots & \bar{\bar{I}}\end{bmatrix} & \bar{\bar{0}} & \bar{\bar{0}} \\ \hline
-4\begin{bmatrix}[\vec{x}_{sq,1}-\vec{x}_{cm}]_\times & \cdots & [\vec{x}_{sq,N_f}-\vec{x}_{cm}]_\times\end{bmatrix} & \bar{\bar{0}} & \bar{\bar{0}}
\end{array}\right]
\left[\begin{array}{c}\vec{f}_1\\ \vdots\\ \vec{f}_{N_f}\\ \hline \vec{U}_a \\ \hline \vec{\Omega}\end{array}\right] = \left[\begin{array}{c}\vec{\mathcal{F}}^1\\ \vdots \\ \vec{\mathcal{F}}^{N_f}\\ \hline \vec{F}_o\\ \hline \vec{Q}_o\end{array}\right]. \tag{3.42}$$

Since we consider three-dimensional space, the size of the identity matrix $\bar{\bar{I}}$ is (3×3). The matrix $[\vec{y}]_\times$ represents the cross product operator defined by,

$$[\vec{y}]_\times = \begin{bmatrix} 0 & -y_3 & y_2 \\ y_3 & 0 & -y_1 \\ -y_2 & y_1 & 0 \end{bmatrix}, \tag{3.43}$$

where $\vec{y} = (y_1, y_2, y_3)$. We use this operator for the rotation term,

$$[\vec{x} - \vec{x}_{cm}]_\times \vec{\Omega} = (\vec{x} - \vec{x}_{cm}) \times \vec{\Omega} = -\vec{\Omega} \times (\vec{x} - \vec{x}_{cm}),$$

in the total torque equation. In addition, the top part of the right-hand side of the equation (3.40) is the discretization of the volume integral,

$$\vec{\mathcal{F}}(\vec{x}_{sq,i}) = -\frac{\alpha C_{max}}{8\pi} \frac{\rho_0}{(\rho_s - \rho_0)(1-\phi)} \sum_{j=1}^{Ns} C\left(\vec{x}_{sq,i}, t\right) \hat{k} \cdot \bar{\bar{G}}\left(\vec{x}_{sq,i}, \vec{x}_j\right), \tag{3.44}$$

where N_s is the total number of grid or source points in the fluid domain. We discuss more details of the volume integral computation in the next section. One can find factor 4 multiplied by the second and third blocks on the right-hand side of the system (3.42). Since we set the side length of a cube as 2, factor 4 represents the area of a square face, which is the integral domain of the total force and torque equations. Note that the linear system 3.42 gives us infinitely many solutions. To select a unique solution, we use the method of least squares.

Once we solve the linear system and obtain the unknowns, we use equation (3.26) to calculate the velocity field at all points in the fluid domain. We want to point out that the fluid velocity computation, especially including the volume integral (3.44), is a very numerically expensive calculation. To accelerate it, we apply the fast multipole method (FMM) to our simulations. In the following section, we explain how we use the FMM.

3.3.3 Fast Multipole Method (FMM)

Knowing that we simulate our problem in a three-dimensional fluid domain, it is necessary to implement an efficient and fast method for each part of the code. At the same time, we want to keep the stability and desired accuracy. The FMM is a numerical scheme for rapid computation of N-body problems governed by a Green's function using a multipole expansion. It was first introduced by Greengard and Rokhlin (L. Greengard & Rokhlin, 1987). Since then, the researchers at Flatiron Institute - Simons Foundation, including the original authors of the FMM, have developed the methods and shared the source code (Cheng, Greengard, & Rokhlin, 1999; L. Greengard & Rokhlin, 1997; L. F. Greengard & Huang, 2002). We choose to use their library, called FMM3D. It provides the Fortran code with MATLAB wrapper for the $N-$body interactions governed by Laplace and Helmholtz equations in three dimensions. For our problem, we can modify the Laplace kernel, as shown in (Tornberg & Greengard, 2008), to compute the integrals of the Stokeslet (1.14). The definition of the Laplace FMM in the FMM3D library is the following:

Definition 3.3.1. (*Laplace FMM*) Let $c^n \in \mathbb{R}$ denote a collection of charge strengths and $\vec{v}^n \in \mathbb{R}^3$ denote a collection of dipole strengths for $n = 1, 2, \cdots, N$. The Laplace FMM computes the potential $u(\vec{y}^m) \in \mathbb{R}^3$ given by

$$u(\vec{y}^m) = \sum_{n=1}^{N} \left[\frac{c^n}{\|\vec{x}^n - \vec{y}^m\|} - \vec{v}^n \cdot \nabla_{\vec{y}} \frac{1}{\|\vec{x}^n - \vec{y}^m\|} \right], \tag{3.45}$$

at the *source* ($\vec{x}^n$) and *target* locations ($\vec{y}^m$). When $\vec{y}^m = \vec{x}^n$, the term corresponding to $\vec{x}^n$ is dropped from the sum.

Note that we use the letters m and n to index the targets and sources, respectively. For our problem, the points where we want to obtain velocity would be the targets; all points in the integral domain are sources. In addition to the target and source points, we can input the constant c^n and vector $\vec{v}^n$. One needs to be careful with these terms; both values could depend on the sources but are independent of the targets.

Volume integral of the Stokeslet

We first investigate how to incorporate the volume integral (3.44) (without the prefactor) in the form of (3.45). For a fixed j, we can rewrite the equation using the index notation ($i, j = 1, 2, 3$),

$$\tilde{V}(y_j^m) \equiv d \sum_{n=1}^{Ns} \sum_{i=1}^{3} C(x_i^n, t) k_i G_{ij}(x_i^n, y_j^m), \tag{3.46}$$

where $\vec{y}^m = (y_1^m,\ y_2^m,\ y_3^m)$ is the target point, $\vec{x}^n = (x_1^n,\ x_2^n,\ x_3^n)$ are the source or grid points in the fluid domain V, and d is a constant from a quadrature method. The Stokeslet can be expressed in terms of the Laplace kernel, $\Phi(\vec{x}, \vec{y}) = 1/\|\vec{x} - \vec{y}\|$ as,

$$G_{ij}(\vec{x}^n, \vec{y}^m) = \delta_{ij} \Phi\left(x_i^n - y_j^m\right) - \left(x_i^n - y_j^m\right) \frac{\partial}{\partial x_j} \Phi\left(x_i^n - y_j^m\right) \tag{3.47}$$

By substituting the Stokeslet (3.47) into the discretized volume integral (3.46), we then get

$$\tilde{V}_j(\vec{y}^m) = \sum_{n=1}^{Ns} d \sum_{i=1}^{3} C(x_i^n, t) k_i \left(\frac{\delta_{ij}}{\|\vec{x}^n - \vec{y}^m\|} - \left(x_i^n - y_j^m\right) \frac{\partial}{\partial x_j} \frac{1}{\|\vec{x}^n - \vec{y}^m\|} \right) \tag{3.48}$$

Knowing that the vector $\hat{k} = (0,\ 0,\ 1)$, only the terms where $i = 3$ survive. We thus reach the simplified sum,

$$\tilde{V}_j(\vec{y}^m) = \sum_{\substack{n=1 \\ n \neq m}}^{Ns} d\, C(x_3^n, t) \left(\frac{\delta_{3j}}{\|\vec{x}^n - \vec{y}^m\|} - x_3^n \frac{\partial}{\partial x_j} \frac{1}{\|\vec{x}^n - \vec{y}^m\|} \right) \tag{3.49}$$

$$+ y_j^m \sum_{\substack{n=1 \\ n \neq m}}^{Ns} d\, C(x_3^n, t) \frac{\partial}{\partial x_j} \frac{1}{\|x_3^n - y_j^m\|} + \mathbb{V}_p. \tag{3.50}$$

We take the singularity out of the sums since the FMM3D only evaluates an integral for points $\vec{y}^m \neq \vec{x}^n \in V$. At a singularity, i.e., $\vec{y}^m = \vec{x}^n$, we use MATLAB built-in function, `integral3`, to integrate numerically by defining a small cube $\mathbb{V}_p$ around the singularity point,

$$\mathbb{V}_p(\vec{y}) = \int_{V_p} C(\vec{x}, t) \hat{k} \cdot \bar{\bar{G}}\,(\vec{x}, \vec{y})\, \mathrm{d}V(\vec{x}). \tag{3.51}$$

We then compute $\tilde{V}$ as in equation (3.46). We also split the last (gradient) term having $\left(x_i^n - y_j^m\right)$ in equation (3.48), and write it as two summations in equation (3.50) to point out that these two points, x_i^n and y_j^m, represent different arguments. The point x_i^n

represents all points in the volume integral domain V, i.e., *source* and y_j^m is a particular point, or *target*, in which we evaluate the velocity. This is important to acknowledge since the FMM3D code treats these source and target points separately, and this is the key to accelerating the computation. The main advantage of using FMM is that we call this FMM code only once for multiple targets with N_s number of source points.

Moreover, since our summation has a vector form, while the FMM3D package returns a scalar value, we need to run this FMM3D package three times at least for each part, (3.49) and (3.50). For more details, we break down the equations to determine what are c^n and $\vec{v}^n$ would be in (3.45). First, we consider the first term in summation (3.49),

$$\sum_{\substack{n=1\\n\neq m}}^{Ns} d\, C(x_3^n,t)\frac{\delta_{3j}}{\|x_3^n - y_j^m\|} = \left(0,\ 0, d\sum_{\substack{n=1\\n\neq m}}^{Ns} \frac{C(x_3^n,t)}{\|x_i^n - y_j^m\|}\right) \tag{3.52}$$

Since $C(x_3^n,t) \in \mathbb{R}$ for each n and a fixed time t, we simply choose $c^n = C(x_3^n,t)$. The second term in the sum (3.49) can be computed by letting $\vec{v}^n$ in equation (3.45) be the product of the standard basis vector, $\hat{e}_j$, and the constant $x_3^n\ C(x_3^n,t)$, that is

$$\sum_{\substack{n=1\\n\neq m}}^{Ns} d\, C(x_3^n,t)\left(x_3^n\frac{\partial}{\partial x_j}\frac{1}{\|\vec{x}^n - \vec{y}^m\|}\right) = d\sum_{\substack{n=1\\n\neq m}}^{Ns} x_3^n\ C(x_3^n,t)\ \nabla_{\vec{y}}\frac{1}{\|\vec{x}^n - \vec{y}^m\|}. \tag{3.53}$$

We simply repeat the FMM3D for each component.

As we mentioned, the second summation (3.50) is slightly different since the target point is multiplied by the gradient term that can be only related to the sources. One of the critical rules in the FMM is separating the target and source terms to compute integrals rapidly. Thus, the computation of this sum requires another three uses of the FMM package and a dot product with the target point vector. We compute the sum in the same manner as in (3.53)

$$y_j^m\sum_{\substack{n=1\\n\neq m}}^{Ns} d\, C(x_3^n,t)\frac{\partial}{\partial x_j}\frac{1}{\|\vec{x}^n - \vec{y}^m\|} = dy_j^m\sum_{\substack{n=1\\n\neq m}}^{Ns} C(x_3^n,t)\ \nabla_{\vec{y}}\frac{1}{\|\vec{x}^n - \vec{y}^m\|} \tag{3.54}$$

as we have shown in the previous summation term with the gradient.

Surface integral of the Stokeslet

To obtain the fluid velocity, we use equation (3.26) for all $\vec{y} \in V$. In this computation, the evaluation of

$$u_H(\vec{y}) = \int_S \vec{f}(\vec{x})\cdot \bar{\bar{G}}\,(\vec{x},\vec{y})\ \mathrm{d}S(\vec{x}), \tag{3.55}$$

is quite expensive, as is that of the volume integral. We measured CPU time while varying the total number of fluid grid points. In Figure 3.3, each line represents CPU time to compute, in seconds: 1) volume integral on the aggregate surface S, 2) volume integral in the fluid domain V, 3) solving the linear system (3.42), 4) solving the advection-diffusion equation to update the perturbation, 5) velocity evaluation in the fluid domain, and 6) sum of all above (1 - 5). The main takeaway in this plot is that the velocity computation for all fluid points is dominant. We thus decided to use the FMM for this surface integral (3.55) by approximating as follows: Here, the points $\vec{x}$ are the sources, and $\vec{y}$ are the targets. For the velocity inside and on the aggregate boundary, we use the rigid boundary velocity $u(\vec{x}) = \vec{U}_a + \vec{\Omega} \times (\vec{x} - \vec{x}_{cm})$. This implies that we only use targets located outside the aggregate, and we do not expect any singularity in this computation ($\vec{x} \neq \vec{y}$). However, we may have close evaluation problems. We will discuss the size of errors in the next section.

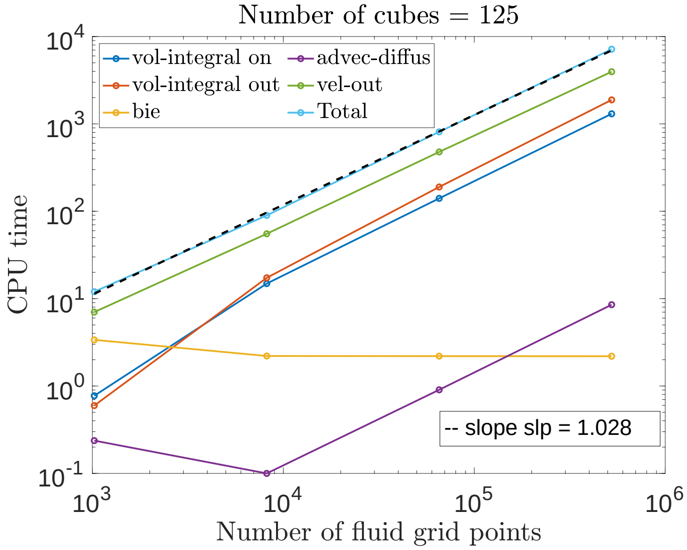

Figure 3.3: CPU time for each computation step in second with an aggregate of 125 cubes for ten time steps.

We handle the integration of the Stokeslet in a manner similar to what was done for the volume integral. Using the Laplace kernel, we can rewrite the surface integral (3.55) as

$$u_H(\vec{y}) = \int_S \vec{f}(\vec{x}) \cdot \left(\frac{\bar{\bar{I}}}{\|\vec{x} - \vec{y}\|} - (\vec{x} - \vec{y})\, \nabla_{\vec{y}} \frac{1}{\|\vec{x} - \vec{y}\|} \right) \, \mathrm{d}S(\vec{x}). \tag{3.56}$$

We first discretize the entire aggregate surface into N_f square faces located at $[cx_j^n - 1, cx_j^n + 1]$, where (cx_1^n, cx_2^n) is the center of n square face. The discretized version of the velocity equation (3.56) is denoted by $H(\vec{y})$,

$$\begin{aligned} H(\vec{y}^m) &= u_H(\vec{y}) - E_f = \sum_{n=1}^{N_f} H^n(\vec{y}^m) \\ &= \sum_{n=1}^{N_f} \vec{f}(\vec{x}^n) \cdot \int_{cx_2^n-1}^{cx_2^n+1} \int_{cx_1^n-1}^{cx_1^n+1} \left(\frac{\bar{\bar{I}}}{\|\vec{x}^n - \vec{y}^m\|} - (\vec{x}^n - \vec{y}^m)\, \nabla_{\vec{y}^m} \frac{1}{\|\vec{x}^n - \vec{y}^m\|} \right) \mathrm{d}x_1 \mathrm{d}x_2, \end{aligned} \tag{3.57}$$

where the error coming from this approximation is denoted as E_f. A more detailed analysis regarding E_f can be found in section 2.4.1. Note that the stress $\vec{f}(\vec{x}^n)$ is assumed to be constant over each square face. One can find that we have a significant error in the cube's corners. We want to ensure that we do not introduce larger errors as we make further approximations.

Next, we need to approximate the surface integral in equation (3.57) using a mid-point rule for a Riemann sum,

$$\begin{aligned} \tilde{H}(\vec{y}^m) &= H^n(\vec{y}^m) - E_G \\ &= \sum_{n=1}^{N_f} \vec{f}(\vec{x}^n) \cdot \sum_{s=1}^{Ns^2} d^2 \left(\frac{\bar{\bar{I}}}{\|\vec{x}_s^n - \vec{y}_s^m\|} - (\vec{x}_s^n - \vec{y}^m)\, \nabla_{\vec{x}_s^n} \frac{1}{\|\vec{x}_s^n - \vec{y}^m\|} \right) - E_G, \end{aligned} \tag{3.58}$$

where E_G is the error coming from the quadrature method. We use N_s^2 sub-squares with sizes of $d = 2/N_s$ and take the center of each sub-squares as the integration point. We take the same number of points, N_s, evenly distributed in one direction. In the schematic, Figure 3.4, the red cross represents the center of the $n-$th square face, (cx_1^n, cx_2^n). The blue dots and the red cross are the integration points. We do not include any boundary values on one square face for simplicity.

As mentioned, we hope to have a small integration error, i.e., $E_G \ll E_f$. To measure E_f, we consider the settling of one cube-shaped aggregate. We then observe the relative error of the vertical velocity on one square face, considering the translational velocity, $\vec{U}_a$, as the exact solution. In Figure 3.5, we see the square face at $x = 1$, where the white dashed line shows the location of the square face, and the color indicates the relative error. It implies that the maximum of 23.12% error occurs at the cube corners. Note that this error made on the drag of a single cube is the worst-case scenario of our simulations. We have confirmed the effect of doubling the resolution of larger aggregates

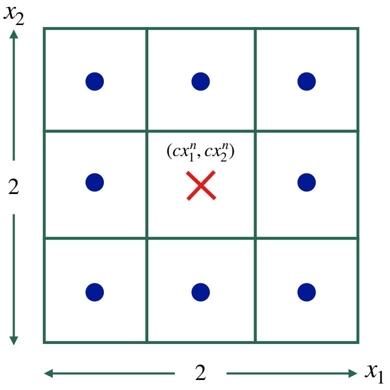

Figure 3.4: Schematic of points we use to approximate the integral of the single-layer potential kernel over one square face.

in Chapter 2. We found changes of less than 2% for the drag and 5% for the torque. We thus would like to control the quadrature error, E_G, by adjusting the total number of integration points, Ns^2.

Two parameters affect the efficiency and accuracy of the FMM computations: 1) the number of quadrature points, N_s^2, and 2) the relative precision ε in the FMM3D library, which determines the number of terms in the series expansion. In Figure 3.6, we vary the number of integration points to choose an optimal value. We test a single-time simulation in the domain, $[-5, 5] \times [-5, 5] \times [-10, 10]$, with the one cube aggregate model. To check the responses of varying ε values, we simulated the same setup with two tolerance values, $\varepsilon = 10^{-1},\ 10^{-6}$. From this analysis, we chose that $Ns = 9^2$ quadrature points as the error is of a size we can tolerate. We had similar results for the $\varepsilon = 10^{-6}$ case. We did not notice any difference in accuracy. We may observe this because the corner error, E_f, dominates our approximation and is already larger than 10%. After implementing the FMM3D library into our program, we checked the compute time to compare the fluid velocity computation previously shown as the green (or dashed line) in Figure 3.3. In Figure 3.7, we observe that the efficiency of the computation increases about ten times when the number of fluid grid points is about 500,00, which is in the range of what we will use to compute the fully stratified simulations.

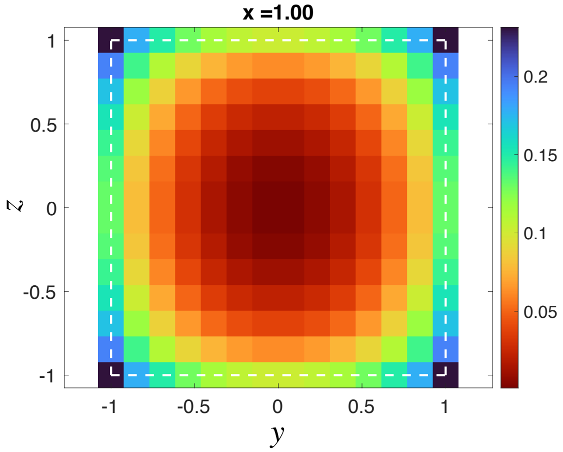

Figure 3.5: Sample case of the relative velocity error on one face, E_f.

3.3.4 Rotation

To have more realistic simulations, we allow our model aggregates to rotate while they settle. In this section, we focus on the angular velocity, $\vec{\Omega} = \Delta\theta/\Delta t$, which tells us how much the aggregate rotates, $\Delta\theta$ in one time step, Δt. This information is stored in the orientation matrix, $\mathcal{Q}(t)$. We can compute the position, $\vec{x}_{\mathcal{R}}(t)$ of a point on the surface of the rotated aggregated using

$$\vec{x}_{\mathcal{R}}(t) = \mathcal{Q}(t)\vec{x}_a,$$

where $\vec{x}_a$ is the position of a point of the aggregate surface relative to the center of mass expressed in a coordinate system that rotated with the aggregate. We note that $\vec{x}_a$ is constant in time and $\mathcal{Q}(0) = \bar{\bar{I}}$ (identity matrix) initially. After we move forward one time step, we update this orientation matrix as

$$\mathcal{Q}(t + \Delta t) = \mathcal{R}\mathcal{Q}(t), \tag{3.59}$$

where $\mathcal{R}$ is a rotation matrix.

We implement updates to the orientation matrix as follows (Polimeno, Kim, & Blanchette, 2022). Assume we obtain the angular velocity, $\vec{\Omega}$, from solving equation (3.42) at every time step. (Initially, it is the zero vector). With this, we can find the three-dimensional change of the angular position vector, $\vec{\Omega}\Delta t = (\Delta\theta_1,\ \Delta\theta_2,\ \Delta\theta_3) \equiv \Delta\vec{\theta}$. The

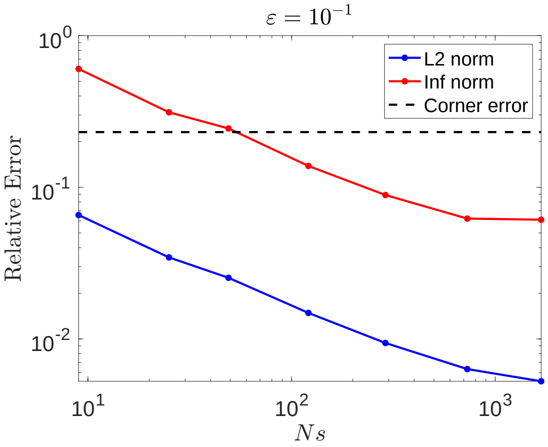

Figure 3.6: Relative error between U^* and U^{*+}, varying the number of integration points: $Ns = [3, 5, 7, 11, 17, 27, 41]^2$ and $\varepsilon = 10^{-1}$.

matrix $\mathcal{A}$ is then defined such that $\mathcal{A}\vec{x} = \Delta\theta \times \vec{x}$,

$$\mathcal{A} = \begin{bmatrix} 0 & -\Delta\theta_3 & \Delta\theta_2 \\ \Delta\theta_3 & 0 & -\Delta\theta_1 \\ -\Delta\theta_2 & \Delta\theta_1 & 0 \end{bmatrix}, \tag{3.60}$$

From here, we have the rotation matrix $\mathcal{R} = e^{\mathcal{A}}$. We can compute the matrix exponential $e^{\mathcal{A}}$ using Rodrigues' formula, for antisymmetric matrices

$$\mathcal{R} = e^{\mathcal{A}} = \bar{\bar{I}} + \frac{\sin(\phi)}{\phi}\mathcal{A} + \frac{1-\cos(\phi)}{\phi^2}\mathcal{A}^2, \tag{3.61}$$

where $\phi = \|\Delta\vec{\theta}\|_2$. With this $\mathcal{R}$ and orientation matrix $\mathcal{Q}$, we are ready to update the fluid grid.

Linear system in a rotated coordinate

We first solve for the stress at the center of each square face of an aggregate, $\vec{y} = \vec{x}_i$, using the same formula as equation (3.26),

$$\vec{u}\left(\vec{x}_i\right) = -\int_S \vec{f}(\vec{x}) \cdot \bar{\bar{G}}\left(\vec{x}, \vec{x}_i\right) \mathrm{d}S - \frac{\alpha C_{max}}{8\pi} \frac{\rho_0}{(\rho_s - \rho_0)(1-\phi)} \int_V C\left(\vec{x}, t\right) \hat{k} \cdot \bar{\bar{G}}\left(\vec{x}, \vec{x}_i\right) \mathrm{d}V,$$

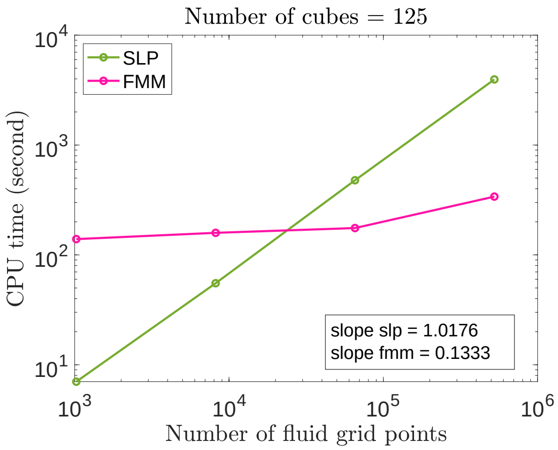

Figure 3.7: CPU time with an aggregate made with 125 cubes for ten time steps. The green line is the velocity computation with the original single-layer potential code, and the pink line represents the approximation using the FMM3D library.

As we allow rotation, we can express the above equation in a rotated frame of reference using $\vec{x}_{r,i} = \mathcal{Q}\vec{x}_i,\ \vec{u}_r = \mathcal{Q}\vec{u}$, and $\vec{f}_r = \mathcal{Q}\vec{f}$,

$$\begin{aligned}\vec{u}_r(\vec{x}_{r,i}) = \mathcal{Q}\vec{u}\left(\mathcal{Q}\vec{x}_i\right) = &-\frac{1}{8\pi}\int_S \vec{f}_r(\mathcal{Q}\vec{x})\cdot\bar{\bar{G}}\left(\mathcal{Q}\vec{x},\mathcal{Q}\vec{x}_i\right)\,\mathrm{d}S \\ &-\frac{\alpha C_{max}}{8\pi}\frac{\rho_0}{(\rho_s-\rho_0)(1-\phi)}\int_V C\left(\vec{x},t\right)\hat{k}\cdot\bar{\bar{G}}\left(\vec{x},\mathcal{Q}\vec{x}_i\right)\,\mathrm{d}V. \end{aligned} \tag{3.62}$$

Since the rotation matrix $\mathcal{Q}$ is constant in space and is a rotation matrix, it is valid to say that

$$\bar{\bar{G}}\left(\mathcal{Q}\vec{x},\mathcal{Q}\vec{x}_i\right) = \bar{\bar{G}}(\vec{x},\vec{x}_i).$$

We now solve for unknowns, including the translational and angular velocities, in a rotated coordinate system $\vec{x}_{r,i}$. Note that the stress values we obtain here are located in the rotated positions. To complete the linear system to solve for stress, translational, and angular velocities, we temporarily map the fluid domain grid into the same coordinate system as the boundary integral term. We can multiply by $\mathcal{Q}^{-1} = \mathcal{Q}^T$ as

$$\begin{aligned}\vec{u}\left(\mathcal{Q}\vec{x}_i\right) = &-\mathcal{Q}^{-1}\left(\frac{1}{8\pi}\int_S \vec{f}_r(\mathcal{Q}\vec{x})\cdot\bar{\bar{G}}\left(\mathcal{Q}\vec{x},\mathcal{Q}\vec{x}_i\right)\,\mathrm{d}S\right) \\ &-\mathcal{Q}^{-1}\left(\frac{\alpha C_{max}}{8\pi}\frac{\rho_0}{(\rho_s-\rho_0)(1-\phi)}\int_V C\left(\vec{x},t\right)\hat{k}\cdot\bar{\bar{G}}\left(\vec{x},\mathcal{Q}\vec{x}_i\right)\,\mathrm{d}V\right). \end{aligned} \tag{3.63}$$

For the other force equations as well, we implement the following

$$\int_S \vec{f}(\vec{x})\,\mathrm{d}S(\vec{x}) = \mathcal{Q}^{-1}\vec{F}_o \tag{3.64}$$

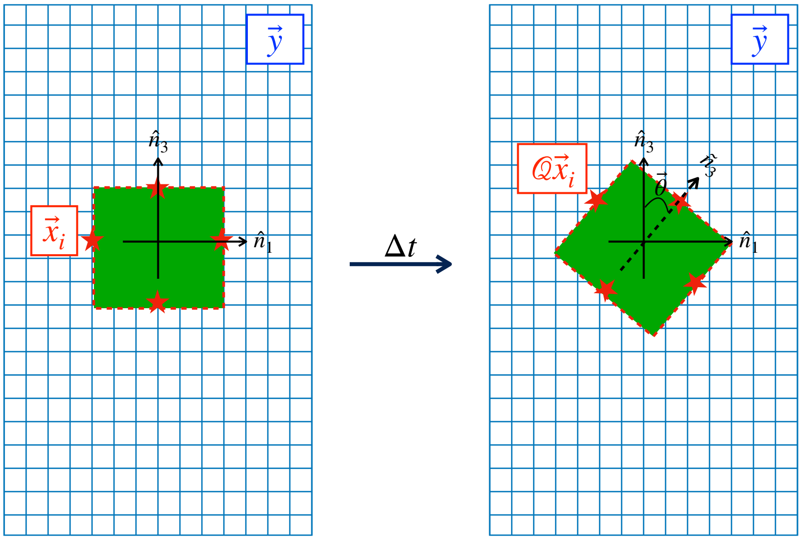

Figure 3.8: Schematics of the rotation of an aggregate. The blue grid is the fluid domain, and the green rectangle represents an aggregate. Red stars show points on the aggregate.

$$\int_S \vec{f}(\vec{x}) \times (\vec{x} - \vec{x}_{cm}) \, \mathrm{d}S(\vec{x}) = \vec{0}. \tag{3.65}$$

Once we solve the linear system, we may return the values on the fluid grid to the Cartesian coordinate system.

Velocity computation

Once we solve the stress, we are supposed to use the same equation (3.26) to solve for velocity in the fluid grid, which stays in the Cartesian coordinates. Although the volume integral term can stay as it is, the boundary integral needs some special treatment since it has two mixed coordinate systems. We particularly pay more attention to the Stokeslet,

$$\bar{\bar{G}}\,(\mathcal{Q}\vec{x}, \vec{y}) = \frac{\bar{\bar{I}}}{||\mathcal{Q}\vec{x} - \vec{y}||} + \frac{(\mathcal{Q}\vec{x} - \vec{y})(\mathcal{Q}\vec{x} - \vec{y})^T}{||\mathcal{Q}\vec{x} - \vec{y}||^3},$$

where $\mathcal{Q}\vec{x}$ is in the rotated frame. Since we cannot compute the boundary integral of the Stokeslet when $\mathcal{Q}\vec{x}$ and $\vec{y}$ are not in the same coordinate system, we need to express $\vec{y}$ using another vector $\vec{v}$ that is in the rotated frame such that

$$\mathcal{Q}\vec{x} - \vec{y} = \vec{x} - \vec{v},$$

or equivalently,

$$\vec{v} = \left(\bar{\bar{I}} - \mathcal{Q}\right)\vec{x} + \vec{y}.$$

After we solve for the velocity field of the fluid domain, we rotate the velocity field back to the original coordinate by multiplying by the inverse of $\mathcal{Q}$ for the concentration update.

3.4 Validation

As we explained in the previous section, the run time of the entire simulation with an aggregate model using 100 cubes, which we desire to observe, may take up to a few weeks. We thus need to determine the parameters to optimize the computing time while maintaining an acceptable degree of accuracy. We examine a smaller simulation, using an aggregate with ten cubes, $NC = 10$, shown in Figure 3.9, by varying 1) domain size via s in Figure 3.9, 2) grid spacing Δx, and 3) time step Δt. Note that we use uniform spacing for all directions, i.e., $\Delta y = \Delta z = \Delta x$. To vary the fluid domain size, we consider the center of mass, $\vec{x}_{cm}$, and maximum radius, R_m, of the aggregate. We use a domain centered at $\vec{x}_{cm}$ of size $2s\,[R_m \times R_m \times 2R_m]$. We note that s is thus the ratio of the domain size to the aggregate diameter. See Figure 3.9.

Since we are interested in the aggregate's long-term settling behavior, we measure its (a) translational velocity $\vec{U}_a$, (b) location of $\vec{x}_{cm}$, and (c) drag $\vec{F}_o$ as a function of time. In particular, we present the vertical component of these three values, focusing on the settling direction. We also want to observe the (d) perturbation $C(\vec{x}, t)$. At locations far from the aggregate, we expect to see very small, almost zero, perturbation. We thus focus on the perturbation value near the aggregate, denoted by $\vec{x}^{\star}$, which is distanced by approximately $(1.2 + R_m)$ from the center of mass.

We show three snapshots of the perturbation C at three different times, obtained with $\Delta t = 0.75,\ \Delta x = 1$, and $s = 5$, at $x = -0.3$ as a sample result in Figure 3.10. Note that the white star point is at $\vec{x}^{\star} = (-0.3,\ 6.9,\ 0.4)$, which is the particular point at which we present C. Since we use the moving frame of reference to compute the perturbation, we see that the aggregate stays in the middle of the fluid domain in Figure 3.10. We notice slight oscillations near the top of the fluid domain, where the zero-flux boundary condition is applied, as the perturbation increases. However, these oscillations remain relatively small and do not extend to the vicinity of the aggregate. We will consider a large enough fluid domain compared to the aggregate size, and study to observe the convergence of the quantities of interest, $\vec{U}_a(t),\ \vec{x}_{cm}(t),\ \vec{F}_o(t)$, and $C(\vec{x}^{\star}, t)$.

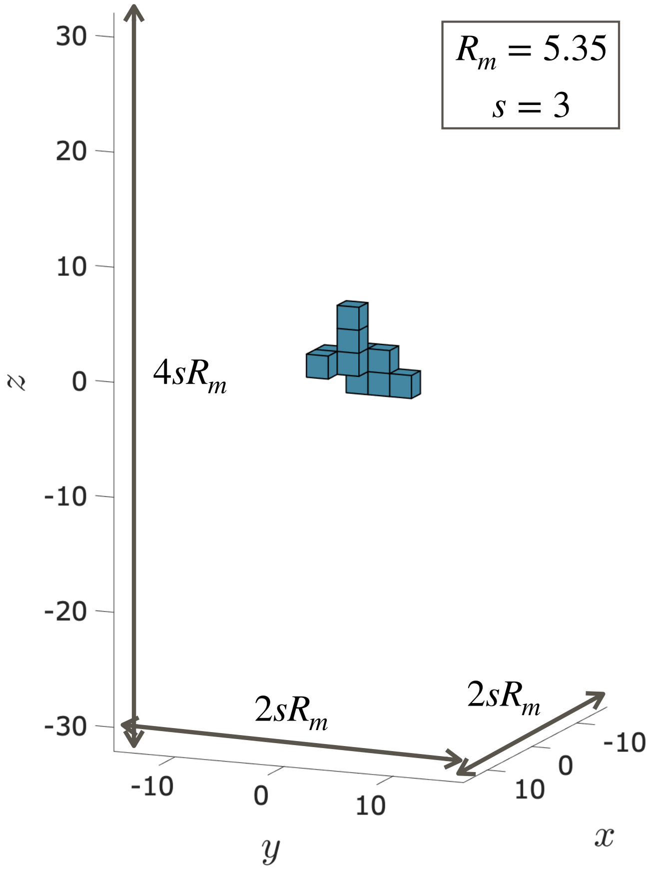

Figure 3.9: Sample aggregate with ten cubes where $s = 3$, that is used to obtain simulations presented in Figure 3.10.

3.4.1 Varying the domain size, via parameter s

As we described in section 2.7.2, we have periodic boundary conditions in the horizontal direction to model an infinite domain where the velocity vanishes to zero. We seek to determine a domain size via the multiplicative factor s, required to approximate these conditions. If we can obtain reasonable results in a smaller domain, we could use smaller s, resulting in more rapid computations and smaller memory requirements.

In Figure 3.11, we present three different domain sizes with the s factor $s = 3,\ 4$, and 5. At first glance, we can barely tell the differences between all three cases. In other words, there is no significant impact on aggregate behavior when reducing the domain size down to $s = 3$. Although we notice that the perturbations at $\vec{x}^{\star}$ show a little more variation with s, this remains a negligible effect.

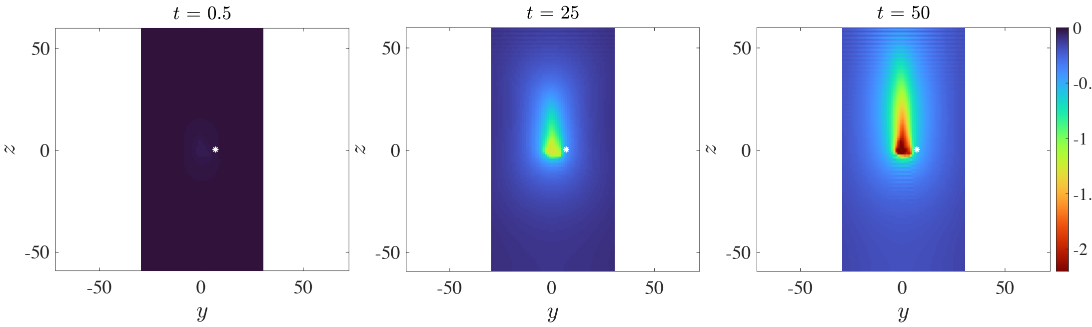

Figure 3.10: Snapshots of the perturbation obtained with $\Delta t = 0.75,\ \Delta x = 1$, and $s = 5$. We look at the $y - z$ plane at $x = -0.3$, which is near the center of mass of the aggregate. The small white dot, $\vec{x}^{\star} = (-0.3,\ 6.9,\ 0.4)$, is located outside of, but very close to, the aggregate.

3.4.2 Varying time step, Δt

We now vary the time step, Δt. We consider three different cases, $\Delta t = 0.75,\ 0.5$, and 0.25. We are able to run simulations with somewhat large time steps since the aggregate size is small enough to have a velocity of order one. When the initial settling velocity is high, the CFL condition (2.57) can be violated, leading to instability. As the aggregate settles, the surrounding fluid becomes denser, which decreases the velocity, and therefore the CFL number. Thus, the velocities are more limited on the time step at the beginning of the simulation.

While we vary Δt, we set the domain size to aggregate diameter ratio $s = 3$ since we observed no critical changes in aggregate dynamics, and we can save computational time. For a fair comparison, we keep the grid size $\Delta x = 1$. The main takeaway of Figure 3.12 is that there are no significant differences in the values we observe when we vary $\Delta t = 0.75,\ 0.5$, and 0.75. Once again, we notice some variations in the perturbation $C(\vec{x}^{\star}, t)$ at later times. However, these remain smaller than 4%.

To more accurately capture the effects of varying Δt, we also present the relative errors between two $\Delta t = 0.25$ and 0.5 in Figure 3.13. It is clear that the errors in all four values are fairly small compared to the error at the corner we found in section 3.3.3 (due to the approximation of constant stress over each face). For the time integration scheme we use, which is the explicit RK2 method, we typically expect to have second-order convergence. These error plots support that our solutions have reached convergence.

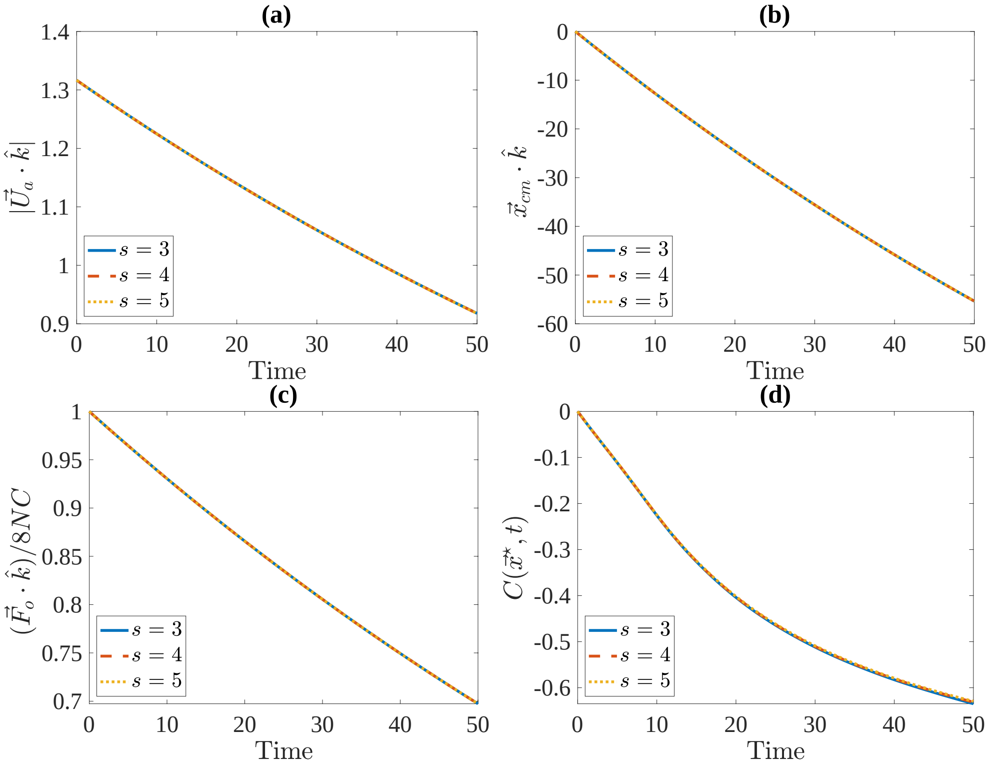

Figure 3.11: Comparison of various domain sizes with $s = 3,\ 4,\ 5$. The time step is $\Delta t = 0.5$, and the grid size is $\Delta x = 1$. We show (a) the settling speed, (b) the position of the center of mass, (c) the vertical force on the aggregate, and (d) the value of the perturbation at $\vec{x}^\star$. Note that $NC = 10$ is the number of cubes used to form the aggregate.

3.4.3 Varying grid size, Δx

Lastly, we perform the simulations with several grid sizes, $\Delta x = 1,\ 2$, and 4. The choice of such large grid sizes is justified by the approximation of constant stress over each face (of side length 2). In general, as long as all three choices produce similar results and have no stability issues, we prefer to use as large Δx as possible to reduce the computational time. The number of fluid grid points can also be a challenge in terms of the computational memory required.

As we saw in the first two validations, we observe quite good agreement presented in the velocity, location, and drag in Figure 3.14. If we had computation time or memory capacity constraints, these results in plots (a), (b), and (c) support that we can still obtain qualitative results to analyze a settling aggregate.

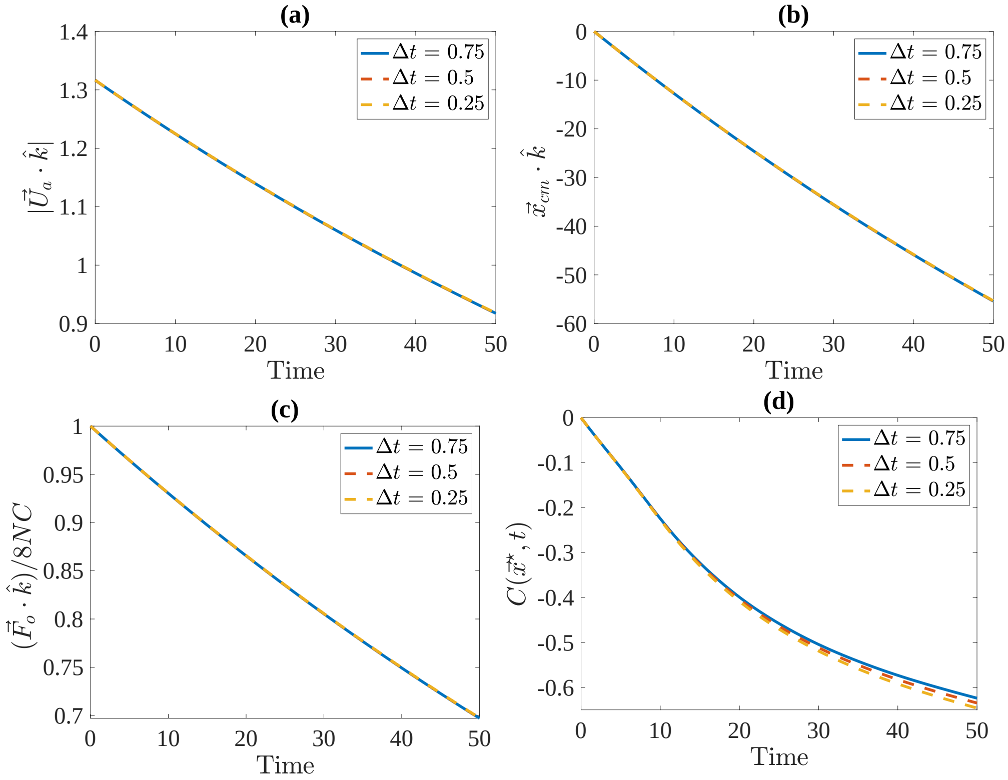

Figure 3.12: Comparison of various $\Delta t = 0.75,\ 0.5,\ 0.25$ in the domain size factor $s = 5$ with $\Delta x = 1$. We show (a) the settling speed, (b) the position of the center of mass, (c) the vertical force on the aggregate, and (d) the value of the perturbation near the aggregate.

For the last plot (d), since we have different grid spacings, we were not able to capture the perturbation at the $\vec{x}^\star$ exactly for $\Delta x = 2$ and 4 cases. We thus used MATLAB built-in function `interp3` to interpolate the C value at location $\vec{x}^\star$. We particularly select the nearest-neighbor method, which finds the value at the nearest sample grid point. We find the interpolation results seem to be reliable, having a good match with previous results of C with various domain and time step sizes.

Before we conclude this section, we want to note that it is difficult to say we obtained the correct solution since we do not have any analytic solutions. The validations we provide here are to exhibit convergence and estimate the size of the errors made due to time and space discretization and finite domain size effects. The results we described in this section were confirmed with simulations of an aggregate made with 50 cubes, and similar trends were observed. We present larger aggregate model simulations in the

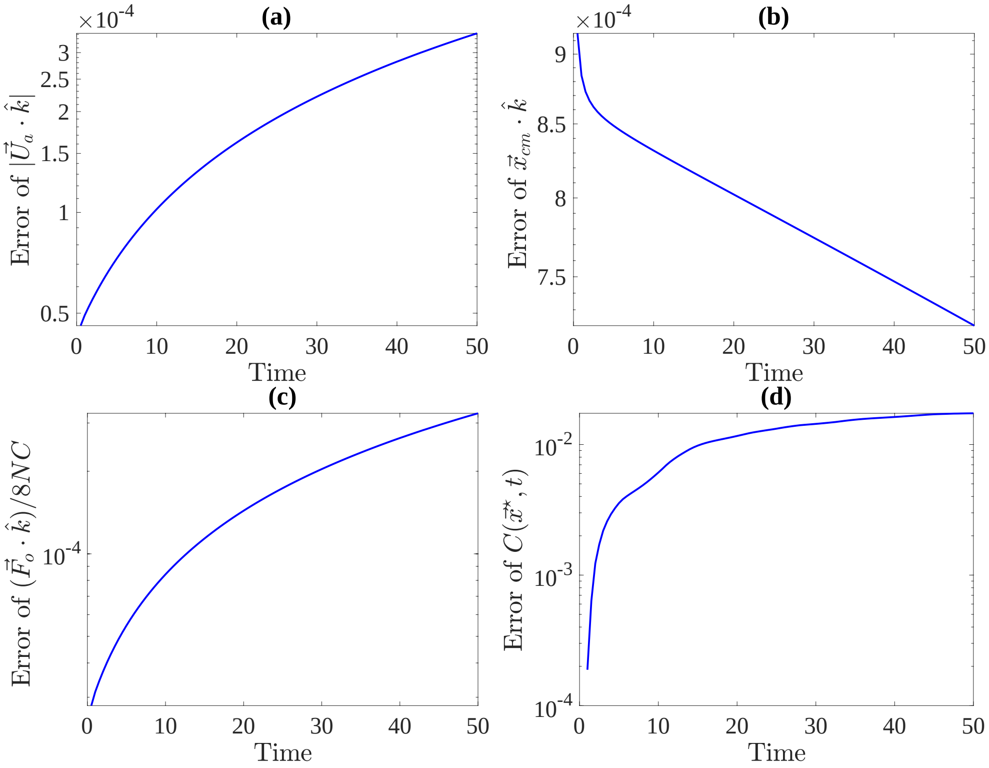

Figure 3.13: Relative error between $\Delta t = 0.5$ and 0.25 cases.

next section.

3.5 Simulation results

3.5.1 Base case analysis

Since there are several parameters we are interested in varying, we decided on setting a base case to compare further simulations. To explore assorted shapes, we used 50 cubes to form an aggregate. We particularly use the aggregate shape in Figure 3.15. To avoid any stability issues while being computationally efficient, we choose the time step size $\Delta t = 0.5$ and grid spacing $\Delta x = 1$. In section 3.4, we have shown that these choices provide good accuracy. Moreover, we found that simulating the settling aggregate in the domain size with the scaling factor $s = 3$ is sufficient to have negligible boundary effects. Also, we apply Pe = 100 as we did for the homogeneous model in Chapter 2.7.4 for this base model.

Additionally, we select the stratification strength γ more systematically. To

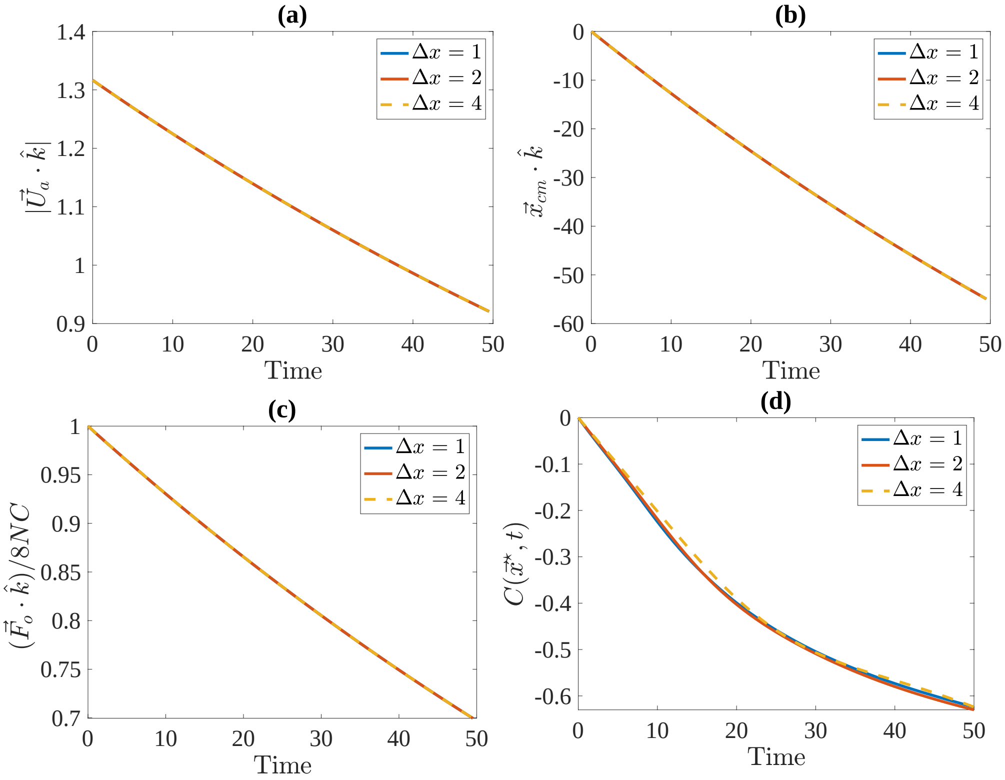

Figure 3.14: Comparison of various $\Delta x = 1,\ 2,\ 4$ in the domain size factor $s = 5$ with $\Delta t = 0.75$. We show (a) the settling speed, (b) the position of the center of mass, (c) the vertical force on the aggregate, and (d) the value of the perturbation near the aggregate.

do so, we first consider the settling distance of an aggregate, denoting it as z_T. In Figure 3.9, we show that the aggregate is initially located in the middle of the domain. We are interested in observing a setup where γ is as large as possible while allowing the aggregate to travel about $z_T = 6R_a$ before reaching its level of neutral buoyancy. Equation (3.1) allows us to compute the background fluid stratification γ

$$\rho_{bg} = \rho_0(1 - \gamma z_T) = \rho_0(1 - \gamma 6R_a) = \rho_a. \tag{3.66}$$

We want the aggregate density ρ_a, which is defined in equation (3.17), to reach neutral buoyancy, assuming its fluid portion ρ_f is ρ_0. For an aggregate composed of 50 cubes, we have an estimated average radius $R_a \approx 9$ (Yoo, Khatri, & Blanchette, 2020), and thus we find $\gamma \approx 4 \times 10^{-4}$.

In Figure 3.16, we show several 2D snapshots, sliced in the middle of the domain ($x = -0.74$), of the perturbation C at various times. Note that we see negative values of

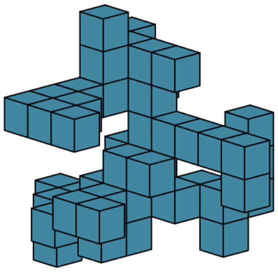

Figure 3.15: The base aggregate model (random seed number 2) with 50 cubes.

C since the perturbation is a concentration difference from the initial concentration. We can observe much higher perturbations around the aggregate that increases in magnitude as time increases as the aggregate entrains the upper-layer solute.

We observe the aggregate behavior more closely in Figure 3.17. As we introduced in the previous section, we measure (a) the settling speed and (b) the normalized total drag of the aggregate. We also exhibit the ratio of total drag to the settling speed in plot (c) as a measure of the coefficient in the linear relationship between drag and velocity that is observed in Stokes flow. Although both settling speed and drag seem to be decreasing over time, we find that their ratio (c) increases non-linearly. This implies that the stratification of the fluid plays a role in the aggregate's settling behavior, not only by reducing the buoyancy but also through the entrained fluid. We would have observed a horizontal line if the surrounding fluid did not affect aggregate motion as it settled in a homogeneous fluid.

In the last plot (d), we observe the perturbation at a particular location outside the aggregate boundary. It is the white star point $\vec{x}^{\star} = (-0.74, 12.74, 0.24)$ in Figure 3.16. This point is approximately (1.01 + R_m) away from the center of mass of the aggregate. The perturbation is expected to grow over time in magnitude at this point. As the settling motion slows down, the magnitude of perturbation also smoothes out.

In the next section, we explore various shapes of aggregates made with 50 cubes in addition to the base case. Afterward, we will observe the effects of varying Péclet numbers and background fluid density stratification γ.

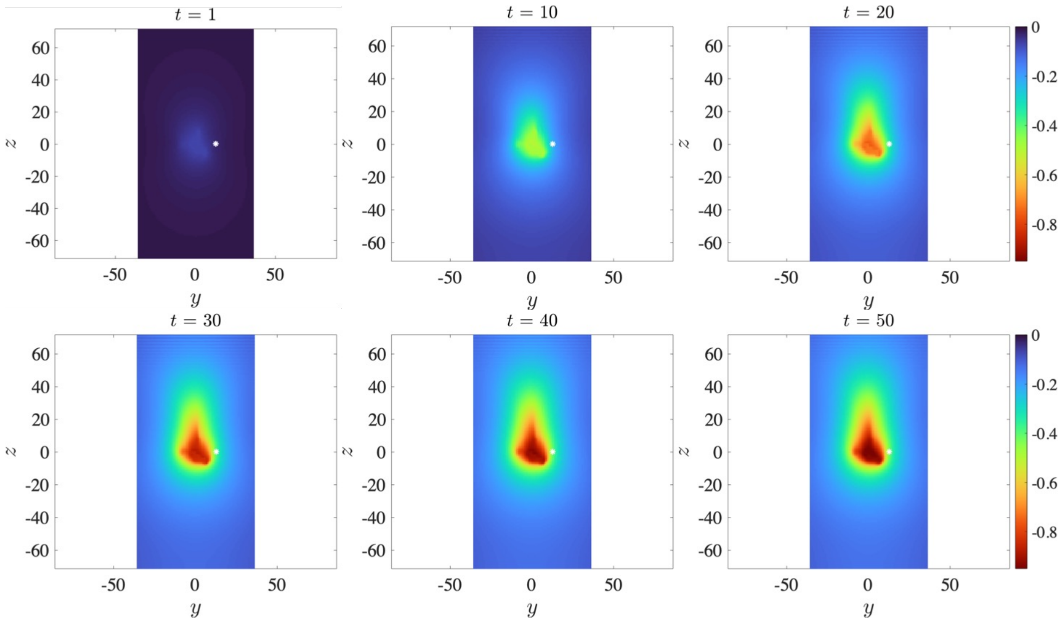

Figure 3.16: Concentration dynamics with the base model case at various times.

3.5.2 Various shapes of aggregates

We first run simulations with randomly shaped aggregates using 50 cubes, in addition to the base case model that is the random seed #2. We create more aggregates, numbering the random seeds from #11 to #15 as shown in Figure 3.18, as well as seeds #21 to #35. With these six sample aggregates, we examine their behaviors. Results are presented in Figure 3.19.

There are some variations (less than 16%) in aggregates settling behaviors, yet their speed, drag, and $\vec{x}_{cm}$ locations seem to have overall similar motions. Meanwhile, plot (c) shows larger differences between each aggregate shape. We find this interesting feature that the drag-velocity ratio spread shows approximately a 12% difference range and 5% away from their mean value (at the final time). Note that the sample mean value at the final time $t = 50$ is about 0.3241. This demonstrates that modeling an aggregate with a simplified shape, such as a sphere, cannot accurately capture all physical forces involved.

Based on this mean value of six samples, we can estimate the number of random seeds, N_{sd}, that we should simulate to obtain a finer result. In particular, we want to get the N_{sd} such that the relative error between the standard error (SE) and standard error

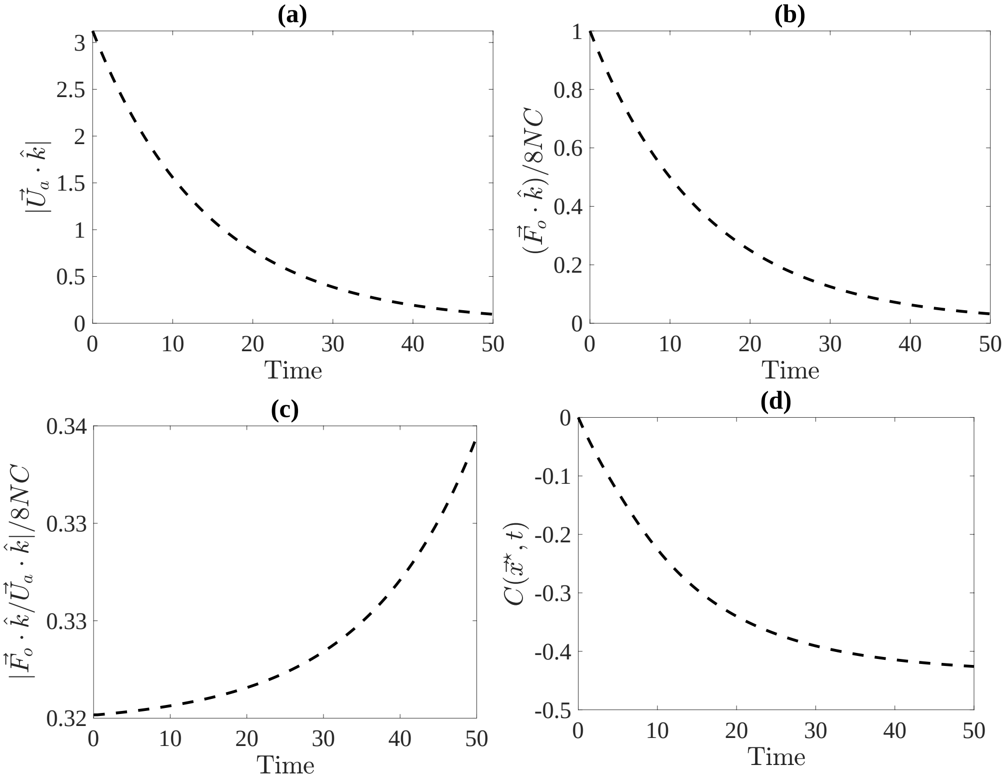

Figure 3.17: Comparison of various Péclet numbers. We show (a) the settling speed, (b) the vertical component of normalized drag force on the aggregate, (c) the ratio of (b) to (a) values, and (d) the perturbation at position $\vec{x}^{\star}$.

of the mean (SEM) is 1%, i.e.,

$$\frac{|SE\ -\ SEM|}{SE} < 1(\%). \tag{3.67}$$

In our case, we have

$$SE\ = \frac{\text{Standard deviation with all } N_{sd}}{\sqrt{N_{sd}}} \tag{3.68}$$

and

$$SEM\ = \frac{\text{Standard deviation of 6 samples}}{\sqrt{6}}. \tag{3.69}$$

However, since we do not know the numerator of SE, we assume that it is the same as the sample standard deviation. We then can solve for $N_{sd} \geq 37$. In the future, we plan to run simulations with N_{sd} many different randomly formed aggregates.

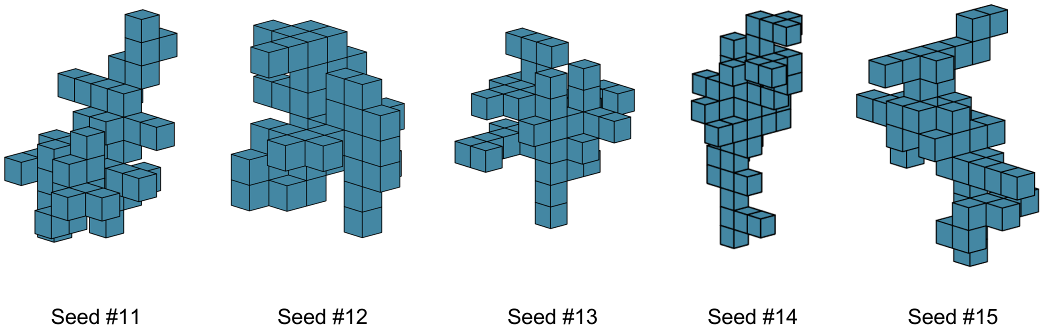
Seed #11 Seed #12 Seed #13 Seed #14 Seed #15

Figure 3.18: Five sample aggregates composed of 50 cubes.

3.5.3 Various Péclet number, Pe

Next, we vary Péclet numbers, Pe $= 1$ and 10, comparing the simulations to the base case for which Pe = 100. As a smaller Péclet number implies more diffusive effects, we look for differences in perturbation. Since we have more numerical instability for lower Péclet numbers, we reduce the time step size to $\Delta t = 0.1$ for all three Péclet number cases.

Figure 3.20 shows no drastic variations between all three Péclet numbers, especially for the velocity and total drag. Focusing on the perturbation plot (d), we can see that more diffusion occurs for the smallest Péclet, Pe = 1, having a steady perturbation value after time $t = 30$. Overall, it is clear that all four plots agree well with our expectations, even though the impact of varying the Péclet number is small in this regime.

3.5.4 Various stratification strength, γ

Lastly, we investigate three different stratification strengths,

$$\gamma = 10^{-4} \times [\,1,\ 4\ \text{(base case)},\ 6\,]\,.$$

We anticipate observing variations in both aggregate and fluid dynamics as we change the γ value. Note that every other parameter is the same as in the base case.

We first present quantities of interest the aggregate itself in Figure 3.19. In plot (a), we see that the settling speed of the aggregate decreases faster when the fluid density

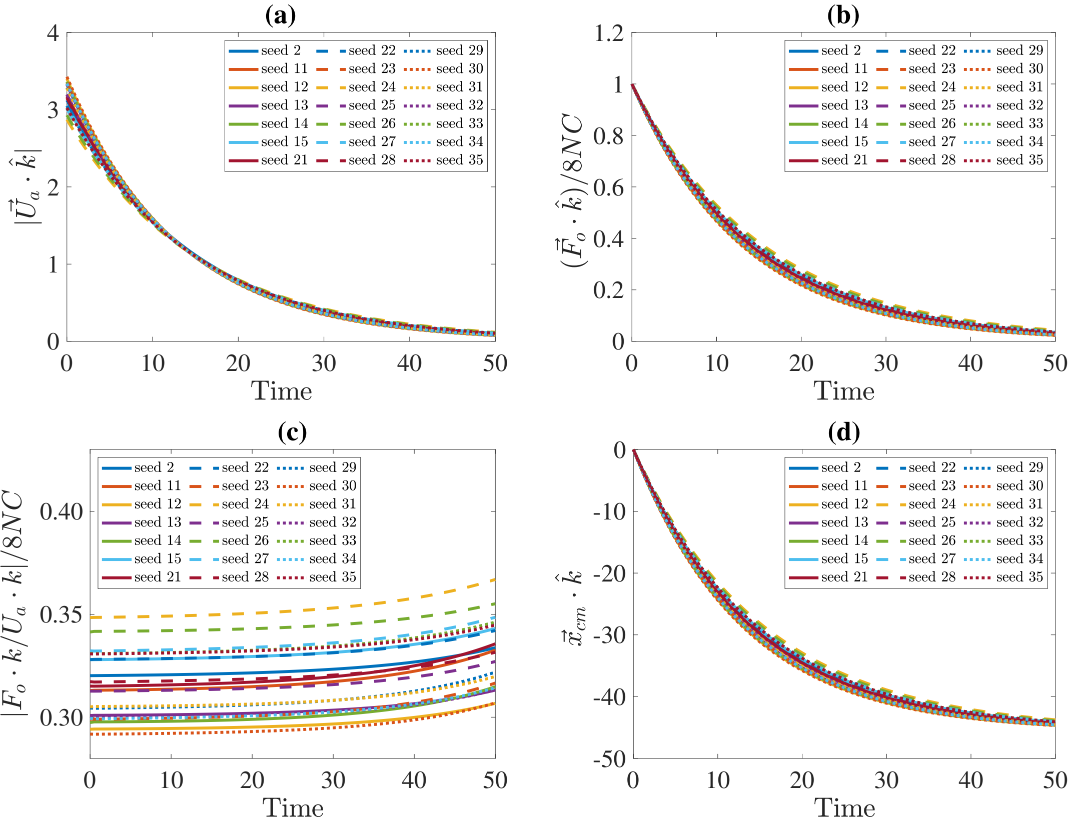

Figure 3.19: Comparison of various shapes of aggregates made with 50 cubes. We show their (a) settling speed, (b) drag force on the aggregate in the settling direction, (c) ratio of (b) to (a) values, and (d) position of the center of mass.

gradient is sharper. Similar results are shown for the total drag over time in plot (b). To clarify, we present the ratio of the drag to the settling speed in plot (c). We observe very similar behavior as in the homogeneous fluid case with the smallest $\gamma = 10^{-4}$. Note that this γ is considered a small value for the aggregate radius $R_a \approx 9$. For instance, the same γ may be a large enough value to observe a clear background fluid stratification effect for an aggregate radius 20. We also look at the center of mass of aggregate over time. Since $\gamma = 10^{-4}$ mimics a homogeneous fluid, the aggregate travels more, yet with a slower speed, demonstrated by the blue solid line in plot (d).

From a fluid perspective, we obtain the perturbation over time at two different points. In Figure 3.22, the left plot is the perturbation at the usual point, $\vec{x}^{\star}$, where the white star is located in Figure 3.16. It is located outside of the aggregate, yet very close.

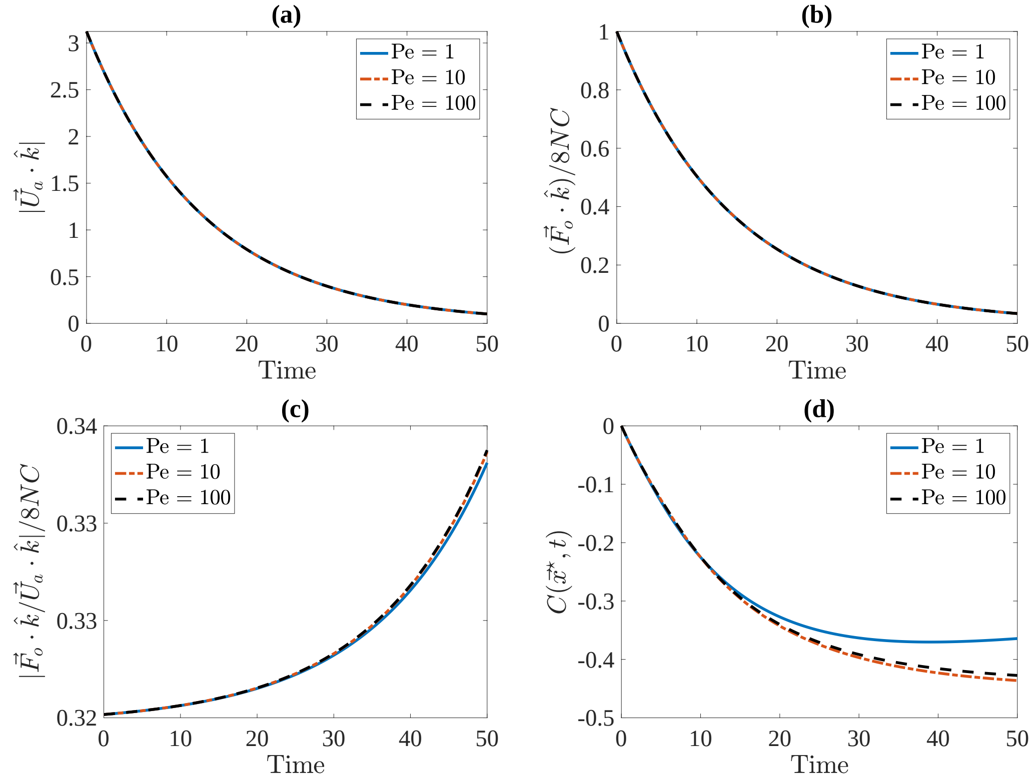

Figure 3.20: Comparison of various Péclet numbers. We show (a) the settling speed, (b) the vertical force on the aggregate, (c) the ratio of (b) to (a) values, and (d) the value of the perturbation near the aggregate.

On the right side, we examine the perturbation inside of the aggregate, particularly at the center of the fluid domain. By looking at the magnitude of C, there are certainly higher perturbations for all three γ cases at $\vec{x}_m$. Moreover, the perturbation varying range is quite large for the light stratification case (blue line). As we mentioned, it is because the same aggregate stops moving in a stronger density-stratified fluid due to reaching neutral buoyancy.

3.6 Conclusion

As an extension of our study of the homogeneous system (Yoo, Khatri, & Blanchette, 2020), we have developed a numerical method to simulate a settling marine aggregate, randomly formed with cubes, using a boundary integral method in a density-

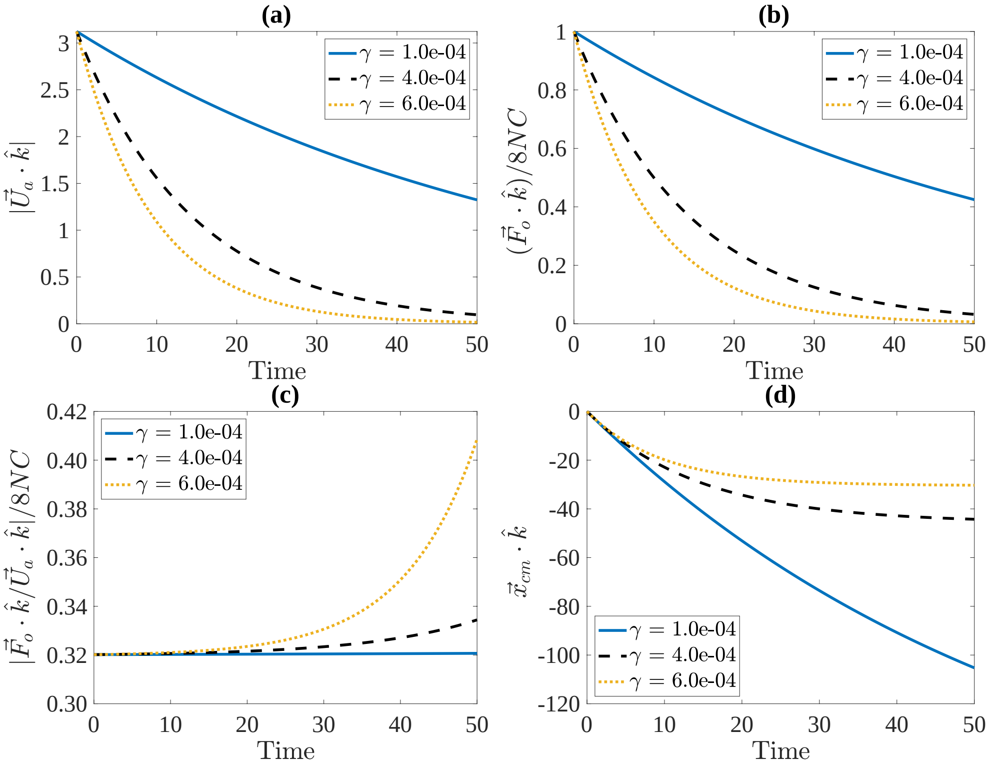

Figure 3.21: Comparison of various background density stratification strengths. We show (a) the settling speed, (b) the vertical force on the aggregate, (c) the ratio of (b) to (a) values, and (d) the position of the center of mass

stratified fluid. Applying the net force equilibrium in a Stokes regime, we prescribed the total drag and torque to solve for the stress on the aggregate and its settling velocity using the single-layer potential formula. With the velocity field obtained, we advance the perturbation in time using the advection-diffusion equation. To accelerate the evaluation of integrals of Stokeslet, we incorporate the Fast Multipole Method by modifying the Laplace kernel.

We have validated our methods by providing results of a settling aggregate composed of 10 cubes while varying the spatial grid, time steps, and domain sizes. Most of the errors for each comparison appeared to be much smaller than those resulting from assuming that the stress is uniform on each square face of a cube.

Furthermore, we simulated larger aggregates, made with 50 cubes, in different settings. We have observed aggregate settling behavior before its density matches the surrounding fluid density. We found a consistent trend in the settling behaviors between

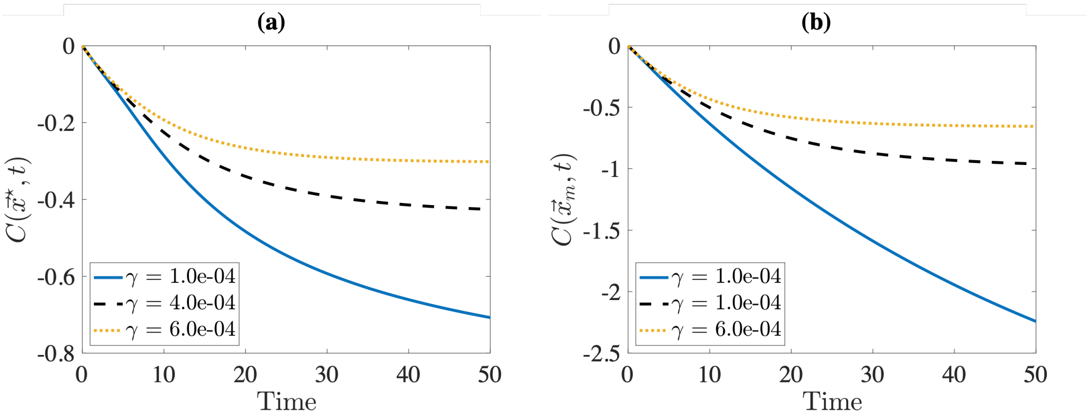

Figure 3.22: Perturbation with various γ at (a) the star position $\vec{x}^{\star}$, outside the aggregate, and (b) the center of the fluid domain, inside the aggregate.

different shapes of aggregates with, for example, variations in the drag coefficient of the order of 8%. In future work, we can simulate aggregates with more cubes and consider more different shapes for better statistical results. kk Under the different Péclet number environments, we find the main changes in the perturbation, as expected, between Pe = 1 and Pe = 10. Since a smaller Péclet number implies a higher diffusivity, the perturbation near the aggregate slows down 10% faster than the other two cases.

We also explore various stratification strengths via γ values. Marine aggregates are highly porous and sensitive to surrounding fluid density stratification (Prairie et al., 2013). Our results also support these characteristics while we perform the simulations with three types of background fluid density gradients. In addition to our results in this thesis, potential future work includes considering another applicable regime with different parameters.

We note that a description of rotational flow results is missing, although we have allowed a rotation of an aggregate while obtaining all the numerical results. In short, we have found an approximate torque having the order $\mathcal{O}(10^{-4})$. This is quite a small value compared to the drag force and perturbation effects as a response to the background fluid stratification. We consider analyzing more details as future work.

There are several branches we can extend our research further with our comprehensive numerical tools developed. As much research work has been done with a sphere model as an aggregate, we would like to compare our results, such as the settling speed, drag acting on the aggregate, and the amount of concentration entrained.

Chapter 4

Continuum modeling of a complex fluid

In this chapter, I report the internship research I began at LBNL in the summer of 2022 that I have continued to work on as part of my doctoral studies. We begin with elaborating more details of Figure 1.2 from Chapter 1.3.

4.1 Rate-dependent flow

In general, most non-Newtonian behaviors of complex fluids can be captured via shear rate dependency. We can describe rate-dependent flow with the following power law (Herschel & Bulkley, 1926). We then have the viscous stress tensor,

$$\boldsymbol{\tau} = 2^n \tilde{\mu} \dot{\gamma}^{n-1} \boldsymbol{D}, \tag{4.1}$$

where $\tilde{\mu}$ is the constant viscosity under zero shear rate and n is the flow behavior index that can be determined experimentally depending on the materials. We also recall that the magnitude of strain rate is $\dot{\gamma} = |\boldsymbol{D}|$. Note that this value can be computed by applying the scaled Frobenius norm for a second-order tensor,

$$\dot{\gamma} = |\boldsymbol{D}| = \sqrt{\frac{1}{2} \mathrm{tr}\,(\boldsymbol{D}\boldsymbol{D}^T)}.$$

The relationship between rate-dependent flow and shear rate can be addressed with the *apparent viscosity* function, η,

$$\eta(\dot{\gamma}) = 2^{n-1} \tilde{\mu} \dot{\gamma}^{n-1}. \tag{4.2}$$

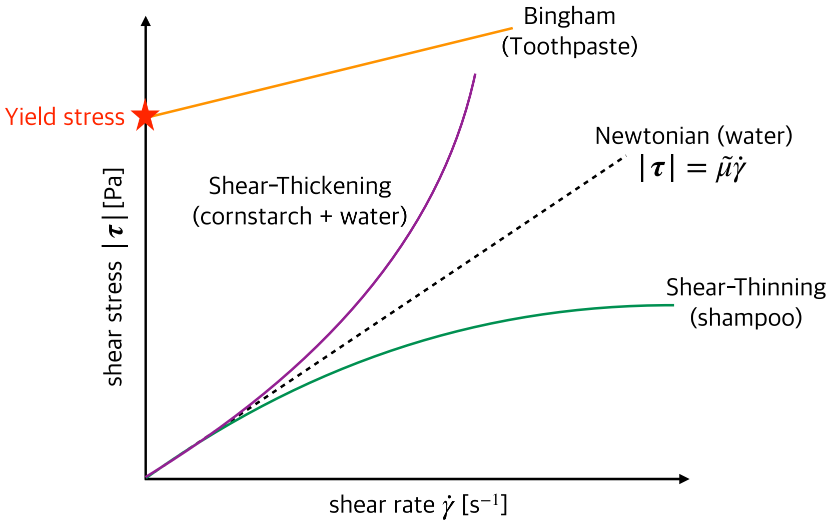

Figure 4.1: Relationship between apparent viscosity and shear rate. The plot is drawn based on (Irgens, 2014). The value μ_∞ is the asymptotic viscosity at high shear rate.

We show the variation of apparent viscosity depending on the shear rate in Figure 4.1. The black dashed line can be found when $n = 1$ in equation (4.2) where the Newtonian fluid viscosity $\tilde{\mu}$ as introduced in equation (1.3). Furthermore, the purple and green lines in Figure 4.1 imply that the shear-thinning and thickening behaviors can be found when $n < 1$ and $n > 1$, respectively.

As we have shown in Figure 1.2 in Chapter 1.3, a Bingham fluid is a particular case of the rate-dependent flow. Bingham fluid behaves as a solid, like plastic, under stress less than the yield stress and begins flowing like a fluid with varying viscosity. This is why it is classified as a *viscoplastic* fluid. The rheological equations describing Bingham fluid (Bingham, 1917) with yield stress τ_0 are,

$$\begin{cases} \boldsymbol{D} = 0, & \text{if } |\boldsymbol{\tau}| < \tau_0 \\ \boldsymbol{\tau} = \left(2\tilde{\mu} + \frac{\tau_0}{\dot{\gamma}}\right)\boldsymbol{D}, & \text{if } |\boldsymbol{\tau}| \geq \tau_0, \end{cases} \tag{4.3}$$

and its corresponding apparent viscosity is

$$\eta = \tilde{\mu} + \frac{\tau_0}{2\dot{\gamma}}, \tag{4.4}$$

when $|\boldsymbol{\tau}| \geq \tau_0$. To illustrate more general yield stress fluids, (Sverdrup, Nikiforakis, & Almgren, 2018) proposed the constitutive equations by combining equations (4.1) and (4.3),

$$\begin{cases} \boldsymbol{D} = 0, & \text{if } |\boldsymbol{\tau}| < \tau_0 \\ \boldsymbol{\tau} = \left(2^n \tilde{\mu} \dot{\gamma}^{n-1} + \frac{\tau_0}{\dot{\gamma}}\right) \boldsymbol{D}, & \text{if } |\boldsymbol{\tau}| \geq \tau_0, \end{cases} \tag{4.5}$$

When $n = 1$, we recover the Bingham fluid.

As it is implied in equation (4.5), we obtain the yield stress of a fluid as $|\boldsymbol{\tau}| \to \tau_0$. When we solve for τ_0 in equation (4.5), we see that

$$2^n \tilde{\mu} \dot{\gamma}^n + \tau_0 \to \tau_0, \tag{4.6}$$

due to $|\boldsymbol{D}| = \dot{\gamma}$, and thus, we should have

$$\dot{\gamma} \to 0. \tag{4.7}$$

Note that the computation of $\boldsymbol{\tau}$ is already implemented for a general rate-dependent fluid in AMReX. In the implementation, they use the Papanastasiou regularization method (Papanastasiou, 1987). By introducing a small parameter, denoted as ε, we can regularize the singularity of $\dot{\gamma}$ as following,

$$\frac{1}{\dot{\gamma}} \to \frac{1 - e^{-\dot{\gamma}/\varepsilon}}{\dot{\gamma}} \tag{4.8}$$

for $\dot{\gamma}/\varepsilon \gg 1$. Otherwise, we simply use $1/\varepsilon$. The detailed mathematics and analysis can be found in (Sverdrup, Nikiforakis, & Almgren, 2018).

4.2 Second-order strain rate rheolgy

Once we obtain the stress tensor $\boldsymbol{\tau}$ for a complex fluid, we can incorporate the varying viscosity into the incompressible Navier-Stokes equations, which are introduced in (1.1) and (1.2), recalling here,

$$\nabla \cdot \vec{u} = 0$$
$$\frac{\partial \vec{u}}{\partial t} + \vec{u} \cdot \nabla \vec{u} = \frac{1}{\rho} \left(-\nabla P + \nabla \cdot \boldsymbol{\tau} + \rho \vec{g}\right),$$

to obtain the flow velocity, $\vec{u}$. We include a viscous stress tensor of the form,

$$\boldsymbol{\tau} = \nu_0 \boldsymbol{A}_1 + \nu_1 \boldsymbol{A}_1^2 + \nu_2 \boldsymbol{A}_2, \tag{4.9}$$

where ν_0 is constant in shear flow, and ν_1 and ν_2 are a function of the shear rate $\dot{\gamma}$. The second-order form of the deviatoric stress tensor, equation (4.9), was introduced by

Colemann and Noll (Coleman & Noll, 1960). The term $\boldsymbol{A_i}$ is the Rivlin-Ericksen tensor, defined as

$$\boldsymbol{A}_1 = \nabla\vec{u} + (\nabla\vec{u})^T = 2\boldsymbol{D} \tag{4.10}$$

and

$$\boldsymbol{A}_2 = \frac{\partial \boldsymbol{A}_1}{\partial t} + \vec{u}\cdot\nabla\boldsymbol{A}_1 + \boldsymbol{A}_1\nabla\vec{u} + (\nabla\vec{u})^T\boldsymbol{A}_1. \tag{4.11}$$

Note that the general form of the Rivlin-Ericksen tensor can be extended to order n,

$$\boldsymbol{A}_{n+1} = \frac{\partial \boldsymbol{A}_n}{\partial t} + \vec{u}\cdot\nabla\boldsymbol{A}_n + \boldsymbol{A}_n\nabla\vec{u} + (\nabla\vec{u})^T\boldsymbol{A}_n. \tag{4.12}$$

For polymer solutions, the most studied in non-Newtonian fluids, it is well-known that the effect of the $\mathcal{O}\left(\boldsymbol{D}^2\right)$ term is small enough to ignore, compared to $\mathcal{O}\left(\boldsymbol{D}\right)$ (Bird, Armstrong, & Hassager, 1987). For this reason, the effect of $\mathcal{O}\left(\boldsymbol{D}^2\right)$ has been neglected in many research works for a complex fluid. For other materials, however, there are potentially important characteristics we should pay attention to considering the stress with higher-order terms in $\boldsymbol{D}$, including granular materials. As a first step, we thus explore the second-order rheology with granular materials.

4.3 Granular rheology

We model a new stress tensor $\boldsymbol{\tau}$ with a second-order strain rate that describes non-isotropic material flow properties,

$$\bar{\bar{\sigma}} = -P\bar{\bar{I}} + \boldsymbol{\tau} = -P\bar{\bar{I}} + \mu_1(\dot{\gamma})\mathcal{O}(\boldsymbol{D}) + \mu_2(\dot{\gamma})\mathcal{O}(\boldsymbol{D}^2). \tag{4.13}$$

In this section, we focus on the methodology to compute the viscosity $\mu_i(\dot{\gamma})$ $(i = 1, 2)$ under the simple shear flow. In (Srivastava et al., 2021), a new stress tensor is presented to describe a non-isotropic flow as follows,

$$\boldsymbol{\tau} = \mu_1(\dot{\gamma})\boldsymbol{D} + \mu_2(\dot{\gamma})\left[\boldsymbol{D}^2 - \frac{\text{tr}\left(\boldsymbol{D}^2\right)}{3}\boldsymbol{I}\right], \tag{4.14}$$

where

$$\mu_1(\dot{\gamma}) = \left(\eta_1\dot{\gamma} + \kappa_1\right)\frac{1}{\dot{\gamma}}, \tag{4.15}$$

and

$$\mu_2(\dot{\gamma}) = \left(\eta_2\dot{\gamma}^2 + \kappa_2\right)\frac{1}{\dot{\gamma}^2}. \tag{4.16}$$

As a particular application to equation (4.9), the form (4.16) is derived under two conditions: (1) the flow motion is simple with a constant stretch by neglecting deformation history, and (2) the flow is isochoric, having uniform properties along streamlines and $\mathrm{tr}(D) = 0$. Note that the last term in equation (4.14) with $\mathrm{tr}(\boldsymbol{D}^2)$ appears to show the pressure dependency of the granular material, in addition to the hydrostatic pressure P (Rajagopal, 2006).

The flow functions, η_i and κ_i for $i = 1, 2$, have the following dependence on total stress: each $\eta_i(\dot{\gamma}, p)$ is (shear) rate-dependent and $\kappa_i(p)$ is (shear) rate-independent. We shall explain the details of these two types of functions in the following sub-section.

4.3.1 $\mu(I)$ rheology

The key to modeling the η_i and κ_i terms is the well-known $\mu(I)$ relationship developed by (Jop, Forterre, & Pouliquen, 2006). Here, I is the *inertial number*,

$$I = \frac{\dot{\gamma} d}{\sqrt{P/\rho_p}}, \tag{4.17}$$

where d and ρ_p are the average particle diameter and density of a given granular material. This dimensionless quantity describes the ratio of the average static force to the inertial force between granular particles, (Jop, Forterre, & Pouliquen, 2006) interpreted the inertial number as the ratio between a macroscopic deformation and an inertial timescale.

To understand the granular flow regimes depending on the inertial number. We consider an hourglass example. As we can see in Figure 4.2, three different states

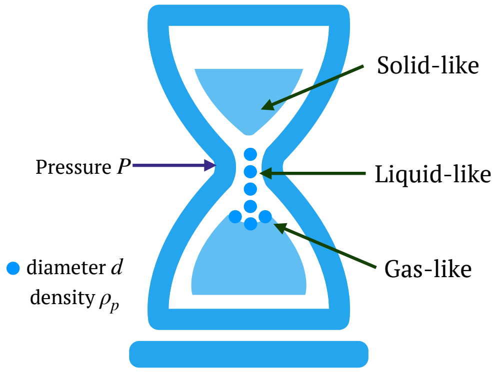

Figure 4.2: Schematics of granular flow with an hourglass example.

can co-exist in granular materials. In the top part of the hourglass, filled with sand, the particles seem not to move and resemble a solid. In the middle nozzle of the hourglass, we can observe the sands passing through the nozzle, flowing like a liquid. Meanwhile, the sand landing on the bottom part of the hourglass forms a cone shape. When we look very closely at the top of the cone, we can see that the sand is falling and colliding, behaving like a gas.

In general, these three regimes can be categorized by the inertial number I. The solid-like state appears when I is small. As I increases, the granular material deformation occurs rapidly, as we see in the middle of the hourglass. The collisional flow, acting like a gas, can be observed for a large I number.

Srivastava (Srivastava et al., 2021) developed a calibration to obtain the coefficients η_i and κ_i, for $i = 1,\ 2$, by applying the $\mu(I)^g$ rheology for granular materials,

$$\mu(I)_i^g = \mu_i^0 + A_i I^{i\alpha_i} = \frac{(\eta_i \dot{\gamma}^i + \kappa_i)}{P}, \tag{4.18}$$

where μ_i^0, A_i, and α_i are fitting parameters, depending on the materials. Note that $\mu(I)^g$ is a dimensionless function of I. By substituting the inertial number I, equation (4.17), into equation (4.18), we get

$$\mu_i^0 + A_i \left(\frac{\dot{\gamma} d}{\sqrt{P/\rho}} \right)^{i\alpha_i} = \frac{(\eta_i \dot{\gamma}^i + \kappa_i)}{P}. \tag{4.19}$$

We then can find the viscous terms (4.15) and (4.16),

$$\mu_i(\dot{\gamma}) = P \left(\mu_i^0 + A_i \left(\frac{\dot{\gamma} d}{\sqrt{P/\rho}} \right)^{i\alpha_i} \right) \frac{1}{\dot{\gamma}^i} \tag{4.20}$$

Note that we can obtain the fitting parameters from particle-based simulations for granular materials, such as the discrete element method (DEM). The following parameter values are introduced in (Jop, Forterre, & Pouliquen, 2006) and (Srivastava et al., 2021):

$$0.09 \le \mu_1^0 \le 0.33, \qquad 0.37 \le \alpha_1 \le 0.7$$

$$0.01 \le \mu_2^0 \le 0.1, \qquad 0.28 \le \alpha_2 \le 0.44.$$

One can find the corresponding A_i values in (Srivastava et al., 2021). Note that we use the following regularization,

$$\frac{1}{\dot{\gamma}^2} \to \frac{1 - e^{-\dot{\gamma}^2/\varepsilon}}{\dot{\gamma}^2}, \tag{4.21}$$

for a higher-order strain rate.

4.3.2 Hydrostatic pressure dependency

For granular rheology, it is typical to see compressible flow. It is, thus, essential to take pressure into account to evaluate the viscosity as seen in equation (4.20). Here, we consider the pressure as a combination of background flow pressure, P_0, that is linear in the vertical direction, z, and a perturbation, P', such that

$$P = P_0(z) + P'(x, y, z).$$

Note that the perturbations are due to gravity. Without a gravitational force, we may simply input the pressure, P_0, constant over time.

In case gravity is involved, we consider the density term in order to approximate the perturbation, as

$$\rho = \rho_0 + \rho'(x, y, z),$$

where ρ_0 is constant and ρ' is a spacially-dependent density perturbation of the flow. Here, we assume that

$$\nabla P_0 = \frac{dP_0}{dz} \approx \rho_0 g. \tag{4.22}$$

This recovers our momentum equation. As we would like to construct a background pressure that stays constant over time for our granular rheology, we may use this assumption. By integrating both sides of equation (4.22), we obtain

$$P_0 \approx p_{bg} + \nabla P_0 z. \tag{4.23}$$

We would like to use this form since we already have the p_{bg} term implemented in the AMReX-incflo code. When we have periodic boundary conditions in the gravity direction, we might need to prescribe a pressure gradient to have an additional pressure effect.

The challenge we faced in implementing the pressure-dependent flow was connecting the pressure in addition to the strain rate into the rheology code. We also need to use a different module than the AMReX-incflo for a compressible flow. We thus leave the pressure-dependent granular flow as a future work.

4.4 Numerical method

In this section, we demonstrate the numerical method used to solve the flow velocity with incompressible Navier-Stokes equations incorporating the viscosity (4.20).

We particularly focus on the time integration that we wanted to improve as we consider the second-order strain rate stress tensor. The main AMReX-incflo library provides three different time integration methods: 1) explicit Euler, 2) Crank-Nicolson, and 3) implicit Euler methods. Since we have the stress tensor $\boldsymbol{\tau}$ of the form (4.9), which is non-linear in the velocity, the most convenient choice was the explicit Euler method. However, it would be beneficial to have another scheme for more stability, efficiency, and accuracy.

We consider a two-stage Runge-Kutta (RK2) method to achieve second-order convergence. In particular, we implemented the following scheme,

$$\vec{u}^{temp} = \vec{u}^n + \frac{\Delta t}{2}\boldsymbol{F}\left(\vec{u}^n\right) \tag{4.24}$$

$$\vec{u}^* = \vec{u}^n + \Delta t \boldsymbol{F}\left(\vec{u}^{temp}\right), \tag{4.25}$$

where

$$\boldsymbol{F}\left(\vec{u}^n\right) = -\vec{u}^n \cdot \nabla \vec{u}^n + \frac{1}{\rho}\Big(-\nabla P^n + \nabla \cdot \boldsymbol{\tau}(\vec{u}^n) + \rho \vec{g}\Big).$$

where the superscript n represents the current time (known) value; $\vec{u}^n \approx \vec{u}(\vec{x}, t_n)$. The new velocity value $\vec{u}^*$ is an updated velocity to the next time, $\vec{u}^* \approx \vec{u}(\vec{x}, t_{n+1})$. Note that the *temp* time is considered to be $n + n/2$. One important part of being consistent is that we only update the one time step with Δt, from the time n to $*$.

After we integrate over one time step, we should make sure that $\vec{u}^*$ satisfies the continuity equation (1.1). We thus project this intermediate velocity $\vec{u}^*$ onto the divergence-free space (Sverdrup, Nikiforakis, & Almgren, 2018). For the projection step, we first express $\vec{u}^*$ according to the Helmholtz-Hodge-Decomposition (Chorin & Marsden, 1993),

$$\vec{u}^* = \vec{u}^{n+1} + \nabla \phi, \tag{4.26}$$

where $\vec{u}^{n+1}$ is the new velocity at time t_{n+1} that satisfies the divergence-free condition and ϕ is a scalar function. To take advantage of the incompressibility of $\vec{u}^{n+1}$, we find the divergence of equation (4.26), leading to the Poisson equation for ϕ,

$$\nabla^2 \phi = \nabla \vec{u}^*.$$

After we solve for ϕ, applying given boundary conditions, we find the updated velocity, projecting the velocity $\vec{u}^*$ onto the divergence-free space to get the new time-level solutions.

$$\vec{u}^{n+1} = \vec{u}^* - \nabla \phi.$$

As we mentioned, my contribution to the AMReX-incflo for this project is the granular material viscosity evaluation and the RK2 scheme implementation. For the rest of the parts to solve for the Navier-Stokes equations, we use the AMReX-incflo library as it is. Note that the details of general algorithms for this library can be found in (Almgren et al., 1998).

4.5 Numerical validation for time integration

We compare the performance of time integration methods: 1) the explicit Euler, which was already available in the AMReX-incflo, and 2) the explicit RK2 scheme that we implemented for a higher-order strain rate rheology.

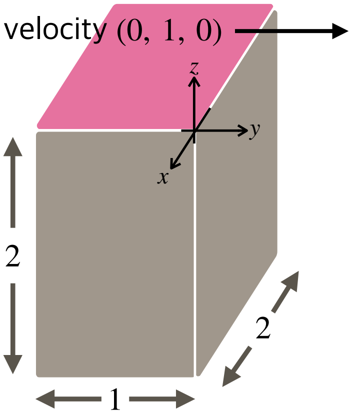

Figure 4.3: Numerical simulation domain box filled with sand type material. We use dimensions with centimeters for a length and seconds for a time scale.

For this validation, we consider a rectangular cuboid, as we show in Figure 4.3, with dimensions 2 cm (x) × 1 cm (y) × 2 cm (z), where all the walls in the $x-$ and $z-$directions have a no-slip boundary condition. We impose a periodic condition on the $y-$direction. Note that we consider centimeters (cm) for the length scale. In the finite volume sense of spatial discretization, the total number of cells composing the cuboid is $8 \times 8 \times 8$. We suppose this cuboid is filled with dry sands of a mean diameter $d = 0.15$ cm and material density $\rho = 1$ g/cm^3. To make sands flow, we move the top plate in the $y-$direction, shown as the pink in Figure 4.3, with the velocity (0, 1, 0) cm/s. For the rest of the parameters, we obtain information from other research papers. In (Senetakis, Coop, & Todisco, 2013), they observed the interparticle friction of dry sands $\mu_s \approx 0.01$ g·cm/s^2, in which particle sizes are in the range of 0.12 cm and 0.24 cm. We then find the fitting parameters from (Srivastava et al., 2021), as in the following Table 4.1. With this setup and parameters, we first observe the finest results to understand the flow.

	μ_i^0	α_i	A_i
$i = 1$	0.12	0.41	0.512
$i = 2$	0.02	0.31	0.252

Table 4.1: Fitting parameters of granular materials when the interparticle friction $\mu_s = 0.01$ (Srivastava et al., 2021).

4.5.1 Velocity in the shear flow direction

We first present the reference solution of our simulation. In particular, we show the velocity in the shear flow direction, y, in Figure 4.4. We use the explicit Euler method with the time step $\Delta t = 10^{-5}$ (s) as the reference solution. The final time of this validation is $t = 1$ s.

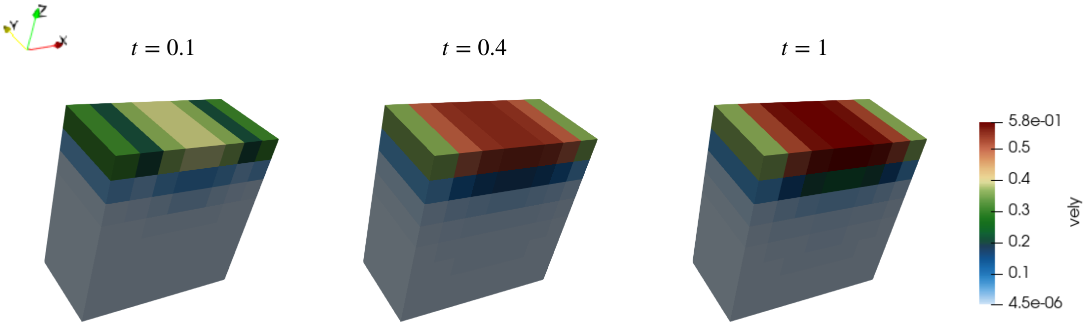

Figure 4.4: Velocity component (cm/s) in $y-$axis at time $t = 0.1,\ 0.4$ and $t = 1$ (s).

We note that in this setup, the velocity is independent of y, although we move the plate in this direction. To observe the variation of $x - z$ plane clearly, we obtain Figure 4.5 when $y = 1$. We can see that the most variation occurs on the top of the z-axis where the plate is moving.

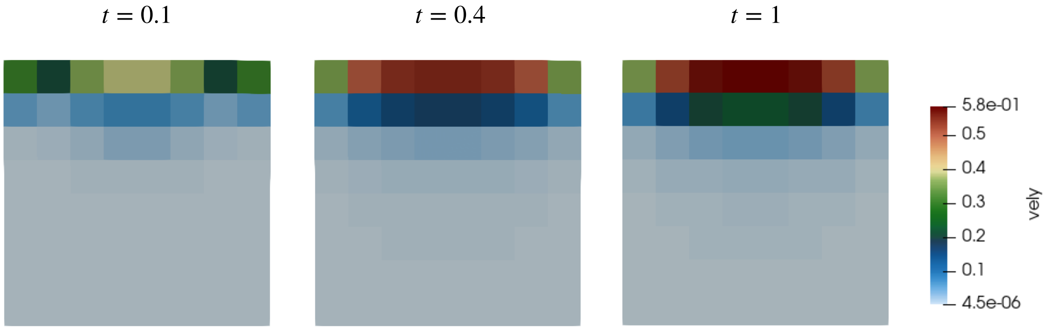

Figure 4.5: Velocity component (cm/s) in $y-$axis at time $t = 1, 6,$ and 10 (s).

4.5.2 Error analysis (order convergence)

Using the reference velocity in $y-$direction obtained by the explicit Euler, we get the errors of the Euler and RK2 methods with various time step sizes, Δt. In Figure 4.6, we obtain the infinite norm of the absolute difference of velocities in the $y-$axis. It is clear to see that RK2 is performing much better in terms of order convergence and accuracy.

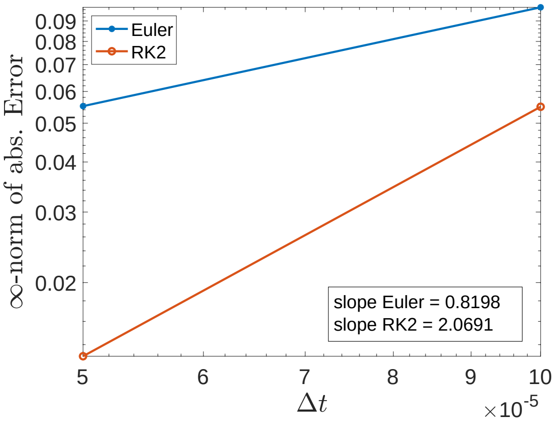

Figure 4.6: Order convergence between the explicit Euler and RK2 schemes at time $t = 1$ (s). The vertical axis shows the infinite norm of the absolute differences between the reference solution and each method.

As we expected, the explicit Euler method shows close to the first order, and the RK2 shows second-order convergence. Note that due to the time constraint, we used two points, $\Delta t = 10^{-4},\ 50^{-5}$, to plot Figure 4.6. Since the error of the explicit Euler method is large and we need the Euler method for a reference solution to validate the RK2 scheme, we have to use quite a small time step Δt to confirm the convergence.

4.6 Future work

There are several potential future works we could consider as an extension of this project. We may analyze the stabilities between the explicit Euler and RK2 methods for this particular granular flow in the cuboid. Our preliminary results of the new time integral implementation showed that the RK2 method was more stable than the explicit Euler method for certain fitting parameters. As we show in Figure 4.7, the stability region for the RK2 method is slightly larger in the imaginary direction than the explicit Euler (Griffiths & Higham, 2010). For advection-dominated problems, the spread of the eigenvalues of the Jacobian matrix is mostly along the imaginary direction. For this reason, we expect better stability for our problem as the diffusion is small compared to the advection.

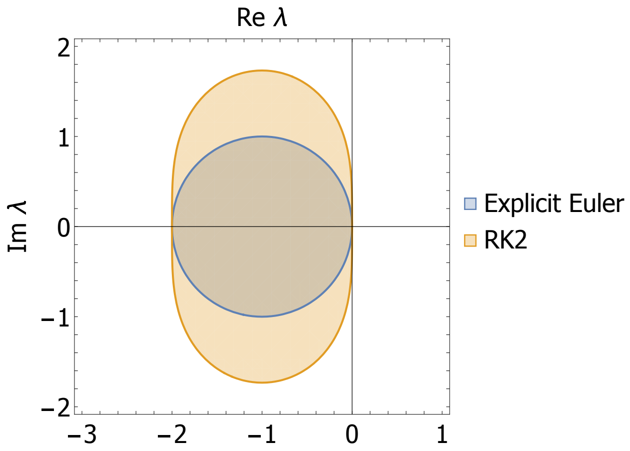

Figure 4.7: Stability regions of the explicit Euler and RK2 methods.

As we are concerned with the stability of explicit schemes, it would be useful to have an implicit time integration for the second-order strain tensor flow. Although further investigation is necessary, we anticipate having a second-order convergence with better stability with the following predictor-corrector scheme (Press, 2007),

$$\vec{u}^{temp} - \frac{1}{\rho}\nabla\left(\frac{\nabla\cdot\boldsymbol{\tau}_1^{temp}}{2}\right) = \vec{u}^n + \tilde{\boldsymbol{F}}\left(\vec{u}^n\right)\Delta t + \frac{1}{\rho}\nabla\left(\frac{\nabla\cdot\boldsymbol{\tau}_1^n}{2} + \nabla\cdot\boldsymbol{\tau}_2^n\right)\Delta t$$

$$\vec{u}^{n+1} - \frac{1}{\rho}\nabla\left(\frac{\nabla\cdot\boldsymbol{\tau}_1^{n+1}}{2}\right) = \vec{u}^n + \tilde{\boldsymbol{F}}\left(\vec{u}^n\right)\Delta t + \frac{1}{\rho}\nabla\left(\frac{\nabla\cdot\boldsymbol{\tau}_1^n}{2} + \frac{\nabla\cdot\boldsymbol{\tau}_2^n + \nabla\cdot\boldsymbol{\tau}_2^{temp}}{2}\right)\Delta t$$

where

$$\tilde{\boldsymbol{F}}\left(\vec{u}^n\right) = -\vec{u}^n\cdot\nabla\vec{u}^n + \frac{1}{\rho}\left(-\nabla P^n + \rho\vec{g}\right).$$

The idea is similar to an implicit RK2 scheme. The main difference is that we split the viscous tensor $\boldsymbol{\tau}$ term into two parts,

$$\boldsymbol{\tau}_1 \propto \boldsymbol{D}, \quad \text{and} \quad \boldsymbol{\tau}_2 \propto \boldsymbol{D}^2.$$

The complication of this implementation is building the linear system to solve for each velocity, $\vec{u}^{temp}$ and $\vec{u^{n+1}}$.

From the second-order strain rate rheology perspective, we consider adding the time-dependent term,

$$\mu_3\left[\boldsymbol{D}\boldsymbol{W} - \boldsymbol{W}\boldsymbol{D},\right] \tag{4.27}$$

to the stress tensor give in equation (4.14). The viscosity coefficient can be found by modifying the $\mu(I)$ rheology (4.18),

$$\mu(I)_3 = -A_3\left(I^2\right)^{\alpha_3} = \frac{\eta_3\dot{\gamma}^2}{P}. \tag{4.28}$$

Specifically, we can find the coefficients of each shear rate term in equation (4.14) as

$$\mu_3 = -PA_3\left(\frac{\dot{\gamma}d}{\sqrt{P/\rho}}\right)^{2\alpha_3}\frac{1}{\dot{\gamma}^2}. \tag{4.29}$$

To obtain more realistic simulations, it would be necessary to connect the granular rheology with a compressible flow.

It is also interesting that solid particles suspended in a Newtonian fluid can exhibit highly non-Newtonian behaviors. To model this type of behavior, we may implement immersed boundary methods to simulate a suspension of solid particles in a Newtonian fluid, which is an important application area that has received significant research interest lately (Couturier et al., 2011).

Chapter 5

Conclusion

Modeling fluid interactions with other objects can deliver information we cannot easily obtain in physical experiments. To achieve this, we studied both Newtonian and non-Newtonian fluids by investigating marine aggregate models and granular rheology.

We discussed the settling marine aggregate simulations in the first two parts of this thesis. We are motivated to explore marine aggregates by their relevance to global climate change, which is the most significant environmental problem we face today. The ocean absorbs approximately 40% of the carbon dioxide (CO_2) produced anthropogenically (Omand et al., 2020). A portion of the atmospheric CO_2 is dissolved at the surface of the ocean and fixed by marine aggregates. As they transport the dissolved carbon to the deep sea, marine aggregates contribute to reducing the atmospheric CO_2 level. While there are many active experimental works in oceanography, there are limitations to obtaining and processing an actual marine aggregate. With a computational approach, we can reduce these restrictions and assist in research for marine aggregate dynamics. Our ultimate goal for this project is thus to provide numerical tools to attain useful information related to biological or oceanic research.

The methods we developed can create randomly formed aggregate models having a fractal dimension using two algorithms, individually-added aggregation, and cluster-to-cluster aggregation. The parameters for surrounding fluid can be easily adjusted in the Stokes approximation. In the homogeneous fluid, we found a suitable length scale for fractal aggregates to allow users to predict different forces acting on the aggregates as they settle. For a more realistic investigation, we simulate the settling marine aggregate model in a density-stratified fluid. We can quantify several values of interest, including settling speed, time to pass a fluid density gradient, and concentration perturbation. We hope to contribute to oceanic carbon cycle research by providing an understanding of the fluid dynamics of marine aggregates.

For the last chapter of this thesis, we introduced a general strain-to-stress relation for complex fluids that show non-Newtonian behaviors. Since they tend to exhibit more complicated properties than Newtonian fluids, there are still many open questions in this field. In this project, we particularly focused on flows of granular materials, which can be found everywhere in our daily lives. One example is the sand sliding in nature. A dune sliding due to its instability could be extremely hazardous and may even result in casualties depending on its location. In this case, measuring and predicting the slope of a dune is important to prevent any future accidents (Xie et al., 2021). Since their state can co-exist between solid, liquid, and gas, simulating granular material behaviors using computational programs is generally difficult. The constitutive rheology code, AMReX-incflo, developed by researchers at Lawrence Berkeley National Laboratory, provides various rheological models by incorporating a viscous term into an incompressible flow. In this library, we implemented the viscosity computation for granular rheology. To explore a second-order shear rate behavior of complex fluids, we also coded the quadratic strain tensor computation for the incompressible flow solution. For better order convergence and stability, we added a two-stage Runge-Kutta scheme in the AMReX-incflo. Our numerical development in the AMReX-incflo would allow us to examine complex fluid behavior in a more sophisticated way. We hope to continue studying complex fluid research and contributing to various scientific fields.

Bibliography

Alldredge, A. L., & Gotschalk, C. (1988). In situ settling behavior of marine snow1. *Limnology and Oceanography*, *33*(3), 339–351. https://doi.org/https://doi.org/10.4319/lo.1988.33.3.0339

Alldredge, A. L., Cowles, T. J., MacIntyre, S., Rines, J. E. B., Donaghay, P. L., Greenlaw, C. F., Holliday, D. V., Dekshenieks, M. M., Sullivan, J. M., & Zaneveld, J. R. V. (2002). Occurrence and mechanisms of formation of a dramatic thin layer of marine snow in a shallow Pacific fjord. *Marine Ecology Progress Series*, *233*, 1–12. https://doi.org/10.3354/meps233001

Almgren, A. S., Bell, J. B., Colella, P., Howell, L. H., & Welcome, M. L. (1998). A Conservative Adaptive Projection Method for the Variable Density Incompressible Navier–Stokes Equations. *Journal of Computational Physics*, *142*(1), 1–46. https://doi.org/10.1006/jcph.1998.5890

Atkinson, K. E. (1997). *The Numerical Solution of Integral Equations of the Second Kind*. Cambridge University Press. https://doi.org/10.1017/CBO9780511626340

Bao, Y., Donev, A., Griffith, B. E., McQueen, D. M., & Peskin, C. S. (2017). An Immersed Boundary method with divergence-free velocity interpolation and force spreading. *Journal of Computational Physics*, *347*, 183–206. https://doi.org/10.1016/j.jcp.2017.06.041

Bao, Y., Rachh, M., Keaveny, E. E., Greengard, L., & Donev, A. (2018). A fluctuating boundary integral method for Brownian suspensions. *Journal of Computational Physics*, *374*, 1094–1119. https://doi.org/10.1016/j.jcp.2018.08.021

Barnes, H. A., Hutton, J. F., & Walters, K. (1989, June). *An Introduction to Rheology* [Google-Books-ID: B1e0uxFg4oYC]. Elsevier.

Binder, C., Hartig, M. A. J., & Peukert, W. (2009). Structural dependent drag force and orientation prediction for small fractal aggregates. *Journal of Colloid and Interface Science*, *331*(1), 243–250. https://doi.org/10.1016/j.jcis.2008.11.021

Bingham, E. C. (1917). *An Investigation of the Laws of Plastic Flow* [Google-Books-ID: 0EhpNVCVShUC]. U.S. Government Printing Office.

Bird, R. B., Armstrong, R. C., & Hassager, O. (1987). Dynamics of polymeric liquids. Vol. 1, 2nd Ed. : Fluid mechanics [Publisher: John Wiley and Sons Inc.,New York, NY]. Retrieved May 15, 2023, from https://www.osti.gov/biblio/6164599

Bossis, G., Meunier, A., & Brady, J. F. (1991). Hydrodynamic stress on fractal aggregates of spheres. *The Journal of Chemical Physics*, *94*(7), 5064–5070. https://doi.org/10.1063/1.460543

Boyer, F., Pouliquen, O., & Guazzelli, É. (2011). Dense suspensions in rotating-rod flows: Normal stresses and particle migration [Publisher: Cambridge University Press]. *Journal of Fluid Mechanics*, *686*, 5–25. https://doi.org/10.1017/jfm.2011.272

Brady, J. F., & Bossis, G. (1988). Stokesian Dynamics. *Annual Review of Fluid Mechanics*, *20*(1), 111–157. https://doi.org/10.1146/annurev.fl.20.010188.000551

Camassa, R., Khatri, S., McLaughlin, R. M., Prairie, J. C., White, B. L., & Yu, S. (2013). Retention and entrainment effects: Experiments and theory for porous spheres settling in sharply stratified fluids. *Physics of Fluids*, *25*(8), 081701. https://doi.org/10.1063/1.4819407

Chan, C. Y., Beris, A. N., & Advani, S. G. (1992). Second-order boundary element method calculations of hydrodynamic interactions between particles in close proximity. *International Journal for Numerical Methods in Fluids*, *14*(9), 1063–1086. https://doi.org/10.1002/fld.1650140905

Chen, Z.-Y., Deutch, J. M., & Meakin, P. (1984). Translational friction coefficient of diffusion limited aggregates. *The Journal of Chemical Physics*, *80*(6), 2982–2983. https://doi.org/10.1063/1.447012

Cheng, H., Greengard, L., & Rokhlin, V. (1999). A Fast Adaptive Multipole Algorithm in Three Dimensions. *Journal of Computational Physics*, *155*(2), 468–498. https://doi.org/10.1006/jcph.1999.6355

Chorin, A. J., & Marsden, J. E. (1993). *A Mathematical Introduction to Fluid Mechanics* (J. E. Marsden, L. Sirovich, & M. Golubitsky, Eds.; Vol. 4). Springer. https://doi.org/10.1007/978-1-4612-0883-9

Coleman, B. D., & Noll, W. (1960). An approximation theorem for functionals, with applications in continuum mechanics. *Archive for Rational Mechanics and Analysis*, *6*(1), 355–370. https://doi.org/10.1007/BF00276168

Cortez, R. (2001). The Method of Regularized Stokeslets [Publisher: Society for Industrial and Applied Mathematics]. *SIAM Journal on Scientific Computing*, *23*(4), 1204–1225. https://doi.org/10.1137/S106482750038146X

Couturier, É., Boyer, F., Pouliquen, O., & Guazzelli, É. (2011). Suspensions in a tilted trough: Second normal stress difference [Publisher: Cambridge University Press]. *Journal of Fluid Mechanics*, *686*, 26–39. https://doi.org/10.1017/jfm.2011.315

Delves, L. M., & Mohamed, J. L. (1985). *Computational Methods for Integral Equations*. Cambridge University Press. https://doi.org/10.1017/CBO9780511569609

Delves, L., Walsh, J., Mathematics, U. o. M. D. o., Computational, U. o. L. D. o., & Science, S. (1974). *Numerical Solution of Integral Equations*. Clarendon Press. https://books.google.com/books?id=tuqQwgEACAAJ

Eggersdorfer, M. L., Kadau, D., Herrmann, H. J., & Pratsinis, S. E. (2011). Multiparticle Sintering Dynamics: From Fractal-Like Aggregates to Compact Structures [Publisher: American Chemical Society]. *Langmuir*, *27*(10), 6358–6367. https://doi.org/10.1021/la200546g

Gastaldi, A., & Vanni, M. (2011). The distribution of stresses in rigid fractal-like aggregates in a uniform flow field. *Journal of Colloid and Interface Science*, *357*(1), 18–30. https://doi.org/10.1016/j.jcis.2011.01.080

Gmachowski, L. (2002). Calculation of the fractal dimension of aggregates. *Colloids and Surfaces A: Physicochemical and Engineering Aspects*, *211*(2), 197–203. https://doi.org/10.1016/S0927-7757(02)00278-9

Greengard, L., & Rokhlin, V. (1987). A fast algorithm for particle simulations. *Journal of Computational Physics*, *73*(2), 325–348. https://doi.org/10.1016/0021-9991(87)90140-9

Greengard, L., & Rokhlin, V. (1997). A new version of the Fast Multipole Method for the Laplace equation in three dimensions [Publisher: Cambridge University Press]. *Acta Numerica*, *6*, 229–269. https://doi.org/10.1017/S0962492900002725

Greengard, L. F., & Huang, J. (2002). A New Version of the Fast Multipole Method for Screened Coulomb Interactions in Three Dimensions. *Journal of Computational Physics*, *180*(2), 642–658. https://doi.org/10.1006/jcph.2002.7110

Griffiths, D. F., & Higham, D. J. (2010, November). *Numerical Methods for Ordinary Differential Equations: Initial Value Problems* [Google-Books-ID: HrrZop_3bacC]. Springer Science & Business Media.

Guazzelli, É., & Morris, J. F. (2011). *A Physical Introduction to Suspension Dynamics*. Cambridge University Press. https://doi.org/10.1017/CBO9780511894671

Gurel, S., Ward, S. G., & Whitmore, R. L. (1955). Studies of the viscosity and sedimentation of suspensions: Part 3. - The sedimentation of isometric and compact particles [Publisher: IOP Publishing]. *British Journal of Applied Physics*, *6*(3), 83–87. https://doi.org/10.1088/0508-3443/6/3/304

Henson, S. A., Sanders, R., & Madsen, E. (2012). Global patterns in efficiency of particulate organic carbon export and transfer to the deep ocean. *Global Biogeochemical Cycles*, *26*(1). https://doi.org/https://doi.org/10.1029/2011GB004099

Herschel, W. H., & Bulkley, R. (1926). Konsistenzmessungen von Gummi-Benzollösungen. *Kolloid-Zeitschrift*, *39*(4), 291–300. https://doi.org/10.1007/BF01432034

Honjo, S., Eglinton, T., Taylor, C., Ulmer, K., Sievert, S., Bracher, A., German, C., Edgcomb, V., Francois, R., Iglesias-Rodriguez, M. D., Van Mooy, B., & Rapeta, D. (2014). Understanding the Role of the Biological Pump in the Global Carbon Cycle: An Imperative for Ocean Science. *Oceanography*, *27*(3), 10–16. https://doi.org/10.5670/oceanog.2014.78

Ingber, M. S., & Mammoli, A. A. (1999). A comparison of integral formulations for the analysis of low Reynolds number flows. *Engineering Analysis with Boundary Elements*, *23*(4), 307–315. https://doi.org/10.1016/S0955-7997(98)00090-3

Irgens, F. (2014). *Rheology and Non-Newtonian Fluids*. Springer International Publishing. https://doi.org/10.1007/978-3-319-01053-3

Jackson, G. A. (1989). Simulation of bacterial attraction and adhesion to falling particles in an aquatic environment. *Limnology and Oceanography*, *34*(3), 514–530. https://doi.org/10.4319/lo.1989.34.3.0514

Jackson, G. A. (1990). A model of the formation of marine algal flocs by physical coagulation processes. *Deep Sea Research Part A. Oceanographic Research Papers*, *37*(8), 1197–1211. https://doi.org/10.1016/0198-0149(90)90038-W

Jackson, G. A., & Burd, A. B. (1998). Aggregation in the Marine Environment [Publisher: American Chemical Society]. *Environmental Science & Technology*, *32*(19), 2805–2814. https://doi.org/10.1021/es980251w

Johnson, C. P., Li, X., & Logan, B. E. (1996). Settling Velocities of Fractal Aggregates [Publisher: American Chemical Society]. *Environmental Science & Technology*, *30*(6), 1911–1918. https://doi.org/10.1021/es950604g

Johnson, D. L., Leith, D., & Reist, P. C. (1987). Drag on non-spherical, orthotropic aerosol particles. *Journal of Aerosol Science*, *18*(1), 87–97. https://doi.org/10.1016/0021-8502(87)90013-9

Jop, P., Forterre, Y., & Pouliquen, O. (2006). A constitutive law for dense granular flows [Number: 7094 Publisher: Nature Publishing Group]. *Nature*, *441*(7094), 727–730. https://doi.org/10.1038/nature04801

Karrila, S. J., & Kim, S. (1989). Integral Equations of the Second Kind for Stokes Flow: Direct Solution for Physical Variables and Removal of Inherent Accuracy Limitations. *Chemical Engineering Communications*, *82*(1), 123–161. https://doi.org/10.1080/00986448908940638

Kaye, B. H. (2008, July). *A Random Walk Through Fractal Dimensions*. John Wiley & Sons.

Kiørboe, T., Grossart, H.-P., Ploug, H., & Tang, K. (2002). Mechanisms and Rates of Bacterial Colonization of Sinking Aggregates [Publisher: American Society for Microbiology]. *Applied and Environmental Microbiology*, *68*(8), 3996–4006. https://doi.org/10.1128/AEM.68.8.3996-4006.2002

Kolb, M. (1987). Anisotropic Diffusion Limited Aggregation: From Self-Similarity to Self-Affinity. *Europhysics Letters*, *4*(1), 85. https://doi.org/10.1209/0295-5075/4/1/014

Krishnaraj, K. P., & Nott, P. R. (2016). A dilation-driven vortex flow in sheared granular materials explains a rheometric anomaly [Number: 1 Publisher: Nature Publishing Group]. *Nature Communications*, *7*(1), 10630. https://doi.org/10.1038/ncomms10630

Kundu, P. K., Cohen, I. M., & Dowling, D. R. (2016, January). Chapter 4 - Conservation Laws. In P. K. Kundu, I. M. Cohen, & D. R. Dowling (Eds.), *Fluid Mechanics (Sixth Edition)* (pp. 109–193). Academic Press. https://doi.org/10.1016/B978-0-12-405935-1.00004-6

MacIntyre, S., Alldredge, A. L., & Gotschalk, C. C. (1995). Accumulation of marines now at density discontinuities in the water column. *Limnology and Oceanography*, *40*(3), 449–468. https://doi.org/10.4319/lo.1995.40.3.0449

McNown, J. S., & Malaika, J. (1950). Effects of particle shape on settling velocity at low Reynolds numbers. *Eos, Transactions American Geophysical Union*, *31*(1), 74–82. https://doi.org/https://doi.org/10.1029/TR031i001p00074

Nayar, K. G., Sharqawy, M. H., Banchik, L. D., & Lienhard V, J. H. (2016). Thermophysical properties of seawater: A review and new correlations that include pressure dependence. *Desalination*, *390*, 1–24. https://doi.org/10.1016/j.desal.2016.02.024

Omand, M. M., Govindarajan, R., He, J., & Mahadevan, A. (2020). Sinking flux of particulate organic matter in the oceans: Sensitivity to particle characteristics [Number: 1 Publisher: Nature Publishing Group]. *Scientific Reports*, *10*(1), 5582. https://doi.org/10.1038/s41598-020-60424-5

Panah, M., Blanchette, F., & Khatri, S. (2017). Simulations of a porous particle settling in a density-stratified ambient fluid [Publisher: American Physical Society]. *Physical Review Fluids*, *2*(11), 114303. https://doi.org/10.1103/PhysRevFluids.2.114303

Papanastasiou, T. C. (1987). Flows of Materials with Yield. *Journal of Rheology*, *31*(5), 385–404. https://doi.org/10.1122/1.549926

Park, E.-Y., & Choi, J. (2020). The Performance of Low-Pressure Seawater as a CO2 Solvent in Underwater Air-Independent Propulsion Systems [Number: 1 Publisher: Multidisciplinary Digital Publishing Institute]. *Journal of Marine Science and Engineering*, *8*(1), 22. https://doi.org/10.3390/jmse8010022

Polimeno, M., Kim, C., & Blanchette, F. (2022). Toward a Realistic Model of Diffusion-Limited Aggregation: Rotation, Size-Dependent Diffusivities, and Settling [Publisher: American Chemical Society]. *ACS Omega*, *7*(45), 40826–40835. https://doi.org/10.1021/acsomega.2c03547

Power, H., & Miranda, G. (1987). Second Kind Integral Equation Formulation of Stokes' Flows Past a Particle of Arbitrary Shape. *SIAM Journal on Applied Mathematics*, *47*(4), 689–698. https://doi.org/10.1137/0147047

Pozrikidis, C. (1992). *Boundary Integral and Singularity Methods for Linearized Viscous Flow*. Cambridge University Press. https://doi.org/10.1017/CBO9780511624124

Prairie, J. C., Ziervogel, K., Arnosti, C., Camassa, R., Falcon, C., Khatri, S., McLaughlin, R. M., White, B. L., & Yu, S. (2013). Delayed settling of marine snow at sharp density transitions driven by fluid entrainment and diffusion-limited retention. *Marine Ecology Progress Series*, *487*, 185–200. https://doi.org/10.3354/meps10387

Press, W. H. (2007, September). *Numerical Recipes 3rd Edition: The Art of Scientific Computing* [Google-Books-ID: 1aAOdzK3FegC]. Cambridge University Press.

Rajagopal, K. R. (2006). On implicit constitutive theories for fluids [Publisher: Cambridge University Press]. *Journal of Fluid Mechanics*, *550*, 243–249. https://doi.org/10.1017/S0022112005008025

Richard, P., Nicodemi, M., Delannay, R., Ribière, P., & Bideau, D. (2005). Slow relaxation and compaction of granular systems [Number: 2 Publisher: Nature Publishing Group]. *Nature Materials*, *4*(2), 121–128. https://doi.org/10.1038/nmat1300

Rogak, S. N., & Flagan, R. C. (1990). Stokes drag on self-similar clusters of spheres. *Journal of Colloid and Interface Science*, *134*(1), 206–218. https://doi.org/10.1016/0021-9797(90)90268-S

Rosenstock, H. B., & Marquardt, C. L. (1980). Cluster formation in two-dimensional random walks: Application to photolysis of silver halides [Publisher: American Physical Society]. *Physical Review B*, *22*(12), 5797–5809. https://doi.org/10.1103/PhysRevB.22.5797

Senetakis, K., Coop, M. R., & Todisco, M. C. (2013). The inter-particle coefficient of friction at the contacts of Leighton Buzzard sand quartz minerals. *Soils and Foundations*, *53*(5), 746–755. https://doi.org/10.1016/j.sandf.2013.08.012

Sharqawy, M. H., Lienhard, J. H., & Zubair, S. M. (2010). Thermophysical properties of seawater: A review of existing correlations and data. *Desalination and Water Treatment*, *16*(1-3), 354–380. https://doi.org/10.5004/dwt.2010.1079

Singh, R. P., & Heldman, D. R. (2013, June). *Introduction to Food Engineering*. Academic Press.

Smith, D. J. (2018). A nearest-neighbour discretisation of the regularized stokeslet boundary integral equation. *Journal of Computational Physics*, *358*, 88–102. https://doi.org/10.1016/j.jcp.2017.12.008

Smithies, F. (1959). Integral equations and their applications to certain problems in mechanics, mathematical physics and technology. By S. G. Mikhlin. Translated from the Russian by A. H. Armstrong. Pp. xii, 338. 80s. 1957. (Pergamon Press) [Publisher: Cambridge University Press]. *The Mathematical Gazette*, *43*(344), 156–156. https://doi.org/10.2307/3610248

Srivastava, I., Silbert, L. E., Grest, G. S., & Lechman, J. B. (2021). Viscometric flow of dense granular materials under controlled pressure and shear stress [Publisher:

Cambridge University Press]. *Journal of Fluid Mechanics*, *907*. https://doi.org/10.1017/jfm.2020.811

Stakgold, I. (2000, January). *Boundary Value Problems of Mathematical Physics: Volume 1*. Society for Industrial; Applied Mathematics. https://doi.org/10.1137/1.9780898719888

Sverdrup, K., Nikiforakis, N., & Almgren, A. (2018). Highly parallelisable simulations of time-dependent viscoplastic fluid flow with structured adaptive mesh refinement [Publisher: American Institute of Physics]. *Physics of Fluids*, *30*(9), 093102. https://doi.org/10.1063/1.5049202

Takayasu, M. M., & Galembeck, F. (1998). Determination of the Equivalent Radii and Fractal Dimension of Polystyrene Latex Aggregates from Sedimentation Coefficients. *Journal of Colloid and Interface Science*, *202*(1), 84–88. https://doi.org/10.1006/jcis.1998.5428

Tang, P., Greenwood, J., & Raper, J. A. (2002). A Model to Describe the Settling Behavior of Fractal Aggregates. *Journal of Colloid and Interface Science*, *247*(1), 210–219. https://doi.org/10.1006/jcis.2001.8028

Tanner, R. I. (2018). Review Article: Aspects of non-colloidal suspension rheology. *Physics of Fluids*, *30*(10), 101301. https://doi.org/10.1063/1.5047535

Tornberg, A.-K., & Greengard, L. (2008). A fast multipole method for the three-dimensional Stokes equations. *Journal of Computational Physics*, *227*(3), 1613–1619. https://doi.org/10.1016/j.jcp.2007.06.029

Vanni, M. (2015). Accurate modelling of flow induced stresses in rigid colloidal aggregates. *Computer Physics Communications*, *192*, 70–90. https://doi.org/10.1016/j.cpc.2015.02.022

Wiltzius, P. (1987). Hydrodynamic behavior of fractal aggregates [Publisher: American Physical Society]. *Physical Review Letters*, *58*(7), 710–713. https://doi.org/10.1103/PhysRevLett.58.710

Witten, T. A., & Cates, M. E. (1986). Tenuous Structures from Disorderly Growth Processes [Publisher: American Association for the Advancement of Science]. *Science*, *232*(4758), 1607–1612. https://doi.org/10.1126/science.232.4758.1607

Witten, T. A., & Sander, L. M. (1981). Diffusion-Limited Aggregation, a Kinetic Critical Phenomenon [Publisher: American Physical Society]. *Physical Review Letters*, *47*(19), 1400–1403. https://doi.org/10.1103/PhysRevLett.47.1400

Wollast, R., & Garrels, R. M. (1971). Diffusion Coefficient of Silica in Seawater [Number: 3 Publisher: Nature Publishing Group]. *Nature Physical Science*, *229*(3), 94–94. https://doi.org/10.1038/physci229094a0

Xie, L., Wang, B., Zhu, Q., & Cui, J. (2021). Summary and Trend Analysis of Research Progress on Granular Slope Geological Hazards [Publisher: IOP Publishing]. *IOP Conference Series: Earth and Environmental Science*, *820*(1), 012022. https://doi.org/10.1088/1755-1315/820/1/012022

Yoo, E., Khatri, S., & Blanchette, F. (2020). Hydrodynamic forces on randomly formed marine aggregates [Publisher: American Physical Society]. *Physical Review Fluids*, *5*(4), 044305. https://doi.org/10.1103/PhysRevFluids.5.044305

Youngren, G. K., & Acrivos, A. (1975). Stokes flow past a particle of arbitrary shape: A numerical method of solution [Publisher: Cambridge University Press]. *Journal of Fluid Mechanics*, *69*(2), 377–403. https://doi.org/10.1017/S0022112075001486

Zhang, J., & Zhang, Q. (2015). Direct Simulation of Drag Force on Fractal Flocs during Settling [Publisher: Coastal Education and Research Foundation]. *Journal of Coastal Research*, *73*(sp1), 753–757. https://doi.org/10.2112/SI73-129.1

Zinchenko, A. Z., & Davis, R. H. (2006). A boundary-integral study of a drop squeezing through interparticle constrictions [Publisher: Cambridge University Press]. *Journal of Fluid Mechanics*, *564*, 227–266. https://doi.org/10.1017/S0022112006001479

Appendix A

Appendix for Chapter 2

A.1 Exact Kernel Integration

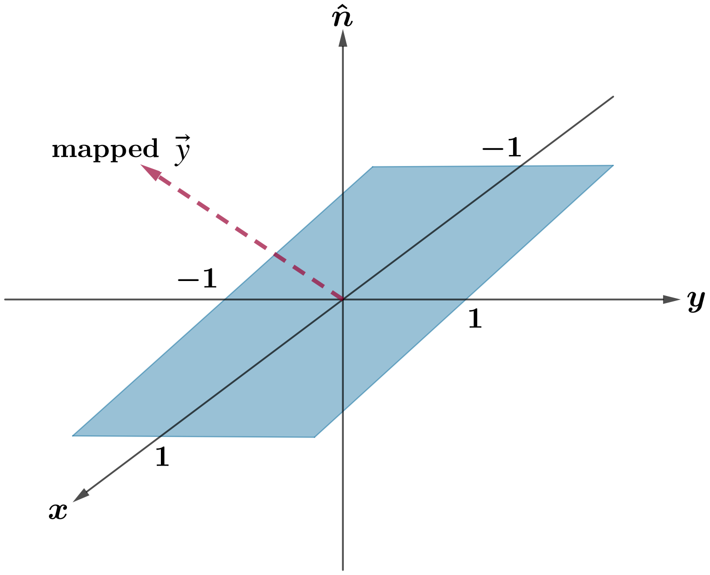

Figure A.1: Schematic of the mapped domain where numerical integration is performed.

When computing the flow around the aggregates, we need to integrate over square surfaces. To integrate over any square face, we first map the square over which we need to integrate to the square $(x, y, 0)$ with $x \in [-1, 1]$ and $y \in [-1, 1]$, as depicted in Fig. (A.1). The normal to the surface is thus always in the $z-$direction. We may then exactly evaluate all the surface integrals involved in either the single-layer or double-layer potential methods.

A.1.1 Single-layer potential

In the single-layer potential approach, we need to compute integrals of the form

$$\int_S \left(\frac{\bar{\bar{I}}}{||\vec{x}-\vec{y}||} + \frac{(\vec{x}-\vec{y})(\vec{x}-\vec{y})}{||\vec{x}-\vec{y}||^3} \right) \mathrm{d}S(\vec{x})$$

$$= \int_S \frac{\bar{\bar{I}}}{||\vec{x}-\vec{y}||} \mathrm{d}S(\vec{x}) + \int_S \frac{(\vec{x}-\vec{y})(\vec{x}-\vec{y})}{||\vec{x}-\vec{y}||^3} \mathrm{d}S(\vec{x}) = I_1 + I_2. \tag{A.1}$$

Here, we have that $\vec{x} = (x, y, 0)$ and we write $\vec{y} = (x_0, y_0, z_0)$ and

$$||\vec{x}-\vec{y}|| = R(x,y) = \sqrt{(x-x_0)^2 + (y-y_0)^2 + z_0^2}$$

We first consider the case when $x_0 = y_0 = z_0 = 0$, which arises when integrating over a face centered at the point where we are computing the velocity. In that case, we have $R(x,y) = \sqrt{x^2+y^2}$. We find for the diagonal terms of I_1

$$\int_{-1}^{1} \int_{-1}^{1} \frac{1}{\sqrt{x^2+y^2}} \, \mathrm{d}x\mathrm{d}y = 8 \text{ arcsinh}(1) \tag{A.2}$$

and all the non-diagonal terms are zero.

Away from the singularity, we can generally find antiderivatives computed using Mathematica. For the integral I_1, we have

$$\int_S \frac{1}{||\vec{x}-\vec{y}||} \mathrm{d}S(\vec{x}) = \int_{-1}^{1} \int_{-1}^{1} \frac{1}{R(x,y)} \, \mathrm{d}x\mathrm{d}y$$

$$= (x-x_0) \log\left(R(x,y) + (y-y_0)\right) + (y-y_0) \log\left(R(x,y) + (x-x_0)\right)$$

$$-z_0 \arctan\left(\frac{(x-x_0)(y-y_0)}{z_0 R(x,y)} \right) + z_0 \arctan\left(\frac{(y-y_0)}{z_0} \right) - (y-y_0) \Bigg|_{x=-1}^{1} \Bigg|_{y=-1}^{1}. \tag{A.3}$$

Note that there is no issue with evaluating the arctangent when $z_0 = 0$, as the multiplication by z_0 yields zero. Also, we need to be careful using this antiderivative when evaluating cases where $z_0 = 0$ and $|x_0| = |y_0| = 1$. In that case, the integral simplifies to

$$\int_{-1}^{1} \int_{-1}^{1} \frac{1}{\sqrt{1+x^2}} \, \mathrm{d}x\mathrm{d}y = 4 \sinh^{-1}(1). \tag{A.4}$$

Next, we consider the second part of the integral equation (A.1), I_2, which we index with m and n

$$I_2 = \int_{-1}^{1} \int_{-1}^{1} \frac{(\vec{x}-\vec{y})_m (\vec{x}-\vec{y})_n}{R(x,y)^3} \, \mathrm{d}x\mathrm{d}y. \tag{A.5}$$

Note that the numerator in equation (A.5), written in index notation, refers to four different cases. There are two square-like terms

$$\text{(a)} \quad (x-x_0)(x-x_0) \quad \text{or} \quad (y-y_0)(y-y_0) \quad \text{and (b)} \quad z_0^2,$$

and two mixed terms

$$\text{(c)} \quad (x-x_0)(y-y_0) \quad \text{and (d)} \quad -(x-x_0)(z_0) \quad \text{or} \quad -(y-y_0)(z_0).$$

Again, we treat $x_0 = y_0 = z_0 = 0$ separately. The first two diagonal terms (case (a)) are then

$$\int_{-1}^{1}\int_{-1}^{1} \frac{x^2}{(x^2+y^2)^{3/2}}\,\mathrm{d}x\mathrm{d}y = 4\,\text{arcsinh}(1). \tag{A.6}$$

The third diagonal term is zero because of $z_0 = 0$, and every non-diagonal term is zero by symmetry.

Assuming that $x_0y_0z_0 \neq 0$, we consider cases (a)-(d) in turn. For case (a), we have

$$\int_{-1}^{1}\int_{-1}^{1} \frac{(x-x_0)^2}{R(x,y)^3}\,\mathrm{d}x\mathrm{d}y = (y-y_0)\left(\log\left(R(x,y)+x\right)-1\right)$$
$$+z_0\arctan\left(\frac{(y-y_0)}{z_0}\right) - z_0\arctan\left(\frac{(x-x_0)(y-y_0)}{z_0R(x,y)}\right)\Bigg|_{x=-1}^{1}\Bigg|_{y=-1}^{1}. \tag{A.7}$$

This case does not have evaluation issues since the argument of the logarithm can only be zero if $y = y_0$, which causes this entire term to be zero. Also, $R(x,y)$ can only be zero if $z_0 = 0$, which would then ensure that the third term would be zero. Note that the cases with numerator $(y-y_0)^2$ and $(x-x_0)^2$ are equivalent if we swap the x and y variables by choosing a different mapping.

Case (b) is simpler since the z_0 term is constant.

$$\int_{-1}^{1}\int_{-1}^{1} \frac{z_0^2}{R(x,y)^3}\,\mathrm{d}x\mathrm{d}y = \ z_0\arctan\left(\frac{(x-x_0)(y-y_0)}{z_0R(x,y)}\right)\Bigg|_{x=-1}^{1}\Bigg|_{y=-1}^{1} \tag{A.8}$$

Here, the only possibility to have an undefined value is when $z_0 = 0$, which simply gives a value of zero as the multiplying factor z_0 dominates the arctangent.

For case (c), we find

$$\int_{-1}^{1}\int_{-1}^{1} \frac{(x-x_0)(y-y_0)}{R(x,y)^3}\,\mathrm{d}x\mathrm{d}y = \ -R(x,y)\big|_{x=-1}^{1}\Big|_{y=-1}^{1}. \tag{A.9}$$

Finally, for case (d), we have

$$\int_{-1}^{1}\int_{-1}^{1}\frac{(x-x_0)z_0}{R(x,y)^3}\,\mathrm{d}x\mathrm{d}y = \; -z_0\log\left(R(x,y)+(y-y_0)\right)\big|_{x=-1}^{1}\Big|_{y=-1}^{1}. \tag{A.10}$$

As before, this case also does not have any issue since $R(x,y)+(y-y_0)$ can only be zero if $z_0=0$, which causes the entire term to be zero.

A.1.2 Double-layer potential

We now consider the double-layer potential integrals of the form

$$\int_S \frac{(\vec{x}-\vec{y})(\vec{x}-\vec{y})}{R(x,y)^5}\,(\vec{x}-\vec{y})\cdot n_k\,\mathrm{d}S(\vec{x}). \tag{A.11}$$

Since the inner product between the position and normal vectors always gives z_0 in the mapped coordinates, we focus on the integral,

$$\int_S \frac{(\vec{x}-\vec{y})_m(\vec{x}-\vec{y})_n}{R(x,y)^5}\,\mathrm{d}S(\vec{x}). \tag{A.12}$$

Note that we only need to compute this integral when $z_0 \neq 0$, as otherwise equation (A.11) is zero because of the inner product. This also implies that $R(x,y)$ may never be zero.

We now consider the following four cases:

(a) $m=n=1$ or $m=n=2$,

(b) $m=n=3$,

(c) $m=1, n=2$ or $m=2, n=1$,

(d) m =1 or 2 and $n=3$, or $m=3$ and n =1 or 2 vice versa.

For case (a), we find

$$\int_{-1}^{1}\int_{-1}^{1}\frac{(x-x_0)^2}{R(x,y)^5}\,\mathrm{d}x\mathrm{d}y$$

$$=\frac{1}{3}\left[\frac{1}{z_0}\arctan\left(\frac{(x-x_0)(y-y_0)}{z_0R(x,y)}\right)-\frac{(x-x_0)(y-y_0)}{\left((x-x_0)^2+z_0^2\right)R(x,y)}\right]\Bigg|_{x=-1}^{1}\Bigg|_{y=-1}^{1}. \tag{A.13}$$

Since $z_0 \neq 0$ and $R(x,y)\neq 0$, there are no issues when evaluating this antiderivative.

For case (b),

$$\begin{aligned}\int_{-1}^{1}\int_{-1}^{1}\frac{z_0^2}{R(x,y)^5}\,\mathrm{d}x\mathrm{d}y = \frac{1}{3}\Bigg[\frac{1}{z_0}\arctan\left(\frac{(x-x_0)(y-y_0)}{z_0R(x,y)}\right)\\ +\frac{(x-x_0)(y-y_0)\left(R(x,y)^2+z_0^2\right)}{\left((x-x_0)^2+z_0^2\right)\left((y-y_0)^2+z_0^2\right)R(x,y)}\Bigg]\Bigg|_{x=-1}^{1}\Bigg|_{y=-1}^{1},\end{aligned} \tag{A.14}$$

which again can always be evaluated directly when $z_0 \neq 0$.

Case (c) is relatively simple, as we can see,

$$\int_{-1}^{1}\int_{-1}^{1} \frac{(x-x_0)(y-y_0)}{R(x,y)^5}\,\mathrm{d}x\mathrm{d}y = \left.\left.\frac{1}{3R(x,y)}\right|_{x=-1}^{1}\right|_{y=-1}^{1}. \tag{A.15}$$

Finally, case (d) is

$$\int_{-1}^{1}\int_{-1}^{1} \frac{(x-x_0)z_0}{R(x,y)^5}\,\mathrm{d}x\mathrm{d}y = \left.\left.-\frac{(y-y_0)z_0}{3\left((x-x_0)^2+z_0^2\right)R(x,y)}\right|_{x=-1}^{1}\right|_{y=-1}^{1}. \tag{A.16}$$

Once again, this is simple to evaluate when $z_0 \neq 0$.

A.2 Extensional Flow past a Sphere

In the case of a sphere of radius R_s, one may compute an exact solution for the flow satisfying $\vec{U}_{bg} = \bar{\bar{M}} \cdot \vec{x}$ at infinity and $\vec{U}_{bg} = 0$ on the surface of the sphere.

The Stokes flow around the sphere is then (Guazzelli & Morris, 2011)

$$\vec{u} = \left(\bar{\bar{M}} \cdot \vec{x}\right)\left(1 - \frac{R_s^5}{r^5}\right) + \left((\bar{\bar{M}} : \vec{x}\vec{x})\vec{x}\right)\left(\frac{5}{2}\right)\left(\frac{R_s^5}{r^7} - \frac{R_s^3}{r^5}\right)$$

and the corresponding pressure is

$$P = -5\mu R_s^3 \frac{\bar{\bar{M}} : \vec{x}\vec{x}}{r^5}$$

where $\vec{x}$ is the position vector and r the distance to the center of the sphere. The stress tensor is then

$$\begin{aligned}\bar{\bar{T}} \;=\; & 5\mu R_s^3 \frac{\bar{\bar{M}} : \vec{x}\vec{x}}{r^5} + 2\bar{\bar{M}}\left(1 - \frac{R_s^5}{r^5}\right). + (\vec{x}(\bar{\bar{M}}\cdot\vec{x}) + (\bar{\bar{M}}\cdot\vec{x})\vec{x})\left(\frac{10R_s^5}{r^7} - \frac{5R_s^3}{r^5}\right) \\ & + 5\left(\frac{R_s^5}{r^7} - \frac{R_s^3}{r^5}\right)(\bar{\bar{M}} : \vec{x}\vec{x})\bar{\bar{I}} + 5\left(\frac{5R_s^3}{r^7} - \frac{7R_s^5}{r^9}\right)(\bar{\bar{M}} : \vec{x}\vec{x})\vec{x}\vec{x}\end{aligned}$$

On the surface of the sphere, where $r = R_s$, we consider the stress vector, $\vec{f} = \bar{\bar{T}} \cdot \hat{n}$, where $\hat{n} = \vec{x}/R_s$, and find

$$\vec{f} = \left.\bar{\bar{T}} \cdot \hat{n}\right|_{r=R_s} = \frac{5\mu}{R_s^2}\left(\frac{2\bar{\bar{M}} : \vec{x}\vec{x}}{R_s} - \frac{2\bar{\bar{M}} : \vec{x}\vec{x}}{R_s} + \bar{\bar{M}} \cdot \vec{x}R_s\right) = \frac{5\mu\bar{\bar{M}} \cdot \vec{x}}{R_s}$$

For an eigenvector $\hat{v}_i$ with eigenvalue λ_i, we thus find

$$S_i = \frac{1}{2}\int_S |\vec{f} \cdot \vec{v}_i|\, dS = 5\pi\mu R_s^2 \lambda_i.$$